UNIVERSITÀ
DEGLI STUDI
FIRENZE

DOTTORATO DI RICERCA IN
INGEGNERIA INDUSTRIALE

Indirizzo Scienza ed Ingegneria dei Materiali

CICLO XXVII

COORDINATORE Prof. De Lucia Maurizio

DETERMINATION OF MAGNETIC ANISOTROPY OF SINGLE MOLECULE MAGNETS IN DIFFERENT ENVIRONMENTS

Settore Scientifico Disciplinare ING-IND/22

Dottorando
Dott. Cucinotta Giuseppe

(firma)

Tutore
Prof. Sessoli Roberta

(firma)

Coordinatore
Prof. De Lucia Maurizio

(firma)

Anni 2012/2014

Contents

Introduction

Magnetic materials and magnetic anisotropy (which is responsible for phenomena such as magnetic hysteresis and retaining of magnetization) hold, since their first employment in a compass during the Han Dynasty (206 BC – 220 AD) in China, an increasingly prominent role in the development of technology. Magnetic materials have become so important that they are indispensable in today's life. Electric motors and generators, loudspeakers and microphones, electromagnets, magnetic memories, magnetic resonance imaging and medical applications: these represent only a short list of everyday devices whose functioning is based on the employment of materials. Their wide and ubiquitous use places magnetic materials at the center of a vast market (the global market for magnetic materials is forecast to reach 33 billion $ by the year 2018[1]) and makes them the subject of study whose aims are the improvement of the devices' performances and the design of new ones. At the same time magnetic materials attract also basic research scientists since magnetism is still an open chapter and molecular magnetism represents a good example of this fact.

The study and development of magnetic materials has traditionally dealt with 3D and 2D structures involving inorganic elements belonging mainly to transition metals or rare-earths in the shape of alloys or oxides. The magnetism of molecules was initially studied in the magnetochemistry field and considered an investigative way to discern chemical and electronic properties of molecules. The discovery in 1993 by Sessoli et al.[2,3] of the presence of magnetic hysteresis in the Mn_{12}ac molecular cluster paved the way to molecular magnetism as a new interdisciplinary research field in which chemists, physicists and material scientists collaborate to study and synthesize molecules characterized by magnetic properties. From then on

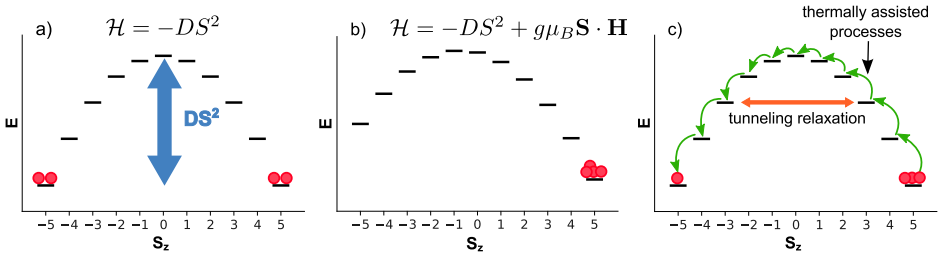

Figure 1: a) Energetic profile of an exemplifying $S = 6$ system in the double well potential $-DS_z^2$ at thermal equilibrium and b) in presence of an external magnetic field; c) schematic representation of principal relaxation processes occurring after the magnetic field is removed.

molecular magnetism spread unceasingly and new compounds showing magnetic properties at molecular scale have been discovered.

These molecules, named single molecule magnets (SMM), are constituted by a core of one or more paramagnetic metal ions combined with organic groups and present the peculiarity of exhibiting magnetic behaviors typical of bulk magnets (such as magnetic hysteresis and the retaining of magnetization state for a long time). Talking of single molecules such behaviors are not due to long range interactions as happens in massive magnets but are a direct expression of the quantum properties of the molecules. As will be shown, a SMM can be described, in a first approximation, by the Hamiltonian $\mathcal{H} = -DS_z^2$ where S_z is the z-component of the total spin of the molecule and D a parameter describing the magnetic anisotropy of the molecule. The result is a double well potential profile where the lowest levels, $S_z = \pm S$, have the same energy and are separated by a barrier of height DS^2 (see Figure 1). At thermal equilibrium the population of the $S_z = \pm S$ levels is equal and no net magnetization is shown by the system (Figure 1 a). When a magnetic field $\mathbf{H}$ is applied, the Zeeman term $\mathcal{H}_Z = g\mu_B \mathbf{H} \cdot \mathbf{S}$ must be considered in the Hamiltonian. The presence of $\mathcal{H}_Z$ modifies the energy levels arrangement, in particular the ground state is represented by only one of the levels $S_z = \pm S$ resulting in a magnetization of the system (Figure 1 b). Due to the presence of the barrier DS^2 removing the magnetic field does not suffice to restore the thermal equilibrium in the absence of the field since molecules remain confined in one of the two potential well presenting a remaining magne-

tization, also named remnant magnetization. In order to return to the starting condition before the magnetic field application a coercive field is required. The state of remnant magnetization in the absence of the field represents a situation far from thermal equilibrium and relaxation processes tending to restore the thermal levels' population are present. One of them is represented by phonon assisted thermal relaxation in which by coupling to phonons molecules can change their values of S_z (Figure 1 c). The relaxation rate is described by the Arrhenius law $\tau = \tau_0 e^{\frac{DS^2}{k_B T}}$ so in order to obtain large relaxation times large S and anisotropy parameter D are requested. Another relaxation mechanism involves tunneling processes from one well to the other. This is due to the presence of a transverse anisotropy term $E(S_x^2 - S_y^2)$ which admixing $|S_z\rangle$ states with opposite signs favors the tunneling mechanism. So another requirement for long relaxation times is a low transverse anisotropy.

Designing and synthesizing of SMMs with great spin values and large uniaxial anisotropy is the principal target for chemists researching SMMs with always better performances. Based on the first SMM discovered, Mn_{12}ac, in the first decade most of the efforts have been focused on high-spin, strongly-coupled transition metal clusters. In 2003 Ishikawa et al.[4] discovered SMM behaviors in lanthanide phthalocyanine sandwich complexes, $[LnPc_2]^n$ (Ln^{III}=Tb, Dy, Ho; H_2Pc=phthalocyanine; n = -1, 0, +1) opening the door to the research of single molecule magnets containing single rare-earths ions.

In the meantime SMMs attracted the interest of other scientist making molecular magnetism a crossroads for physicists and material scientists other than chemists. The possibility of manipulating the orientation of spin, the long relaxation times and molecular dimensions made SMMs objects of studies concerning the creation of switchable, molecular-scale devices that store or manipulate information.[5–7] Their quantum coherence properties brought to studies regarding a possible application in quantum computing.[8–10] Application of SMMs in spintronics devices[11] exploiting the possibility of manipulating spin-currents by means of interactions between the SMMs spin and the carriers ones, together with studies on properties of SMMs deposited on surfaces,[12] are other *hot topics* where SMMs are protagonists.

In this thesis are reported the results of studies conducted at LAboratory for Molecular Magnetism (LA.M.M.) of the University of Firenze concerning the characterization of magnetic anisotropy of magnetic molecules containing rare-earth ions together with the preliminary results of my work on electric transport measurements on devices containing magnetic molecules.

This work is so organized: Chapter 1 contains a survey of magnetic properties of single molecule magnets; in Chapter 2 are presented the main experimental techniques used together with the mathematical model followed to treat the data; Chapter 3 is dedicated to the exposition of results obtained from the magnetic characterization of the series of complexes formed by the ligand DOTA with the tripositive lanthanide ions of Tb, Dy, Ho, Er, Tm, Yb while in Chapter 4 are discussed the studies conducted on single crystals of the SMMs Cp*ErCOT. In Chapter 5 will be instead presented the explorative results obtained from the electric transport studies conducted on two different devices comprising magnetic molecules, the first consisting of interdigitate electrodes functionalized with a network of gold nanoparticles and a derivative of the Fe_4 SMM, the second one represented by a spin-valve device where a magnetic molecules layer is present.

1 Elements of magnetic anisotropy in SMMs

A system is said to possess magnetic anisotropy when its magnetic properties depend on spatial direction in contrast to magnetic isotropic systems whose magnetic behavior is the same whatever direction is considered. Single molecule magnets' properties (such as the blocking of magnetization) are ultimately ascribable to the presence of magnetic anisotropy in the molecule and the study of a SMM often goes hand in hand with the characterization of its magnetic anisotropy.

In this chapter a survey of the magnetic anisotropy properties of a SMM considering, step by step, all the interactions involved in the investigated processes will be presented.

As a starting point let us consider the isolated ion Hamiltonian $\mathcal{H}_{ion}$ which counts in turn a kinetic contribution and the electron-nucleus and electron-electron Coulomb interactions:

$$\begin{aligned} \mathcal{H}_{ion} &= \mathcal{H}_k + \mathcal{H}_{N\text{-}e} + \mathcal{H}_{e\text{-}e} \\ &= \sum_{i=1}^{N} \frac{p_i^2}{2m} - \sum_{i=1}^{N} \frac{Ze^2}{r_i} + \frac{1}{2} \sum_{i \neq j} \frac{e^2}{r_{ij}} \end{aligned} \tag{1.1}$$

where N is the number of electrons of the ion and Z its atomic number. The first two terms describes the behavior of N not-interacting electrons in the central potential of the nucleus and the eigenvalues are determined by the sum of the single electron energies $E_{n,i}$ which depend only on the principal quantum number n.

The introduction of electron-electron interaction implies a dependence of energy levels on orbital momentum. It is, at this point, convenient, given $\mathbf{l}_i$ and $\mathbf{s}_i$ the orbital angular momentum and the spin operator of the ith electron, to consider the total orbital angular momentum $\mathbf{L} = \sum_{i=1}^{N} \mathbf{l}_i$ and the total spin angular momentum $\mathbf{S} = \sum_{i=n}^{N} \mathbf{s}_i$ since they commute with $\mathcal{H}_{ion}$. As a consequence it is possible to find eigenfunctions of $\mathcal{H}_{ion}$ which are also eigenfunctions of the operators $\mathbf{L}^2$, $\mathbf{S}^2$, $\mathbf{L_z}$, $\mathbf{S_z}$ and one talks about LS (or Russell-Saunders) coupling. Each energy level associated with a couple LS (also called term) is usually denoted as ${}^{2S+1}L$ with the capital letters $S, P, D, F, \ldots$ corresponding to $L = 0, 1, 2, 3, \ldots$ and $2S + 1$ giving the spin multiplicity of the level. In order to determine the LS terms for a given electronic configuration the rules for the addition of angular momenta together with the Pauli exclusion principle must be used. It follows that for all the filled subshells $L = S = 0$ and thus they are represented by the term ${}^1S$.[†] This means that in order to determine the LS terms it suffices to consider only the incomplete subshells. The ground state configuration is instead defined by the Hund's rules which state that: (i) for a given configuration the term with the largest possible value of S has the lowest energy; (ii) if more than one term present the same value of S the one with the highest possible L value has the lowest energy.

The eigenstates of $\mathcal{H}_{ion}$, given its rotational symmetry, are not depending on L_z and S_z but each energy level, identified by the couple LS, is $(2L + 1)(2S + 1)$ times degenerate with respect to L_z and S_z. This degeneracy can be lifted by several mechanisms, the principal ones are spin-orbit interaction, crystal field and the presence of an external magnetic field. Relative strengths of such interactions, which are strongly dependent on molecule composition and structure, affect the theoretical approach to the description of the system. If one interaction is predominant in comparison to the others, usually, starting from the Hamiltonian (1.1), first its effects are considered on energetic levels' structure treating subsequently the other interactions as perturbations. On the contrary, if the effects of two or more interactions are comparable, the diagonalization of the complete Hamilto-

[†]In a filled subshell is present the maximum number $2(2l + 1)$ of equivalent electrons with the same n and l. Rules for addition of angular momenta and Pauli exclusion principle imply that $M_L = \sum_i m_{l_i} = 0$ (m_{l_i} runs over all the possible values $0, \pm1, \pm2, \ldots, \pm l$) and similarly $M_S = \sum_i m_{s_i} = 0$.

nian is required to properly describe the system.

In the next sections spin-orbit coupling, interaction with magnetic fields and crystal field interaction will be treated independently.

1.1 Spin-orbit interaction

Spin-orbit coupling originates from the electromagnetic interaction between the electron spins and the magnetic field generated by the electrons orbit around the nucleus. The Hamiltonian $\mathcal{H}_{so}$ describing such interaction is given by:

$$\mathcal{H}_{so} = A\,\mathbf{L}\cdot\mathbf{S} \tag{1.2}$$

with A a parameter depending on the considered atom. Introducing this term in the Hamiltonian implies that the spin and orbital angular momenta are combined together and L and S alone are no longer good quantum numbers to describe the eigenstates of the system since $\mathcal{H}_{ion} + \mathcal{H}_{so}$ is not diagonal in the basis $|L, S, L_z, S_z\rangle$. It is instead diagonal in the basis $|J, L, S, J_z\rangle$, where $\mathbf{J} = \mathbf{L} + \mathbf{S}$ is the total angular moment. We can in fact write $\mathbf{L}\cdot\mathbf{S} = \frac{1}{2}(\mathbf{J}^2 - \mathbf{L}^2 - \mathbf{S}^2)$ and the effect of spin-orbit interaction on energy levels is given in the new basis by:

$$\begin{aligned}&\frac{1}{2}A\langle J, L, S, J_z|\mathbf{J}^2 - \mathbf{L}^2 - \mathbf{S}^2|J, L, S, J_z\rangle \\ &= \frac{1}{2}A[J(J+1) - L(L+1) - S(S+1)]\,.\end{aligned} \tag{1.3}$$

As a result $(2L+1)(2S+1)$ degeneracy is partially removed: now each level is characterized by quantum number J which can assume all the values $|L-S| \leqslant J \leqslant L+S$. Using the Russell-Saunders notation the terms are now indicated by ${}^{2S+1}L_J$ while the ground state is $J = |L-S|$ if less than half of the subshell is occupied and $J = L+S$ otherwise.

1.2 Interaction with magnetic fields

Neglecting the small diamagnetic contribution, interaction with a magnetic field $\mathbf{H}$ is described by the Zeeman Hamiltonian:

$$\mathcal{H}_Z = \mu_B(\mathbf{L} + g_0\mathbf{S})\cdot\mathbf{H}\,, \tag{1.4}$$

where $\mu_B = \frac{e\hbar}{2m_e c} = 9.274 \times 10^{-21}$ erg/G indicates the Bohr magneton and $g_0 \approx 2.0023$ is the gyromagnetic ratio. The magnetic field contribution to the energy is so given by:

$$\Delta E_n = \mu_B \mathbf{H} \cdot \langle n|\mathbf{L} + 2\mathbf{S}|n\rangle \,. \tag{1.5}$$

Considering the basis $|L, S, J, J_z\rangle$, the Wigner-Eckart theorem[13] implies that the matrix elements of $(\mathbf{L} + 2\mathbf{S})$ are proportional to those of $\mathbf{J}$ so Equation (1.5) becomes:

$$\begin{aligned} \Delta E_n &= \mu_B \mathbf{H} \cdot \langle L, S, J, J_z|\mathbf{L} + 2\mathbf{S}|L, S, J, J'_z\rangle \\ &= \mu_B \mathbf{H} \cdot g_L \langle L, S, J, J_z|\mathbf{J}|L, S, J, J'_z\rangle \end{aligned} \tag{1.6}$$

where the proportionality constant is the Landé factor

$$g_L = \frac{3}{2} + \frac{S(S+1) - L(L+1)}{2J(J+1)} \,. \tag{1.7}$$

Defining the quantization axis z parallel to $\mathbf{H}$, Equation (1.6) implies that the magnetic field removes the $2J+1$ degeneracy of $|L, S, J, J_z\rangle$ states splitting the J_z levels by an amount given by:

$$\Delta E = g_L \mu_B H J_z \qquad J_z = -J, -J+1, \ldots J-1, J \,. \tag{1.8}$$

Consider now an ensemble of N atoms in a volume V, the thermodynamic average values of its magnetization M and magnetic susceptibility χ are respectively:[14]

$$M = -\frac{N}{V}\frac{\partial F}{\partial H} \tag{1.9}$$

$$\chi = \frac{\partial M}{\partial H} = -\frac{N}{V}\frac{\partial^2 F}{\partial H^2} \tag{1.10}$$

where F is the Helmholtz free energy defined by:

$$e^{-\beta F} = \sum_n e^{-\beta E_n} \,, \qquad \beta = \frac{1}{k_B T} \tag{1.11}$$

where the sum is considered over all the energetic levels E_n. If only the lowest $2J+1$ states are thermally populated with appreciable probability

Equation (1.11), taking into account Equation (1.8), can be written as:

$$\begin{aligned} e^{-\beta F} &= \sum_{J_z=-J}^{J} e^{-\beta g_L \mu_B H J_z} \\ &= \frac{e^{\beta g_L \mu_B H (J+1/2)} - e^{-\beta g_L \mu_B H (J+1/2)}}{e^{\beta g_L \mu_B H/2} - e^{-\beta g_L \mu_B H/2}} \ . \end{aligned} \tag{1.12}$$

The expression (1.9) for the magnetization gives:

$$M = -\frac{N}{V}\frac{\partial F}{\partial H} = \frac{N}{V} g_L \mu_B J B_J(\beta g_L \mu_B H) \ , \tag{1.13}$$

where the Brillouin function $B_J(x)$ is defined by

$$B_J(x) = \frac{2J+1}{2J} \coth\left(\frac{2J+1}{2J}\, x\right) - \frac{1}{2J} \coth\left(\frac{1}{2J}\, x\right) . \tag{1.14}$$

It follows from Equations (1.13) and (1.14) that for $k_B T \ll g_L \mu_B H$ (i.e. for very low temperatures and/or high magnetic fields) $B_J \to 1$ and $M = \frac{N}{V} g_L \mu_B J$ which corresponds to the saturation value for all the moments aligned to the field. On the contrary, for $k_B T \gg g_L \mu_B H$ $B_J(x) \to \frac{J+1}{3J} x$ and:

$$M = \frac{N}{V} (g_L \mu_B)^2 \frac{J(J+1)}{3 k_B T} H \tag{1.15}$$

$$\chi = \frac{N}{V} (g_L \mu_B)^2 \frac{J(J+1)}{3 k_B T} = \frac{C}{T} \ . \tag{1.16}$$

Equation (1.16) is known as Curie's law and C is the Curie constant.

Before going on it is important to notice that until now no anisotropic effects have been found. Indeed as long as the J multiplet remains degenerate, Equations (1.6) and (1.8) are not dependent on the direction of the applied magnetic field. Infact if the direction of the magnetic field is changed from $z \to z'$ it is always possible with a rotation to define z' as quantization axis where $|L, S, J, J'_z\rangle$ are linear combinations of $|L, S, J, J_z\rangle$. This rotation, given the degeneracy of $|L, S, J, J_z\rangle$ levels, doesn't affect the system response to the magnetic field given by Equations (1.6) and (1.8).

In order to observe magnetic anisotropy it is thus necessary that degeneracy is removed. This occurs when also crystal field interaction is considered.

1.3 Crystal field interaction

Thus far the magnetic properties of isolated ions have been discussed but to describe the behavior of ions surrounded by other atoms, the effects of the neighboring atoms have to be considered.

When an ion is embedded in a solid the surrounding charge distribution, described by $\rho(\mathbf{r})$, produces an electric field which acts on its electronic charge distribution $\rho_0(\mathbf{r})$. The crystal field Hamiltonian term $\mathcal{H}_{cf}$ accounts for this interaction through:

$$\mathcal{H}_{cf} = \int \rho_0(\mathbf{r}) V_{cf}(\mathbf{r}) \mathrm{d}^3 r \tag{1.17}$$

where

$$V_{cf}(\mathbf{r}) = \int \frac{\rho(\mathbf{r}')}{|\mathbf{r} - \mathbf{r}'|} \mathrm{d}^3 r' \tag{1.18}$$

which, switching to polar coordinates $\mathbf{r} = (r, \theta, \phi)$ and $\mathbf{r}' = (r', \theta', \phi')$, can be expanded in spherical harmonics $Y_k^q(\theta, \phi)$:

$$V_{cf}(r, \theta, \phi) = \sum_{k=0}^{\infty} \sum_{q=-k}^{k} A_k^q \, r^k \, Y_k^q(\theta, \phi) \tag{1.19}$$

with

$$A_k^q = \frac{4\pi}{2k+1} \int \frac{\rho(r')(-1)^q \, Y_k^{-q}(\theta', \phi')}{r'^{k+1}} \mathrm{d}^3 r' \; . \tag{1.20}$$

Equation (1.19) can be read as arising from the interaction of the multipoles $r^k \, Y_k^q(\theta, \phi)$ of the ion electrons with the appropriate components of the electric field A_k^q generated by the surrounding charges.

As shown by Stevens,[15] by applying the Wigner-Eckart theorem it is possible to express the crystal field interaction in terms of the angular momentum operators through the Stevens operators $O_k^q(\mathbf{J})$ and the crystal field parameters B_k^q:

$$\mathcal{H}_{cf} = \sum_{k} \sum_{q=-k}^{k} B_k^q O_k^q(\mathbf{J}) \tag{1.21}$$

with k assuming only even values $k \leqslant 2l$.[16] Crystal field parameters can in principle be calculated, yet since charge density on the surroundings of an

ion is not easy to determine with the necessary accuracy more often B_k^q are regarded as parameters to be determined from experiments. Stevens operators instead can be found tabulated in several works.[16–18]

Thus starting from the Hamiltonian $\mathcal{H} = \mathcal{H}_{ion} + \mathcal{H}_{so}$ the ground state is represented by a J multiplet composed of $2J+1$ degenerate levels characterized by the quantum number J_z[†]. These projections of J can be affected differently by the crystal field, thereby removing the $(2J+1)$ degeneracy of the ground state.

Instead of using Equation (1.21) let us introduce the widely used approximation representing the crystal field interaction as quadratic form:[17]

$$\mathcal{H}_{cf} = \mathbf{J} \cdot \mathbf{D} \cdot \mathbf{J} \ , \tag{1.22}$$

where $\mathbf{D}$ is a real, symmetric tensor thus it possesses three orthogonal eigenvectors and Equation (1.22) can be written as:

$$\mathcal{H}_{cf} = D_{xx}\mathbf{J}_\mathbf{x}^2 + D_{yy}\mathbf{J}_\mathbf{y}^2 + D_{zz}\mathbf{J}_\mathbf{z}^2 \ . \tag{1.23}$$

Introducing the quantities $D = D_{zz} - \frac{1}{2}D_{xx} - \frac{1}{2}D_{yy}$ and $E = \frac{1}{2}(D_{xx} - D_{yy})$ it is possible to obtain from Equation (1.23):

$$\begin{aligned} \mathcal{H}_{cf} &= D\mathbf{J}_\mathbf{z}^2 + E(\mathbf{J}_\mathbf{x}^2 - \mathbf{J}_\mathbf{y}^2) \\ &= D\mathbf{J}_\mathbf{z}^2 + \frac{E}{2}(\mathbf{J}_+^2 + \mathbf{J}_-^2) \end{aligned} \tag{1.24}$$

where $\mathbf{J}_\pm = \mathbf{J}_\mathbf{x} \pm i\mathbf{J}_\mathbf{y}$ are the ladder operators.

It is easy to show that crystal field representation given by Equation (1.24) represents an approximation of the one expressed in terms of Stevens operators (1.21). Indeed considering only the second order terms in Equation (1.21) (the first order $k = 0$ term shifts all the levels by the

[†]In this case we're considering the situation in which spin-orbit coupling is stronger than crystal field interactions so $\mathcal{H}_{cf}$ acts on the eigenstates defined by $\mathcal{H}_{ion} + \mathcal{H}_{so}$. On the opposite if $|\mathcal{H}_{cf}| \gg |\mathcal{H}_{so}|$ is more convenient first to consider crystal field interactions acting on $(2S+1)(2L+1)$-fold degenerate states of $\mathcal{H}_{ion}$ and subsequently apply the spin-orbit coupling.

same amount, therefore it may be omitted) $O_2^0 = 3\mathbf{J_z^2} - J(J+1)$ and $O_2^2 = \frac{1}{2}(\mathbf{J_+^2} + \mathbf{J_-^2})$ one obtains the Hamiltonian in Equations (1.24) where $D = 3B_2^0$ and $E = B_2^2$.

Whatever the level structure is, it is anyway possible to state that if J is integer eigenstates resulting after applying crystal field interaction present no degeneracy while if J is half-integer levels are double degenerate. This is a consequence of Kramers theorem[19] and the pairs of degenerate levels are called Kramers doublets.

As said before, including crystal field interactions brings to the onset of magnetic anisotropy. As a consequence the magnetization is no more isotropic and the response to applied magnetic fields is described by:

$$M_i = \sum_j \chi_{ij} H_j \qquad i,j = x,y,z \tag{1.25}$$

with χ_{ij} the magnetic susceptibility tensor.

1.4 Blocking of magnetization and relaxation processes

Magnetic anisotropy is at the origin of the blocking of magnetization in SMMs which manifests as retaining of a magnetization state for a long time.

Consider the crystal field term in Equation (1.24) in a situation of pure axial symmetry (i.e. $D_{xx} = D_{yy}$, $D = D_{zz}$ and $E = 0$). Equation (1.24) becomes:

$$\mathcal{H}_{cf} = D_{zz}\mathbf{J_z^2}\,. \tag{1.26}$$

The Hamiltonian in Equation (1.26) is diagonal in the $|J, L, S, J_z\rangle$ basis, the eigenvectors are pure $\mathbf{J_z}$ states and J multiplet is split in states degenerate in J_z. This gives rise to the double-well potential profile, typical of SMMs, with the lowest energy levels the ones with the smallest $|J_z|$ if $D > 0$ and the ones with the greater $|J_z|$ if $D < 0$. The first case (D positive) corresponds to easy-plane magnetic anisotropy while negative D describes systems with easy-axis magnetic anisotropy.

In an easy-axis situation the ground state is so defined by $|J, J_z\rangle$ and $|J, -J_z\rangle$ lying on different wells. Suppose the system is *prepared* populating only one of the two ground state levels (for example by applying a magnetic field along z), given that Hamiltonian (1.26) possesses no out-of-diagonal elements no admixing of levels are present so tunneling is inhibited and the only way to relax and restore equilibrium is via thermal assisted processes represented by spin-phonon coupling whose relaxation rate can be described by the Arrhenius law:

$$\tau = \tau_0 e^{|D|J_z^2/k_B T} \ . \tag{1.27}$$

If $E \neq 0$ the second term in Equation (1.24) removes further the degeneracy in J_z and at the same time admixes sates with different J_z values so the eigenvectors are no more pure $\mathbf{J_z}$ states given that the Hamiltonian now possesses also out-of-diagonal elements. One of the consequences of having eigenstates constituted by admixing of J_z levels is the possibility of tunneling between states belonging to one potential well, determined by the D term, with states belonging to the other. This creates another relaxation path efficient at low temperatures.

In general every contribution which breaks the ideal axial symmetry can give rise to tunneling processes. This include for example transverse magnetic fields. The magnetic fields acting on the ion energetic structure can be external but, in order to adequately treat tunneling processes, also internal magnetic fields can be relevant. These internal fields can be originated by hyperfine interactions between the magnetic moment of the nuclei and the electron spins as well as by dipole interactions between spins of different molecules.

Equation (1.24) represents in many situations a good approximation which allows a correct description of the anisotropy properties of SMMs. Even so terms of order higher than second, which are neglected in Equation (1.24), also if small can hold an important role in tunneling processes.

In order to obtain an efficient SMM it is thus important that the molecule possesses a double degenerate ground state presenting bistability, a low transverse anisotropy to inhibit tunnel processes of relaxation and high energy separation between the ground doublet and first excited multiplets to make less efficient thermally assisted mechanisms.

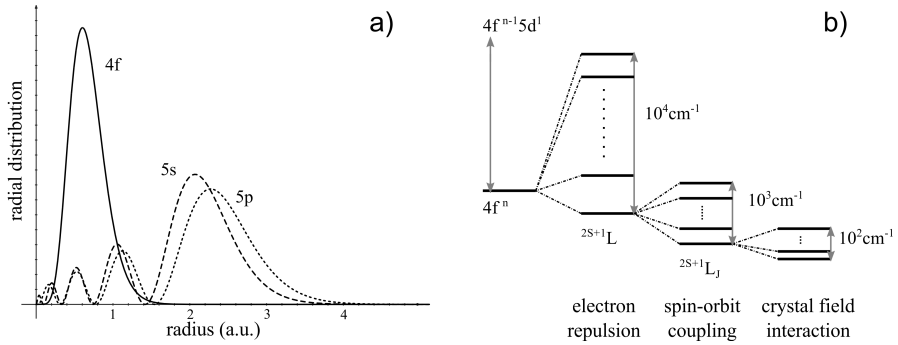

Figure 1.1: a) Comparison of the radial distributions of $4f$, $5s$ and $5p$ orbitals in function of distance from nucleus in atomic units; b) qualitative representation of energy levels in a rare-earth ion and their splitting as interaction are introduced: electron-electron interactions (which provide an energy separation of the order of $10^4\,\mathrm{cm}^{-1}$), spin-orbit coupling (energy separation ca. $10^3\,\mathrm{cm}^{-1}$) and crystal field interaction (energy separation ca. $10^2\,\mathrm{cm}^{-1}$).

1.5 Magnetic properties of rare-earth trivalent ions

The magnetic anisotropy characterizations presented in this work mostly concern magnetic molecules comprising trivalent ions belonging to the rare-earths. This section provides a description, on the base of what previously seen, of the magnetic properties of the lanthanide ions that will be encountered in the next chapters.

The term rare-earths describes the chemical elements whose atomic number ranges from 57 to 71. The complexes studied for this work involve the tripositive ions Tb^{III}, Dy^{III}, Ho^{III}, Er^{III}, Tm^{III} and Ym^{III} characterized by the electronic configuration $[Xe]4f^n$ which means that the incomplete subshell responsible for the magnetic properties is represented by the orbitals $4f$. As shown in Figure 1.1 a the $4f$ electrons are well embedded within the atom and shielded by the $5s$ and $5p$ states from the surroundings. As a consequence of the screening provided by the $5s$ and $5p$ electrons, the extent of the crystal field interactions is smaller than the spin-orbit coupling one as schematized in Figure 1.1 b. In such a situation first the Hamiltonian $\mathcal{H}_{ion} + \mathcal{H}_{so}$ is considered and then the crystal field interaction is added.

	Tb^{III}	Dy^{III}	Ho^{III}	Er^{III}	Tm^{III}	Yb^{III}
f^n	f^8	f^9	f^{10}	f^{11}	f^{12}	f^{13}
$^{2S+1}L_J$	$^7F_6$	$^6H_{\frac{15}{2}}$	$^5I_8$	$^4I_{\frac{15}{2}}$	$^3H_6$	$^2F_{\frac{7}{2}}$
g_L	$\frac{3}{2}$	$\frac{4}{3}$	$\frac{5}{4}$	$\frac{6}{5}$	$\frac{7}{6}$	$\frac{8}{7}$

Table 1.1: $4f$ electronic configurations, LS ground state terms and g_L values of tripositive ions encountered in this work.

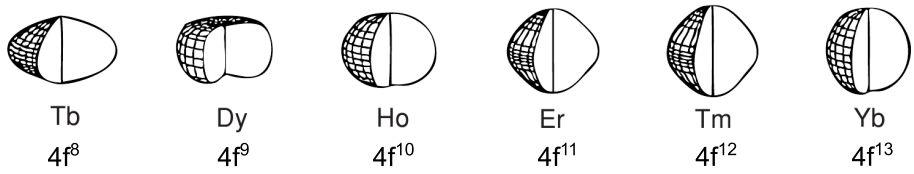

Figure 1.2: Charge density distributions for the trivalent rare-earth ions.

In Table 1.1 are reported the electronic configurations, the Russel-Saunders terms and the Landé factors characterizing the ground state of the Hamiltonian $\mathcal{H}_{ion} + \mathcal{H}_{so}$ for the rare-earth ions considered while in Figure 1.2 are illustrated their electric configurations.

Given the electrostatic nature of crystal field interactions, the charge distribution of the $4f$ electrons plays a relevant role in defining the magnetic anisotropy of the system. Starting from this consideration Rinehart and Long[20] proposed a qualitative method to determine the magnetic anisotropy of a SMM based on the correlation between prolate/oblate distribution of ion electron density and ligand geometry. This method predicts the presence of an easy axis type anisotropy if ions presenting an oblate charge distribution (such as Tb^{III}, Dy^{III} and Ho^{III}) are embedded in an axially "sandwich" type ligand geometry (i.e. the ligand electron density is concentrated above and below the ion one); if instead the ion has a prolate charge distribution (such as Er^{III}, Tm^{III} and Ym^{III}) an easy axis anisotropy is provided by an equatorial geometry of the ligand (see Figure 1.3).

At the base of this model there is the requirement of a ligand with axial geometry: as it will be shown, once this requirement is missed also a

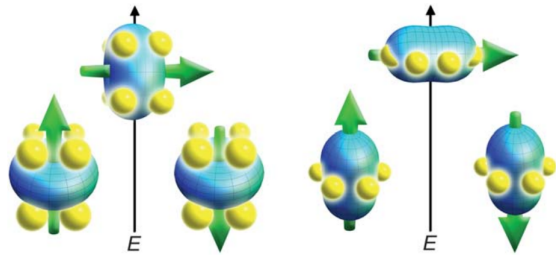

Figure 1.3: Representation of low- and high-energy configurations of the $4f$-orbital electron density with respect to the crystal field environment for an oblate (left) and prolate (right) electron density following Rinehart and Long. The green arrow represents the orientation of the total orbital momentum **J**. For the oblate electron density, an axial "sandwich"-type crystal field an easy-axis anisotropy is energetically favored. In the prolate electron density case, the presence of an easy-axis is provided by an equatorial electron configuration of the ligand. Image from Rinehart and Long paper. [20]

small deviation from the axial symmetry can produce relevant effects on magnetic anisotropy.

2 Methodology

The experimental techniques to measure the magnetization of a sample can be divided into two great families: the inductive methods and the force methods. The working principle of the first ones is based on the variation of magnetic flux generated inside a coil by the sample which induces an electromotive force whose analysis allows to determine the magnetic moment of the sample. In magnetometers based on force method the torque exerted on a magnetic material when immersed in a magnetic field is instead exploited.

In this work methods belonging to both typologies have been used: a superconducting quantum interference device (SQUID) magnetometer and an AC susceptometer belonging to the inductive methods and a capacitive cantilever able to measure the magnetic torque.

A description of the SQUID magnetometer used is given in section 2.1. AC susceptometry is presented in section 2.2 while the horizontal rotator (a particular sample-holder which allows to rotate samples inside the magnetometer in order to characterize their angular dependence of magnetization) is described in section 2.3 along with the mathematical approach followed to analyze data collected with the horizontal rotator. Section 2.4 is instead dedicated to the description of the capacitive cantilever.

2.1 SQUID magnetometer

This section covers the description of the main components of a SQUID magnetometer and its operating principles. Readers interested in specific aspects can refer to specialized texts such as the book of Clarke and Braginski.[21]

The heart of a SQUID magnetometer is constituted by a closed superconducting loop with one or two Josephson junctions. Since two of the peculiarities of superconductors are that (i) a magnetic flux enclosed in a superconductive loop is quantized in unit of flux quantum $\Phi_0 = \frac{h}{2e} \approx 2.07 \times 10^{-15}\,\mathrm{Wb}$ (here h is Planck's constant and e is the electron charge) and (ii) the current flowing through Josephson junctions is periodic in magnetic flux with period equal to Φ_0, SQUID magnetometers are very sensitive instruments capable of resolving changes in external magnetic flux of the order of Φ_0.

The magnetometer used for the magnetic measurements in this work is a Quantum Design MPMS-XL5. This magnetometer allows to perform measurements in a range of temperature spanning from 1.9 K to 400 K and with applied magnetic fields up to ± 5 T. In Figure 2.1 is shown the cryogenic probe comprising the principal components of the magnetometer:

- the sample space and temperature control;
- the superconducting magnet;
- the detection coils;
- the SQUID.

Since the SQUID and the magnet are superconductive elements, the cryogenic probe is immersed in a liquid helium bath inside a dewar not shown in Figure 2.1 along with the magnet power supply, the vacuum pump and the computer used to manage the magnetometer.

2.1.1 The sample space and temperature control

The sample space (**10** in Figure 2.1) is located inside three concentric tubes (**9, 13, 15**). The two outer, separated by a sealed and evacuated region and containing reflective superinsulation, prevent heat exchange between the sample chamber and the helium bath. The inner tube is the sample chamber tube and is separated from the others by the cooling annulus (**12**). Two thermometers and one heater are situated at the bottom of the sample chamber. Temperature control is obtained by heating the sample chamber with the heater or cooling it with cold gas drawn

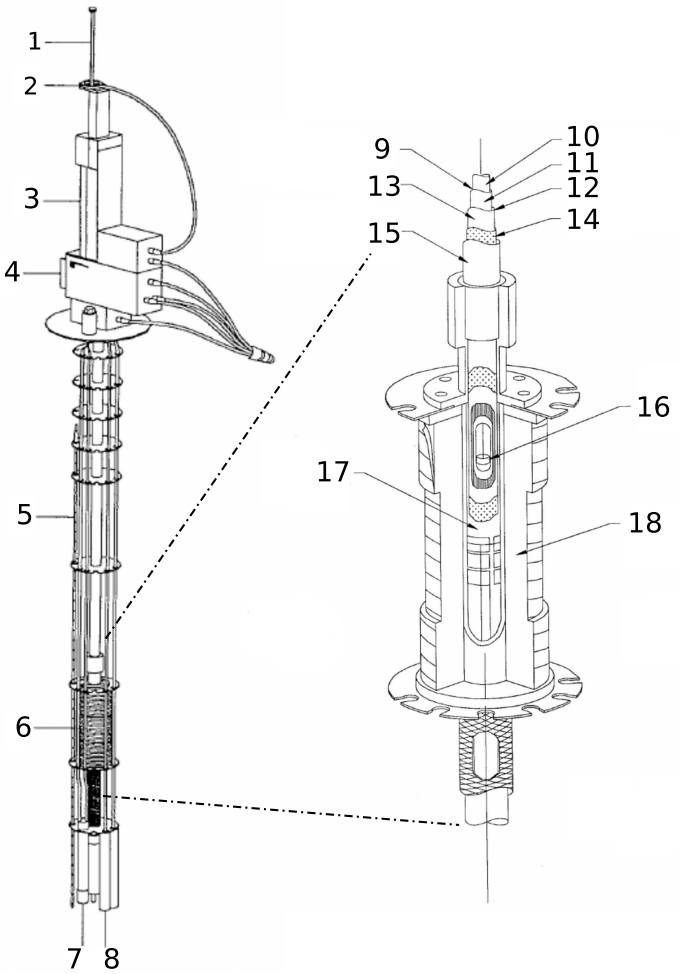

Figure 2.1: Cryogenic probe of MPMS XL QD. **1** Sample rod; **2** sample rotator; **3** sample transport; **4** probe; **5** helium level sensor; **6,18** superconductive solenoid; **7** flow impedance; **8** SQUID capsule; **9** sample chamber tube; **10** sample space; **11** iso-thermal sheet with heater; **12** annular cooling region; **13** inner vacuum jacket wall; **14** superinsulation; **15** outer vacuum jacket wall; **16** sample; **17** sensing coils.

into the cooling annulus from the helium bath through a needle valve. Longitudinal copper wires along the length of the sample chamber assure thermal uniformity. Feedback provided by the two thermometers allows a fine control of temperature stabilization procedure and, at the same time, gives readings of the temperature inside the sample space. With this temperature control system the magnetometer can operate at temperatures between 1.9 K and 400 K.

The sample is placed inside the sample chamber by means of a sample rod (**1**) made of stainless steel in the upper part (because of its strength and low thermal conductivity) and of a silicon copper alloy in the bottom section (to minimize spurious magnetic signals caused by the sample rod). To avoid the presence of air (oxygen is paramagnetic and could compromise the correctness of measurements) or humidity which could condensate inside the sample space due to the cryogenic temperature, a low pressure atmosphere of helium boiled from the dewar has to be maintained inside the sample tube. For this reason the upper side of the sample space is sealed with a ball valve and the rod with the sample before entering inside the magnetometer undergoes a purge procedure in an airlock where air is substituted with gaseous helium.

2.1.2 The superconducting magnet

Samples inside the magnetometer are magnetized by a static magnetic field generated by a superconducting solenoid composed of a niobium alloy (**6, 18**) which can provide magnetic fields up to ± 5 T. Solenoidal geometry makes sure that the sample located at the center of the magnet is subject to an uniform field.

One of the features of the magnet is that it constitutes a closed superconductive loop. This means that once it is charged with the desired current it can operate maintaining a stable field without external current or power supply. In order to keep it in a superconductive state the magnet is located outside the outer jacket of the sample tube so it is always immersed in liquid helium.

Changing the magnetic field corresponds to changing the current flowing inside the magnet but in order to do so, the superconducting loop has to be interrupted, through a switch. The switch is constituted by a small heater wrapped around a segment of the magnet's superconductive wire. When the

heater is energized the segment of wire within the heater becomes normal (no longer superconductive) opening in this way the closed superconducting loop. At this stage a power supply attached to each side of the switch can change the current inside the magnet. Once the new value of current is set the heater is switched off, the superconductive loop is closed again and the magnet can operate without the contribution of the power supply. During this procedure a correct management of the current by the power supply is of crucial importance. If the current supplied is considerably different from that flowing in the magnet or higher than the critical value a magnet quench can occur. When this happens a portion of the superconducting wire becomes normal and, due to the Joule's effect, generates heat that can cause transition to the normal state in an other portion of the magnet giving rise to a domino effect which can eventually bring the entire superconductive wire to the normal state with damaging consequences for the magnet.

A quench can also occur if the helium level in the bath is too low so that the magnet is no longer maintained under the superconductive critical temperature. For this reason caring for regular helium refills is requested to the operator.

2.1.3 The detection coils

Magnetic moment detection is entrusted to the detection coils placed outside the sample tube at the center of the magnet (**17**). Its operating principle is based on Faraday's law which states that the induced electromotive force (emf) in a closed circuit is equal to $-\frac{\mathrm{d}\Phi}{\mathrm{d}t}$ where Φ is the magnetic flux enclosed by the circuit. When the sample is moved (by means of a stepping motor **3**) through the coil the consequent variation of magnetic flux induces a current inside the circuit proportional to the magnetization of the sample.

The detection coils are made of a single superconducting wire wound in a second order gradiometer geometry with a total length of approximately 3 cm consisting of a series of three sets of coils: the upper and bottom sets of N rounds wound clockwise while the center set of $2N$ rounds wound counterclockwise. The choice of such geometry makes it possible to eliminate spurious contributions coming from fluctuation of the magnet: since the field of the magnet is uniform the flux change in the outer rounds is exactly balanced by the flux change in the middle ones. In this way only

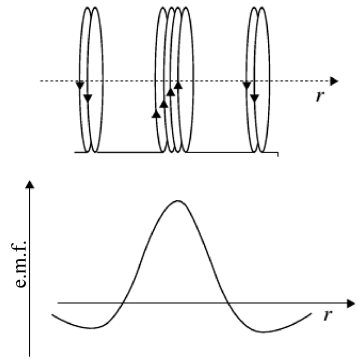

Figure 2.2: Up: second order gradiometer coils scheme; down: induce emf as function of sample position.

the flux changes coming from the moving of the sample inside the detection coils are relevant for the measurement. A schematic view of a second order gradiometer and of the induced emf in shown in Figure 2.2.

2.1.4 The SQUID

The magnetic moment of the sample is not directly determined by measuring the current induced inside the detection coils. Detection coils are instead inductively coupled to a rf-SQUID constituted by a superconductive loop with one Josephson junction (that is an interruption in the superconducting loop which can be made with a thin isolating barrier, a short section of a normal metal or a physical constriction in the loop).

The SQUID functioning is based on Josephson effect postulated by Brian Josephson in 1962[22] and which earned him a Nobel Prize in Physics in 1973. It consists in carriers tunneling between two superconductors (1 and 2) coupled by a weak link (the junction) which give rise to a current:[23]

$$I = I_0 \sin(\vartheta_2 - \vartheta_1) = I_0 \sin(\delta) \ , \tag{2.1}$$

where I_0 is the critical current of the junction while $\delta = \vartheta_2 - \vartheta_1$ is the difference of phases between the wave functions in superconductor 1 and 2

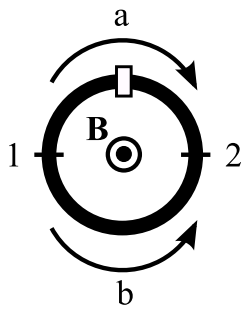

Figure 2.3: Scheme of a single Josephson junction squid in a magnetic field **B**. Phase difference in wave function from point 1 to 2 doesn't depend on the choice of path a (including the junction) or b.

respectively.[†]

In the presence of a magnetic field **B** the difference of phases can be expressed as:

$$\delta = (\vartheta_2 - \vartheta_1) - \frac{2e}{\hbar c}\int_1^2 \mathbf{A}\cdot \mathrm{d}\mathbf{l} \ , \tag{2.2}$$

with **A** the vector potential related to **B** by $\mathbf{B} = \nabla \times \mathbf{A}$.

We consider now the SQUID scheme in Figure 2.3. Wave function inside the superconductor presents in points 1 and 2 phases values independent from the choice of path a or b, so:

$$\delta_b - \frac{2e}{\hbar c}\int_b \mathbf{A}\cdot \mathrm{d}\mathbf{l} = \delta_a - \frac{2e}{\hbar c}\int_a \mathbf{A}\cdot \mathrm{d}\mathbf{l} + 2\pi m \ , \tag{2.3}$$

from which it follows:

$$\begin{aligned} \delta = \delta_b - \delta_a &= -\frac{2e}{\hbar c}\oint \mathbf{A}\cdot \mathrm{d}\mathbf{l} + 2\pi m \\ &= -\frac{2e}{\hbar c}\Phi + 2\pi m = -\frac{2\pi\Phi}{\Phi_0} + 2\pi m \ . \end{aligned} \tag{2.4}$$

Substituting in (2.1) we obtain:

$$I = -I_0 \sin\Big(\frac{2\pi\Phi}{\Phi_0}\Big) \ . \tag{2.5}$$

[†]Superconductivity represents a macroscopic quantum phenomenon: all the carriers (the Cooper pairs) are condensed in a single macrostate which can be described by a single wave function $\psi = \sqrt{\rho}\exp(i\theta)$ where ρ is the density of carriers.

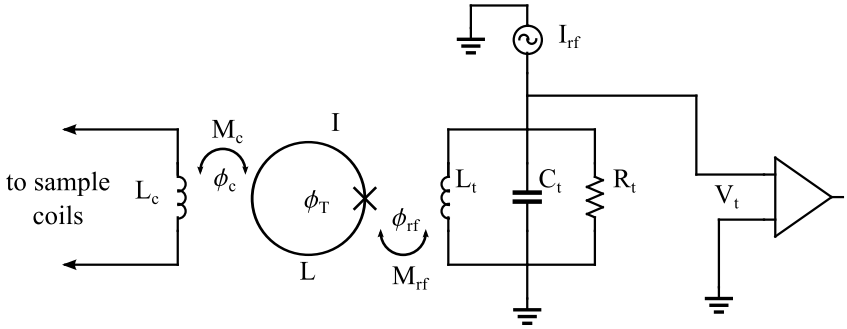

Figure 2.4: Diagram of a rf-SQUID circuit.

Equation (2.5) states that, in the presence of a magnetic field **B**, a current is induced inside the SQUID periodic in the total flux enclosed by the ring Φ with period equal to Φ_0.

In Figure 2.4 is shown a diagram of a rf-SQUID circuit. The SQUID is inductively coupled to the sample coils by means of L_c which generates a magnetic flux Φ_c inside the SQUID proportional to the signal coming from the sample. So the total flux Φ_T inside the SQUID is (here L is the inductance of the SQUID ring):

$$\Phi_T = \Phi_c + LI = \Phi_c - LI_0 \sin(2\pi\Phi_T/\Phi_0) \ . \tag{2.6}$$

Consider now the radio-frequency part of the device (which gives it the name). SQUID is inductively coupled to a tank circuit $L_tC_tR_t$ through the mutual inductance $M_{rf} = k(LL_t)^{1/2}$ and driven to its resonant frequency $\omega_{rf} = (L_tC_t)^{-1/2}$ by a current $I_{rf}\sin(\omega_{rf}t)$ supplied by a generator. Usually ω_{rf} varies in the radio-frequency domain from 20 MHz to 10 GHz.

Since the current I_t flowing through L_t is dependent on magnetic flux in the SQUID through $I_t = \Phi_T/M_{rf}$, the peak value of voltage V_t across the tank circuit is:

$$V_t = \omega_{rf} L_t \frac{\Phi_T}{M_{rf}} \ . \tag{2.7}$$

A pre-amplified reading of V_t constitutes the output of the rf-SQUID that, given its dependence on the flux inside the SQUID in its turn periodic in Φ_0 (see Equation (2.6)), allows very sensitive measurements.

Further and detailed information on rf-SQUID can be found in the already cited book of Clarke[21] or in the original article by Zimmerman.[24]

Being a superconducting element, SQUID needs cryogenic temperature to operate regularly: for this reason it is placed outside the sample chamber in the helium bath (**8** in Figure 2.1). SQUID and couplings to sample coils and rf circuit, given their high sensitivity to magnetic flux changes, are also magnetically shielded from the superconductive magnet by a superconducting shield.

2.2 AC susceptometry

A quantity often measured in order to characterize the magnetic behavior of a sample is its magnetic susceptibility defined as:

$$\chi = \frac{\partial M}{\partial H} \ . \tag{2.8}$$

The magnetometer as described above allows to apply a constant magnetic field H and measure the magnetization $M(H)$ of the sample immersed in it. This type of measurement is also known as DC magnetic measurements and values for the susceptibility are determined as $\chi = \frac{M}{H}$. For low values of applied magnetic field the two ways of obtain χ are equivalent but in general M dependence on H is not linear and $\frac{\partial M}{\partial H} \neq \frac{M}{H}$.

AC susceptometry is a technique able to perform more precise measurements of χ closest to the definition given in Equation (2.8). In an AC magnetic the measurement of the current inside the detection coil is not induced by movement of the magnetized sample but by a time dependent magnetic moment of the sample (maintained fixed inside the detection coil) induced by an oscillating magnetic field. A coil, external to the detection coil, driven by an alternating current generates a small oscillating field whose amplitude usually doesn't exceed 10 Oe. The detection coil consists instead of a pair of winding wound in opposite direction in a first-order gradiometer geometry: in this way the current induced in absence of sample is null. To avoid effects due to a non-perfect coils balance a two-step measurement is usually performed: the sample is first measured in the

middle of the first winding and then in the middle of the second one. AC option is provided in the instrument used by an AC driven coil coaxial to the superconductive magnet, while the middle and the bottom winding of DC detection coils serve as AC detection coils.

A major concern in the design of an induction coil susceptometer is the parasitic capacitance present throughout the coil system, which limits the frequency range of the AC-susceptometer. The inductance, resistance and parasitic capacitance results in a resonant frequency that must be above the highest measurement frequency. This implies, for a given AC-probe, that the frequency range accessible is restricted (usually to four decades).

It is also possible to apply a static field H_0 parallel to the oscillating one so that the total field on the sample is:

$$H = H_0 + \Delta H = H_0 + h\cos\omega t \tag{2.9}$$

where h is the amplitude of the oscillating field and ω its frequency. Sample magnetization in function of the time dependent field ΔH can be expressed as:

$$\begin{aligned} M(H) = M(H_0 + \Delta H) &= M(H_0) + \frac{\partial M}{\partial H}\Delta H \\ &= M(H_0) + \chi\, h\cos\omega t\ . \end{aligned} \tag{2.10}$$

Since H_0 is static and the sample is still inside the coils it doesn't induce any signal in the detection coils and its only effect is to give access to different parts of $M(H)$ curve. The measured signal is instead due to the oscillating component which, as shown in Equation (2.10), is directly related to the susceptibility.

Besides allowing a precise measurement of susceptibility one of the advantages offered by AC susceptometry is the possibility of investigating the dynamics of magnetization by varying the frequency ω. Due to absorption processes depending on frequency, the magnetization of the sample may lag behind the drive field so, thanks to the use of a lock-in detector, an AC susceptibility measurement provides both the in-phase component χ' and out-of-phase one χ'' and susceptibility can be described as $\chi = \chi' + i\,\chi''$. Using the model proposed by Cole and Cole[25] (a generalization of the one originally proposed by Casimir and Du Pré[26]) susceptibility dependence

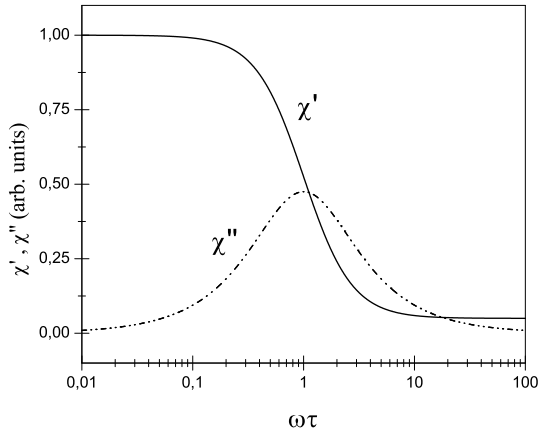

Figure 2.5: Plot of Equations (2.11) for χ' (solid line) and χ'' (dashed line).

on frequency can be described by:

$$\begin{aligned} \chi(\omega) &= \chi_\infty + \frac{\chi_0 - \chi_\infty}{1 + (i\,\omega\tau)^{1-\alpha}} \\ \chi'(\omega) &= \chi_\infty + (\chi_0 - \chi_\infty)\frac{1 + (\omega\tau)^{1-\alpha}\sin(\pi\alpha/2)}{1 + 2(\omega\tau)^{1-\alpha}\sin(\pi\alpha/2) + (\omega\tau)^{2-2\alpha}} \\ \chi''(\omega) &= (\chi_0 - \chi_\infty)\frac{(\omega\tau)^{1-\alpha}\cos(\pi\alpha/2)}{1 + 2(\omega\tau)^{1-\alpha}\sin(\pi\alpha/2) + (\omega\tau)^{2-2\alpha}} \ . \end{aligned} \tag{2.11}$$

In Equations (2.11) τ is the relaxation time needed to restore the thermodynamic equilibrium when the system is subjected to the excitation due to the oscillating field. The parameter α takes into account the situations in which instead of a single value of τ the relaxation process is characterized by a distribution of relaxation times: the wider is the relaxation times distribution the greater is α. The parameters χ_0 and χ_∞ are related to the behavior in the low and high frequency limit: for low values of the field frequency (i.e. $\omega\tau \ll 1$) excitation is so slow that the system can be considered in thermal equilibrium and in Equations (2.11) $\chi = \chi_0$, so χ_0 can be addressed as the isothermal susceptibility. In the opposite limit of high frequency (i.e. $\omega\tau \gg 1$) excitation is so fast that the

system cannot exchange energy with the surroundings and $\chi = \chi_\infty$ (also known as adiabatic susceptibility).

In Figure 2.5 are reported the frequency dependencies of Equations (2.11) for χ' and χ''. While χ' varies monotonically from χ_0 (for $\omega\tau \rightarrow 0$) to χ_∞ ($\omega\tau \rightarrow \infty$), χ'' goes to zero at these extremes and presents a maximum when $\omega\tau = 1$.

From the analysis of AC susceptometry data it is possible to discern if relaxation processes of magnetization are present (in the frequency range accessible to the instrument) and in particular, from the maximum of χ'', estimate the relaxation time $\tau = 1/\omega_{max}$ related to these mechanisms. The possibility of applying static magnetic fields and determining how these affect the relaxation time allows further insight into magnetization dynamic processes. Also characterization of the behavior of τ on varying the temperature can reveal properties related to thermal assisted relaxation mechanisms.

Concerning molecular magnetism AC susceptometry can provide hints regarding the presence of SMM behaviors. Unlike classic paramagnetic mediums, SMMs, due to the presence of an energy barrier, show in fact non zero χ'' in the absence of a static magnetic field. In simple paramagnets, when no static field is applied, each spin is subject to the field of neighboring spins. The application of the small oscillating field only means a precession around a slightly different direction, so relaxation is only due to spin-spin interactions whose relaxation times are of the order of 10^{-9} s. Given that the typical maximum frequency of an AC susceptometer is ca. 100 kHz it follows that spin-spin relaxation is so fast that only the isothermal susceptibility is accessible and the measured χ'' is equal to zero. The ground state of a spin S in SMM is instead constituted, at low temperatures by two degenerate levels, $m = \pm S$, separated by a potential barrier. Neglecting tunneling processes, which occur in a long time scale, relaxation occurs through population of excited levels whose energy separation from the ground state is greater than the spin-spin interaction which in practice become ineffective. In this way slower relaxation processes, usually accessible to AC scusceptometers, are favored leading to a non zero χ'' also in zero static field and it's for this reason that a non-null χ'' is often interpreted as a proof of SMM behavior.

2.3 Angular resolved magnetic measurements with the horizontal rotator

When dealing with crystals the relation linking the magnetization **M** of the sample to the applied magnetic field **H** is given by the general expression:

$$M_i = \sum_j \chi_{ij} H_j \quad , \qquad \boldsymbol{\chi} = \begin{pmatrix} \chi_{xx} & \chi_{xy} & \chi_{xz} \\ \chi_{xy} & \chi_{yy} & \chi_{yz} \\ \chi_{xz} & \chi_{yz} & \chi_{zz} \end{pmatrix} \tag{2.12}$$

where the magnetic susceptibility tensor $\boldsymbol{\chi}$ is a rank 2 tensor with six independent elements whose element χ_{ij} describes the relation between the i magnetization component and the component of field along j.

It is possible to diagonalize the susceptibility tensor, that is to find a new coordinate system in which:

$$M_{i'} = \chi_{i'i'} H_{i'} \quad , \qquad \boldsymbol{\chi} = \begin{pmatrix} \chi_{x'x'} & 0 & 0 \\ 0 & \chi_{y'y'} & 0 \\ 0 & 0 & \chi_{z'z'} \end{pmatrix} . \tag{2.13}$$

Three possibilities can occur:

- $\chi_{x'x'} = \chi_{y'y'} = \chi_{z'z'}$: the susceptibility tensor behaves like a scalar and the medium is isotropous;
- $\chi_{x'x'} = \chi_{y'y'} \neq \chi_{z'z'}$: the medium is uniaxial. If $\chi_{z'z'} > \chi_{x'x'}, \chi_{y'y'}$ the direction along z' is called easy axis of magnetization and $x'y'$ is the hard plane of magnetization; on the contrary if $\chi_{z'z'} < \chi_{x'x'}, \chi_{y'y'}$ z' is the hard axis of magnetization and $x'y'$ is the easy plane of magnetization;
- $\chi_{x'x'} \neq \chi_{y'y'} \neq \chi_{z'z'}$: the medium is biaxial and the easy axis of magnetization is determined by the highest component of the tensor.

By performing angular resolved magnetic measurement it is possible to determine the components of $\boldsymbol{\chi}$ in Equation (2.12). For this purpose, given that the solenoid generating the magnetic field is vertically oriented, a horizontal rotator has been employed, a particular sample holder described

in the next section. Procedures followed to diagonalize the susceptibility tensor experimentally found and determine the principal direction are illustrated in § 2.3.2

2.3.1 The horizontal rotator

The horizontal rotator is a particular sample rod conceived to allow the rotation of the sample inside the magnetometer around an axis perpendicular to the magnetic field direction making it possible to collect magnetic measurements varying the relative angle between the sample and the magnetic field. These kind of experiments have demonstrated to be a powerful tool to study and characterize samples presenting magnetic anisotropy.[27,28]

Referring to the scheme shown in Figure 2.6 the horizontal rotator is constituted by two coaxial rods, **1** and **3**, the first and internal one is free to rotate and driven by a stepper motor while the second is fixed on the magnetometer by the clamp **4**. The rods are made, like the magnetometer sample rod, of stainless steel in the upper part and of a silicon copper alloy in the bottom part. Entering of air inside the magnetometer chamber from the interspace between the two rods is avoided by the seal **2**. The motion of the inner rod is transferred to the sample holder by means of a worm screw which transforms the rotational motion in the translational motion of the shuttle **5**. One end of a $Be_{1.8}Cu_{98.1}$ wire **6** is connected to the shuttle, the other to a spring **7** so that the wire is always in tension. The wire is also threaded through a pulley **9** connected to the sample holder **8**. In this way the translational motion of the shuttle, making slide the wire inside the pulley, is transformed into a rotational motion of the sample holder orthogonal to the axis of the rod.

Measured samples are not directly arranged on the sample holder of the horizontal rotator but first they are fixed with grease on a teflon cube which successively is placed on the horizontal rotator sample holder. The reason for such a choice is given by the procedure followed to determine the susceptibility tensor which involves performing three orthogonal rotations. Given that the biggest dimension of crystals analyzed doesn't exceed 1 mm and that it is not taken for granted at all that a crystal possesses three

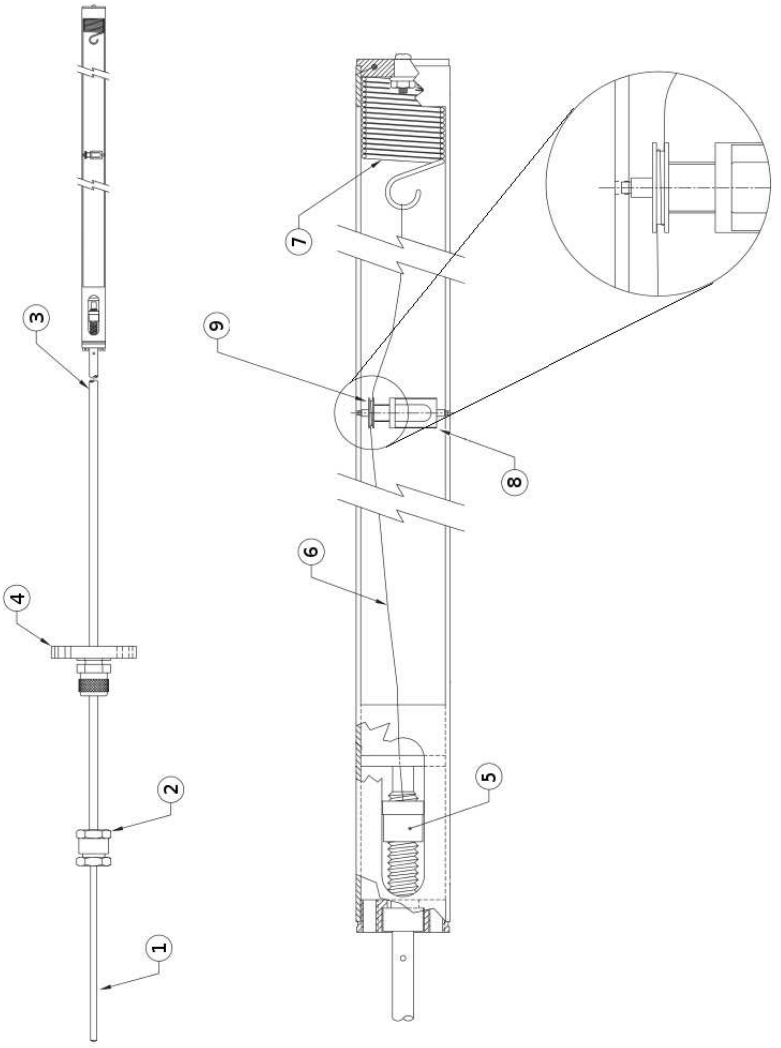

Figure 2.6: Scheme of the horizontal rotator. **1** internal rotating rod; **2** seal; **3** external fixed rod; **4** clamp; **5** worm screw and shuttle; **6** $Be_{1.8}Cu_{98.1}$ wire; **7** spring; **8** sample holder; **9** pulley.

orthogonal faces, the use of a cube has revealed as a good solution to easily manipulate and rearrange the crystal on the sample holder.

The faces of the cube are also labeled defining a right-handed reference frame so that the sample lies on the z-face. In this way three rotations around the x, y and z cube axis allows the determination of the elements of the susceptibility tensor (as shown in the next section) in the reference frame of the cube. Results so obtained are not strictly related to the intrinsic properties of the crystal but rather to the whole crystal-cube system, in fact placing for example the crystal in different positions leads to different values for the susceptibility tensor in the cube reference frame x, y, z. A solution is given by expressing the susceptibility tensor elements in the crystal cell reference frame which is an intrinsic characteristic of the crystal. For this purpose an investigation based on single-crystal X - ray diffraction (in our case performed by using a Xcalibur3 by Oxford Diffraction) makes it possible (i) to determine the orthogonalized unit cell $a, b', c^{*\dagger}$ of the crystal mounted on the cube and (ii) to assign to each face of the cube its Miller's indexes h, k, l related to the crystal orthogonalized unit cell. Once these parameters are known it is possible to express the $\boldsymbol{\chi}$ elements collected in the cube reference frame into a, b', c^* crystal reference frame.

2.3.2 Mathematical model for data processing

This section contains the mathematical approach followed to analyze data coming from measurements with the horizontal rotator in order to determine the components of the susceptibility tensor and its principal directions. Data processing described here has been performed by a program in C written for this purpose.

In Figure 2.7 is shown a schematic representation of how the cube with the sample is placed on the horizontal rotator for each of the three orthogonal rotations performed: RX, RY and RZ which correspond to a configuration with rotation axis parallel to x, y and z cube axis respectively. For each rotation the range between 0° and 270° has been scanned acquiring a measurement of magnetization at each step of 5° obtaining in the end a

[†]Given an unit cell described by the lattice vectors $\mathbf{a}, \mathbf{b}, \mathbf{c}$ the orthogonalized unit cell is defined leaving $\mathbf{a}$ unaltered, taking $\mathbf{b}'$ orthogonal to $\mathbf{a}$ and lying in the ab-plane while $\mathbf{c}^*$ is chosen orthogonal to both $\mathbf{a}$ and $\mathbf{b}'$.

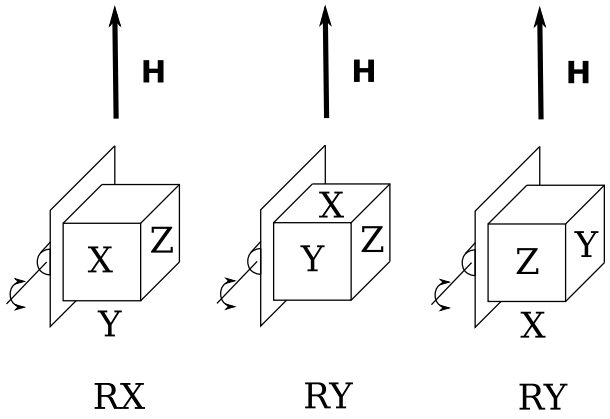

Figure 2.7: Schematic representation of the cube placement on the horizontal rotator sample holder for the rotations around the x, y and z axis of the cube. The arrow indicate the direction of the applied magnetic field $\mathbf{H}$, while the sample lies on the z-face of the cube.

set of $N = 3 \times 55 = 165$ measurements of $M(\theta)$ with θ the angle between the sample holder and the applied magnetic field $\mathbf{H}$.

In order to find the relation linking the value of $M(\theta)$ to the susceptibility tensor elements, let us consider that the magnetic field rotates instead of the sample. This means that considering, for example, the RX configuration $\mathbf{H}$ lies on the yz plane of the cube and can be represented by $\mathbf{H} = (0,\, H\sin(\theta),\, H\cos(\theta))$. From Equation (2.12) it follows that:

$$\begin{aligned}\mathbf{M} = \boldsymbol{\chi}\mathbf{H} &= \begin{pmatrix} \chi_{xx} & \chi_{xy} & \chi_{xz} \\ \chi_{xy} & \chi_{yy} & \chi_{yz} \\ \chi_{xz} & \chi_{yz} & \chi_{zz} \end{pmatrix} \begin{pmatrix} 0 \\ H\sin(\theta) \\ H\cos(\theta) \end{pmatrix} \\ &= H \begin{pmatrix} \chi_{xz}\cos(\theta) + \chi_{xy}\sin(\theta) \\ \chi_{yz}\cos(\theta) + \chi_{yy}\sin(\theta) \\ \chi_{zz}\cos(\theta) + \chi_{yz}\sin(\theta) \end{pmatrix} .\end{aligned} \tag{2.14}$$

Since the magnetization measured by the magnetometer is its projection along the magnetic field, the output value given by the instrument is:

$$\begin{aligned} M_{meas} &= \mathbf{M} \cdot \big(0,\, H\sin(\theta),\, H\cos(\theta)\big) \\ &= H\big(\chi_{zz}\cos^2(\theta) + \chi_{yy}\sin^2(\theta) + 2\chi_{yz}\sin(\theta)\cos(\theta)\big) . \end{aligned} \tag{2.15}$$

Repeating the same for all three configurations we get, in terms of susceptibility measured:

$$\begin{aligned} \text{RX:} \quad & \chi_{zz}\cos^2(\theta) + \chi_{yy}\sin^2(\theta) + 2\chi_{yz}\sin(\theta)\cos(\theta) \\ \text{RY:} \quad & \chi_{zz}\cos^2(\theta) + \chi_{xx}\sin^2(\theta) + 2\chi_{xz}\sin(\theta)\cos(\theta) \\ \text{RZ:} \quad & \chi_{yy}\cos^2(\theta) + \chi_{xx}\sin^2(\theta) + 2\chi_{xy}\sin(\theta)\cos(\theta) \end{aligned} \tag{2.16}$$

These are equations linear in χ_{ij} which can be written as:

$$y(\theta) = \sum_{k=1}^{6} p_k X_k(\theta) \tag{2.17}$$

where $y(\theta)$ is the susceptibility measured, p_k indicates the elements of susceptibility tensor and $X_k(\theta)$ are functions of $\sin(\theta)$ and $\cos(\theta)$. The parameters p_k are obtained with the least square method by minimizing the χ^2 function:[29]

$$\chi^2 = \sum_{i=1}^{N} \left(\frac{y_i - \sum_{k=i}^{6} p_k X_k(\theta_i)}{\sigma_i} \right)^2 \tag{2.18}$$

with σ_i the error associated to the y_i measurement. Finding the minimum of Equation (2.18) means solving the N-elements system comprising the derivatives of χ^2 respect to p_k parameters:

$$\sum_{i=1}^{N} \frac{1}{\sigma_i} \left[y_i - \sum_{j=1}^{6} p_j X_j(\theta_i) \right] X_k(\theta_i) = 0 \qquad k = 1, \ldots, 6 \tag{2.19}$$

which can be written as:[30]

$$(\mathbf{A}^T \cdot \mathbf{A}) \cdot \mathbf{p} = \mathbf{A}^T \cdot \mathbf{b} \tag{2.20}$$

where $\mathbf{p} = [\chi_{xx}, \chi_{yy}, \chi_{zz}, \chi_{xy}, \chi_{yz}, \chi_{xz}]$ is the vector containing the unknown quantities to be determined while $\mathbf{A}$ and $\mathbf{b}$ are respectively a block matrix and a vector defined as:

$$A_{ij} = \frac{X_j(\theta_i)}{\sigma_i} \quad , \qquad b_i = \frac{y_i}{\sigma_i} \, . \tag{2.21}$$

The solution of the linear system (2.20), obtained following the LU decomposition method,[30] returns the best estimation for the susceptibility tensor elements while the error associated is given by the diagonal terms of the covariance matrix $\mathbf{C} = \mathbf{A}^T \cdot \mathbf{A}$.

Once the matrix describing $\boldsymbol{\chi}$ is known, its eigenvalues and the eigenvectors represent respectively the principal values and directions of the system under investigation. Functions in GNU Scientific Libraries `gsl_math.h`, `gsl_eigen.h` and `gsl_vector.h` have been used to obtain the eigenvalues and eigenvectors of $\boldsymbol{\chi}$ while for the estimation of the errors they were considered in the same way as perturbations and propagated at the first order.

As stated in the previous section, it is necessary to express the principal directions found in the unit cell reference frame to become properties characterizing the crystal itself. Having indexed, with the use of the X-ray diffractometer, the teflon cube faces with Miller's indexes makes it possible to know the reciprocal orientation of the x, y, z and a, b', c^* reference frames and so to construct the change of basis matrix $\mathbf{T}$. This matrix is characterized by having as column the basis vectors $\hat{\mathbf{a}}, \hat{\mathbf{b}}', \hat{\mathbf{c}}^*$ expressed in terms of $\hat{\mathbf{x}}, \hat{\mathbf{y}}, \hat{\mathbf{z}}$: $\mathbf{T} = \big(\hat{\mathbf{a}}(\hat{\mathbf{x}}, \hat{\mathbf{y}}, \hat{\mathbf{z}}), \hat{\mathbf{b}}'(\hat{\mathbf{x}}, \hat{\mathbf{y}}, \hat{\mathbf{z}}), \hat{\mathbf{c}}^*(\hat{\mathbf{x}}, \hat{\mathbf{y}}, \hat{\mathbf{z}})\big)$.

Susceptibility tensor $\boldsymbol{\chi}$ and its principal directions $\mathbf{v}_i$ can be reported in the orthogonalized crystal unit cell by:

$$\begin{aligned} \boldsymbol{\chi}(a, b', c^*) &= \mathbf{T}\, \boldsymbol{\chi}(x, y, z)\, \mathbf{T}^{-1} \\ \mathbf{v}_i(a, b', c^*) &= \mathbf{T} \cdot \mathbf{v}_i(x, y, z)\ , \qquad i = 1, 2, 3\ . \end{aligned} \tag{2.22}$$

2.4 Angular resolved magnetic measurements with capacitive torque meter

The methods described in the previous section belong to the family of inductive methods. In this section instead a method will be described based on the magnetic torque $\boldsymbol{\tau}$ exerted on a magnetic sample when immersed in a magnetic field $\mathbf{H}$ and described by the equation:

$$\boldsymbol{\tau} = \mathbf{M} \times \mathbf{H}\ . \tag{2.23}$$

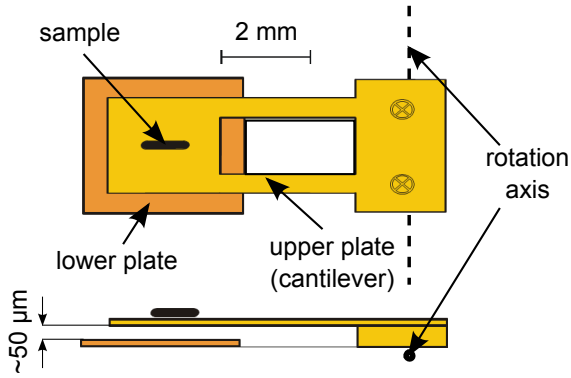

Figure 2.8: Capacitive cantilever scheme.

The technique makes use of a capacitive torque meter whose schematic representation is given in Figure 2.8. The working principle is based on determining the magnetic torque exerted on the sample by a capacitance variation measurement. A lower and an upper plates (the last being the cantilever which serves also as sample holder), separated by a spacer of a distance $d = 50\mu$m, constitute the parallel plates of a capacitor. A very low conductive copper plated epoxy slab acts as support for the system. The double-armed design avoids transverse deflections of the cantilever in order to measure only capacitance variations due to deflections around an axis parallel to the plates surfaces.

Both the plates and the spacer are made of a CuBe alloy (Cu: 98%, Be: 2%). The choice of CuBe alloy was made because it is a non-magnetic material. Furthermore it has a wide operating temperature range which enables it to retain its shape under high loads even at low temperatures.

The whole is mounted on a rod which allows the introduction of the instrument in the center of a superconductive magnet inside a cryostat by Oxford Instruments. The system can supply magnetic vertically oriented magnetic fields up to $\pm 12\,\mathrm{T}$ and work in a range of temperatures from $1.5\,\mathrm{K}$ to $1000\,\mathrm{K}$. In addition a stepper motor can rotate the two-plate system in order to perform measurements at specified angles between the magnetic field and the torque magnetometer.

The capacitance measurements are accomplished by a high-sensitive capacitance bridge by Andeen-Hagerling AH2550A connected through wires

to the cantilever and the lower plate. The resolution of the bridge is 0.8 aF and it can measure capacitances up to 1.5 µF and measurements are performed by applying a 1 kHz ac voltage between 0.3 mV and 15 V (depending on the value of the capacitance measured) across the terminals of the capacitor. Considering the lowest capacitance measurable equal to 0.1 fF (this value takes into account the effects of thermal noise and external vibrations) the smallest torque measurable by the system is 10^{-11}N m.

When the sample mounted on the instrument is placed inside a magnetic field the cantilever deflects from its rest position due the magnetic torque τ. The extent of the deflection is mainly determined by the equilibrium between the magnetic and cantilever elastic torques. If linear elastic response is valid (i.e. the deflection is small)[†] the elastic torque acting on the cantilever, characterized by an elastic constant k_{el} and length l, can be expressed by:

$$\tau_{\mathrm{el}} = k_{\mathrm{el}} l(d - d_0) = k_{\mathrm{el}} l\delta \,, \tag{2.24}$$

where $\delta = d - d_0$ represents the deflection from rest position d_0. Considering now the cantilever as a parallel plate capacitor with capacitance C_0 at rest, the variation ΔC due to the cantilever deflection is given by:

$$C_0 = \frac{\epsilon A}{d_0} \implies \Delta C = \frac{\epsilon A}{d_0^2}\delta = \frac{C_0}{d_0}\delta \,. \tag{2.25}$$

Substituting in Equation (2.24) and considering the equilibrium between magnetic and elastic torque:

$$\tau = k_{\mathrm{el}} l \frac{d_0}{C_0}\Delta C = K\Delta C \,. \tag{2.26}$$

From Equation (2.26) it follows that, in the linear response limit, the torque acting on the cantilever and the variation of capacitance caused by it are linearly related through the constant K which only depends on the characteristics of the cantilever. This means that, given the high sensitivity of the bridge used, from a measurement of capacitance difference the magnetic torque exerted on the sample can be directly known with high accuracy.

[†]For CuBe the response is no longer linear at induced pressures of around 800 MPa.[31] In our magnetic torque measurements the equivalent pressure induced due to the magnetic torque may go up to 100 Pa in an upper limit.

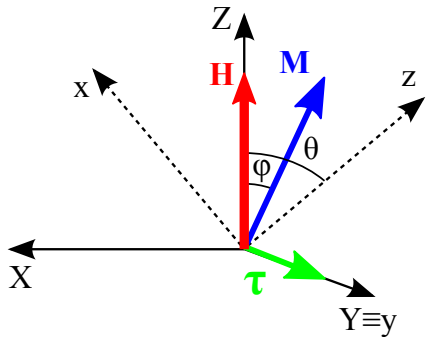

Figure 2.9: Schematic representation of lab reference frame (X, Y, Z) and the cantilever one (x, y, z).

2.4.1 Magnetic anisotropy measurements with capacitive torque meter

The experimental set up used allows the rotation of the cantilever along an axis orthogonal to the applied magnetic field making it possible to collect measurements of the magnetic torque in function of the field-cantilever angle. Identifying the rotation axis with the Y axis of the laboratory reference frame and the magnetic field direction with the Z axis (see Figure 2.9) one obtains the configuration illustrated in Figure 2.9 where x, y, z describe the cantilever reference frame rotating along the $y \equiv Y$ axis.

The geometry of the instrument allows the measurement of only the y component of magnetic torque thus, recalling Equation (2.23), the quantity measured, in the cantilever reference frame, is given by:

$$\tau_y = M_z H_x - M_x H_z \ , \tag{2.27}$$

that, if the field is weak enough to consider the magnetization in linear relationship with the field, can be written as:

$$\tau_y = \chi_z H_z H_x - \chi_x H_x H_z = H^2 \sin\theta \cos\theta (\chi_z - \chi_x) \ . \tag{2.28}$$

Supposing the x and y axis directed along two principal directions of magnetic anisotropy it's possible to compare the previous expression for the torque with the one obtained from magnetic measurements with horizontal rotator which in this situation becomes (see Section 2.3.2):

$$M = H(\chi_z \cos^2\theta + \chi_x \sin^2\theta) \ . \tag{2.29}$$

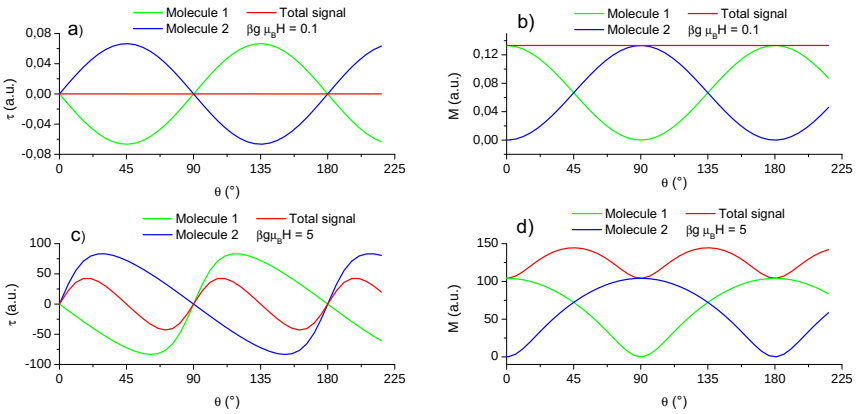

Figure 2.10: Simulations of angular resolved magnetic measurements (red lines) with capacitive cantilever (a and c) and with horizontal rotator (b and d) for two orthogonal Ising-type contributions (individually represented by green and blue lines) in two different regimes: a) and b) linear relationship between M and H ($\beta g \mu_B H = 0.1$ and Equation (2.28) used); c) and d) non-linear magnetization response to the field ($\beta g \mu_B H = 5$ and Equations (2.27) (1.13) considered).

In the presence of magnetic isotropy in the plane xz (i.e. $\chi_x = \chi_z$) a torque measurement gives a result equal to zero for all the angles while the magnetization measured with the horizontal rotator is a constant value equal to $2H\chi_{xz}$. If the system presents instead a magnetic anisotropy in the xz plane, the principal axis direction in torque measurements is easily located at the angles at which the torque crosses the zero; in angular dependent magnetization measurements determination of principal direction is not in general so straightforward as seen in Section 2.3.2.

Consider another situation (similar in certain aspects to the one that will be encountered in Chapter 4): two orthogonal Ising-type ($\chi_x = 0, \chi_z = \chi$) molecules characterized by a spin value 1/2. The measured quantities come from the sum of the two contributions shifted by 90°. In the linear response regime the two techniques of measurement provide respectively:

$$\begin{aligned} \tau &= H^2\chi \sin\theta\cos\theta - H^2\chi\cos\theta\sin\theta = 0 \\ M &= H\chi\cos^2\theta + H\chi\sin^2\theta = H\chi \end{aligned} \tag{2.30}$$

With both methods a constant angular independent quantity is measured

(see Figure 2.10 a and b) so the system descriptions are equivalent. If in the presence of higher $\beta g \mu_B H$, so that M can be considered no more linearly related to H and saturation effects of magnetization are present, the situation is the one shown in the simulation in Figure 2.10 c and d obtained from Equation (2.27) where M is given by the Brillouin function (1.13) and a value $\beta g \mu_B H = 5$ has been considered.

Unlike the previous regime the individual angular dependent torque curves of the two contributions (Figure 2.10 c) show a strong asymmetry, with a steep variation when the field crosses the hard directions.

To give a qualitative description, referring to Equation (2.27), one can notice that even a slight deviation of the field orientation from the hard (x) direction projects a small component along the easy axis (z) able to induce a significant magnetization. This makes the first term of Equation (2.27) quite large and consequently a strong torque is observed. The same does not occur when the field is close to the easy axis (z) because the resulting small component of the field along the hard direction has little effect on the hard component of the magnetization. A more gradual increase of the torque is thus observed around the easy axis. Also for the magnetization measurements (Figure 2.10 d) high $\beta g \mu_B H$ values imply deviation from Equation (2.30) and additional features become visible in the angular dependence. These, however, are superimposed to a strong isotropic signal, whereas torque measurements, as already noticed, are insensitive to isotropic magnetization.

Moreover a small misalignment of the crystal, resulting in rotating not along a principal axis (a situation more common in real experiments), has no significant effect in torque measurements, but can induce a strong spurious modulation of the signal in angular-resolved magnetometry making more difficult the analysis of magnetic anisotropy contributions.

On the other hand in the absence of an external magnetic field the torque is null. This means that torque magnetometry is not a suitable method to study and measure remnant magnetization for example in a magnetic hysteresis loop.

3 The LnDOTA series

In this chapter are presented the results obtained from the magnetic studies conducted on complexes $Na[LnDOTA(H_2O)] \cdot 4\,H_2O$ (**1**) where $DOTA^{4-}$ is the anion of the 1,4,7,10-tetraazacyclododecane-N,N',N'',N'''-tetraacetic acid[32] and Ln indicates ions of Tb^{III}, Dy^{III}, Ho^{III}, Er^{III}, Tm^{III} and Yb^{III}.

As shown in Figure 3.1 the Ln ion is in an idealized capped square antiprismatic environment formed by four oxygen atoms of carboxylate groups and four nitrogen atoms arranged at the corner of two parallel squares and the oxygen atom of a water molecule as capping. The direction identified by the Ln and the oxygen of the water molecule O_w defines a pseudo four-fold symmetry axis.

Only three of the four carboxylate groups are coordinated to the Na^+ ions which themselves are coordinated to two symmetry-related complexes. In addition, the water molecule coordinated to the Ln ion forms hydrogen bonds with oxygen atoms coordinated to the Na^+ ions. These factors limit the tetragonal symmetry only to the first coordination sphere. The complex crystallizes in the triclinic $P\bar{1}$ space group with all the molecules oriented along the same direction (but with opposite sense due to the presence of an inversion center as point group element).

Until 2011 complexes of DOTA and lanthanide ions were studied particularly for their relevance as contrast agents in MRI[33] and for their luminescent properties.[34] They made their entrance in the field of molecular magnetism in 2011 with the article of Car et al.[35] where the first substantial characterization of low temperature magnetic behavior of DyDOTA polycrystalline sample was reported demonstrating the SMM nature of the DyDOTA. The presence was also observed of two competing relaxation

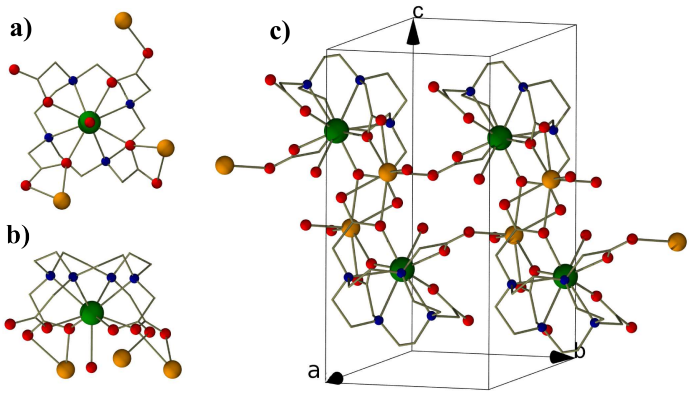

Figure 3.1: Structure of Na[LnDOTA(H_2O)]. On the left two views of the molecule: a) along the pseudo four-fold symmetry axis, b) orthogonal to Ln−O_w bond direction. On the right is shown the molecule packing in the unit cell. Color code: Ln green; O red; N blue; Na yellow; C gray. Hydrogen atoms are not shown for clarity.

processes strongly affected by the presence of an applied static magnetic field: in the absence of a magnetic field a temperature-independent under-barrier mechanism is present while when a weak magnetic field is applied a thermally assisted mechanism is activated with an effective barrier of ca. 60 K and an increase of six orders of magnitude in the relaxation time at 1.8 K, compared to the zero-field one.

Subsequently during my master's degree thesis I studied the magnetic anisotropy of DyDOTA single crystals with angular resolved characterization of magnetization.[36] Thanks to the collinearity shown by all the molecules in the crystal it was possible to determine the principal axis of magnetization of the DyDOTA molecule. Results obtained revealed that the principal axis of magnetization isn't directed along the pseudo-symmetry axis of the molecule (represented by the Ln−O_w bond) but orthogonally to it. Moreover from *ab initio* calculations it followed that the direction of easy axis in the plane orthogonal to the Ln−O_w bond is influenced by the position of the hydrogen atoms belonging to the apical water molecule. This study revealed how interactions between the Dy^{III} ion with the surrounding ligand play a fundamental role on the definition of magnetic anisotropy of the molecules.

	a (Å)	b (Å)	c (Å)	α (°)	β (°)	γ (°)
Tb	8.806	9.138	15.66	82.76	85.40	80.57
Dy	8.719	9.079	15.637	82.962	85.824	81.637
Er	8.719	9.076	15.544	83.33	85.91	82.01
Yb	8.755	9.063	15.634	82.33	85.92	82.33

Table 3.1: Crystallographic unit cell parameters for the Tb, Dy, Er and Yb derivatives determined by single crystal diffraction.

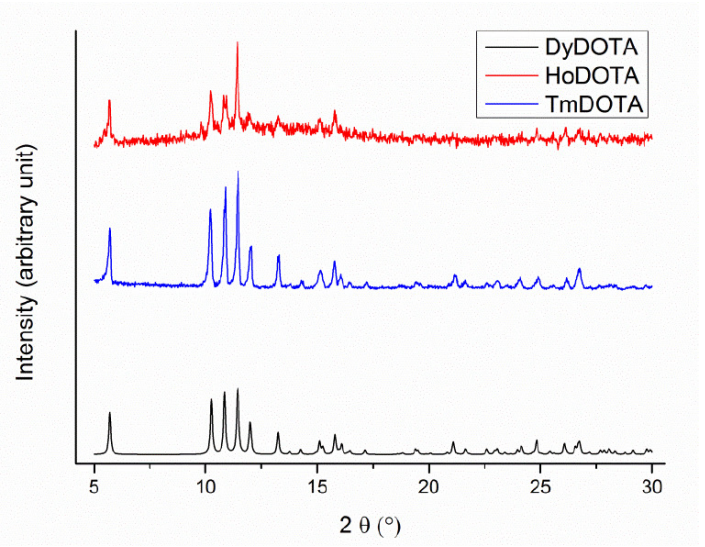

Figure 3.2: X-ray powder diffraction profiles of Ho, Tm and Dy compounds.

In the light of these results and taking advantage of the fact that complexes (**1**) with several Ln^{III} ions are isostructural and stable,[32] also complexes with Tb^{III}, Ho^{III}, Er^{III}, Tm^{III} and Yb^{III} (which, among the lanthanide series, possess the higher J ground state) have been synthesized, following the reported procedure,[37,38] in order to reveal how magnetic anisotropy can be affected by metal-ligand interaction.

Crystals sufficiently big (i.e. with the largest dimension of the order of ca. 1 mm) to be employed in single-crystal magnetic characterization were obtained for Tb, Er and Yb derivatives. Single crystal X-ray diffractometry (see Table 3.1 for the cell parameters) confirmed that the compounds are isostructural. Regarding Ho and Tm derivatives their X-ray powder diffraction profile showed to be superimposable to the Dy one (see Figure 3.2).

Data concerning Dy derivative shown in this Chapter come form my precedent work on DyDOTA single crystals unless otherwise specified.

3.1 Static magnetic measurements

Polycrystalline powder samples, pressed in pellets to avoid reorientation in the field of the microcrystals, of all derivatives have been prepared to study their static magnetic behavior.

In Figure 3.3 are reported the temperature dependence of χT obtained. Data in the range 150 K to 300 K have been fitted using the Curie-Weiss law:

$$\chi = \frac{C}{T - \Theta} \quad \Longrightarrow \quad \chi T = \frac{C}{1 - \frac{\Theta}{T}} \tag{3.1}$$

where C is the same Curie constant as in Equation (1.16) and Θ is the Weiss constant. Equation (3.1) represents a correction to the Curie law (Equation (1.16)), coming from taking into account possible interactions between magnetic moments which reveal themselves at temperatures under Θ where the theory predicts spontaneous magnetization of the system of ferromagnetic nature if $1 - \frac{\Theta}{T} < 1$ or antiferromagnetic if $1 - \frac{\Theta}{T} > 1$.[39]

Results obtained are shown in Table 3.2. Values found for Curie constants are in agreement with the ones expected for tripositive lanthanides ions characterized by the g_L and J listed in Table 1.1. The minus sign in front of critical temperatures Θ suggests the presence of antiferromagnetic interaction. However in the presence of orbitally degenerate states the

Element	C_{th} (emu K mol^{-1})	C_{exp} (emu K mol^{-1})	Θ_{exp} (K)
Tb	11.82	11.79(1)	−4.8(4)
Ho	14.07	14.85(2)	−10.5(3)
Er	11.48	11.56(1)	−13.2(2)
Tm	7.15	7.46(1)	−24.0(5)
Yb	2.57	2.314(2)	−39.2(3)

Table 3.2: Theoretical values of Curie's constant compared to the experimental ones obtained from the fits of χT vs. T measurements (see Figure 3.3). In the third column are reported the values of Curie's temperature Θ.

decrease of χT observed on lowering the temperature is due to the depopulation of the levels belonging to the ground J multiplet split by crystal field.

Magnetization measured in function of a static external magnetic field have been collected at two different temperatures: 2 K and 5 K. In Figure 3.4 are reported the values of magnetization as a function of the reduced variable $\mu_B H/k_B T$. Except for the Yb derivative, measurements collected at the two different temperatures are not superimposable in all the $\mu_B H/k_B T$ range.

From Equation (1.13) and (1.14) it follows that the trend of M with respect to $\mu_B H/k_B T$ is determined by g_L and J values of ground multiplet. This means that, if no other state except the ground J multiplet is populated, $M(\mu_B H/k_B T)$ at different temperatures are superimposable. As shown in section 1.3 the presence of the crystal field interaction splits the J multiplets; Brillouin equation (1.13) can however still be used considering an effective value J_{eff}, determined by the multiplicity of the crystal field multiplet, and the related g_{eff}. The non-superimposability of magnetization curves of Tb, Ho, Er, Tm can be explained by a small energy separation of the first excited crystal field levels so that they can be populated passing from 2 K to 5 K altering the values of J_{eff} and g_{eff}. Magnetization curves of Yb suggest on the contrary a greater energy separation between the two first crystal field levels so that at both temperatures only the ground one can be considered populated and J_{eff} and g_{eff} remain the same as $M(\mu_B H/k_B T)$.

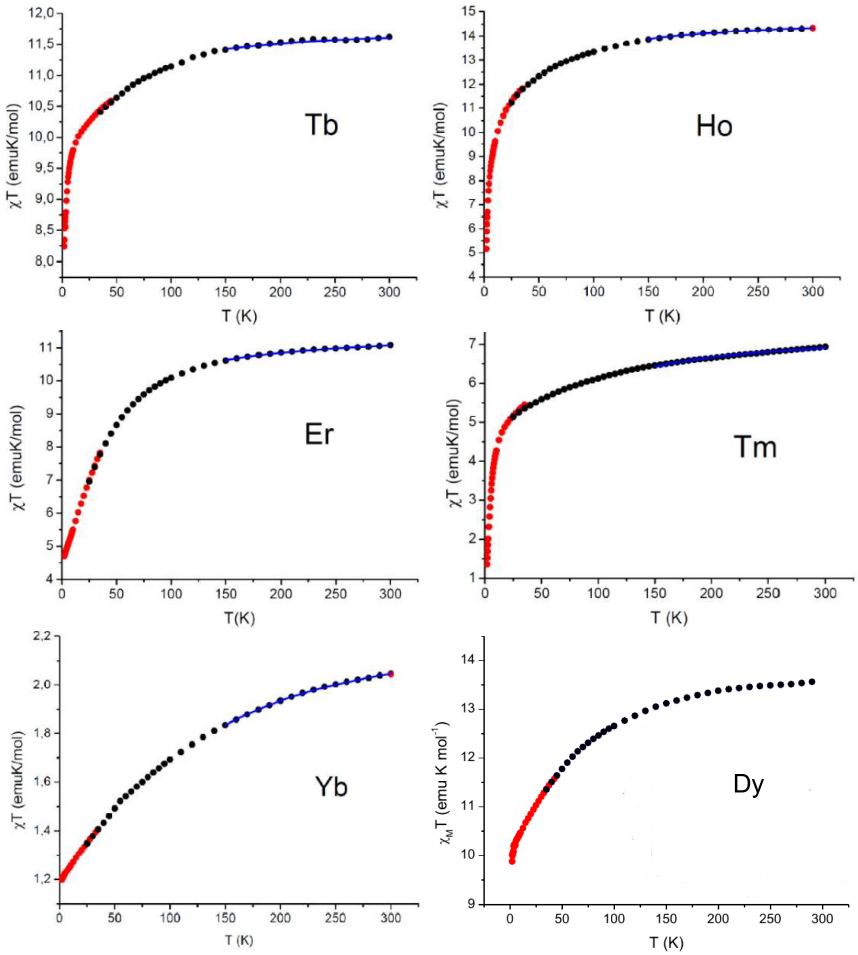

Figure 3.3: Temperature dependence of the χT product for Tb, Ho, Er, Tm and Yb polycrystalline powder samples. The Dy data are from the article of Car et al.[35] Red dots data were taken with $H = 1$kOe while black ones with $H = 10$kOe. The blue line represents the fit considering the Curie-Weiss law in the range from 150 K to 300 K. The results of the fits are reported in Table 3.2.

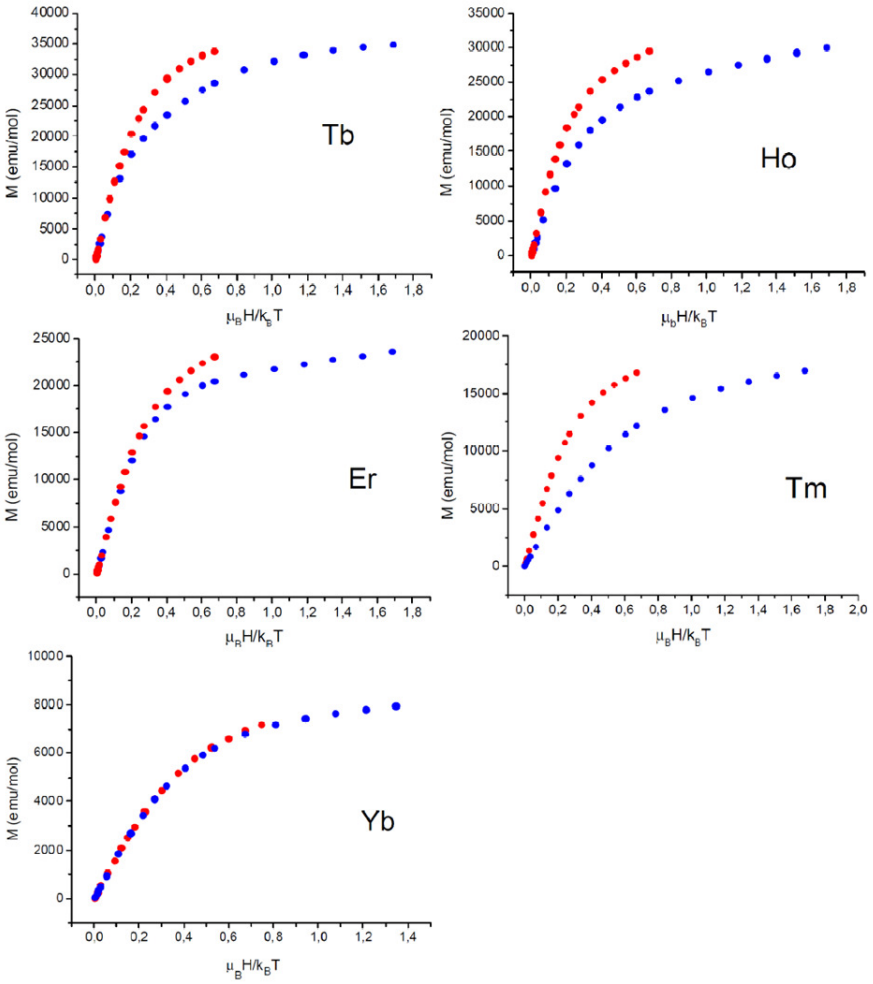

Figure 3.4: Magnetization dependence on reduced variable $\mu_B H/k_B T$ for Tb, Ho, Er, Tm and Yb polycrystalline powder samples. Blue dots data have been measured at 2 K while red ones at 5 K.

Tb	$\hat{\mathbf{x}} = -0.336706\,\hat{\mathbf{a}} - 0.934607\,\hat{\mathbf{b}}' - 0.114625\,\hat{\mathbf{c}}^*$
	$\hat{\mathbf{y}} = -0.947290\,\hat{\mathbf{a}} + 0.286213\,\hat{\mathbf{b}}' + 0.143958\,\hat{\mathbf{c}}^*$
	$\hat{\mathbf{z}} = 0.103404\,\hat{\mathbf{a}} - 0.159987\,\hat{\mathbf{b}}' - 0.981688\,\hat{\mathbf{c}}^*$
Dy	$\hat{\mathbf{x}} = -0.06734\,\hat{\mathbf{a}} - 0.99764\,\hat{\mathbf{b}}' + 0.01363\,\hat{\mathbf{c}}^*$
	$\hat{\mathbf{y}} = -0.99733\,\hat{\mathbf{a}} + 0.05933\,\hat{\mathbf{b}}' - 0.04266\,\hat{\mathbf{c}}^*$
	$\hat{\mathbf{z}} = 0.03680\,\hat{\mathbf{a}} - 0.02717\,\hat{\mathbf{b}}' - 0.99895\,\hat{\mathbf{c}}^*$
Er	$\hat{\mathbf{x}} = 0.032731\,\hat{\mathbf{a}} + 0.999463\,\hat{\mathbf{b}}' + 0.001610\,\hat{\mathbf{c}}^*$
	$\hat{\mathbf{y}} = 0.992334\,\hat{\mathbf{a}} - 0.123014\,\hat{\mathbf{b}}' + 0.011849\,\hat{\mathbf{c}}^*$
	$\hat{\mathbf{z}} = 0.008839\,\hat{\mathbf{a}} - 0.034773\,\hat{\mathbf{b}}' + 0.999356\,\hat{\mathbf{c}}^*$
Yb	$\hat{\mathbf{x}} = -0.002633\,\hat{\mathbf{a}} - 0.111998\,\hat{\mathbf{b}}' - 0.993705\,\hat{\mathbf{c}}^*$
	$\hat{\mathbf{y}} = -0.128189\,\hat{\mathbf{a}} - 0.988734\,\hat{\mathbf{b}}' + 0.077279\,\hat{\mathbf{c}}^*$
	$\hat{\mathbf{z}} = -0.995755\,\hat{\mathbf{a}} + 0.091381\,\hat{\mathbf{b}}' - 0.011055\,\hat{\mathbf{c}}^*$

Table 3.3: Unit vectors normal to x, y and z faces of the cube expressed in the orthogonalized unit cell reference frame a, b', c^* after indexing by single-crystal X-ray diffraction for all the crystals studied.

3.2 Angular resolved magnetic measurements

Angular resolved magnetic measurements with horizontal rotator have been performed on the single crystal samples of Tb, Er and Yb derivatives, described at the beginning of the chapter, following the procedure reported in section 2.3. Thus, after having fixed the crystal, using grease, on the z face of a labeled teflon cube, the x, y and z faces of the cube have been indexed (making use of a single-crystal X - ray diffractometer) assigning to each of them its Miller's indexes h, k, l related to the crystal orthogonalized unit cell (see Table 3.3). The samples have been measured, with the horizontal rotator, rotating along three orthogonal axes corresponding to the normal to the x, y and z faces of the teflon cube.

In Figure 3.5 are shown the experimental data of the three rotations performed at $T = 2$K together with a comparison of single rotations performed at 2K and 10K. The calculated values obtained from Equations 2.16 using the suceptibility tensor elements fitted according to the method described

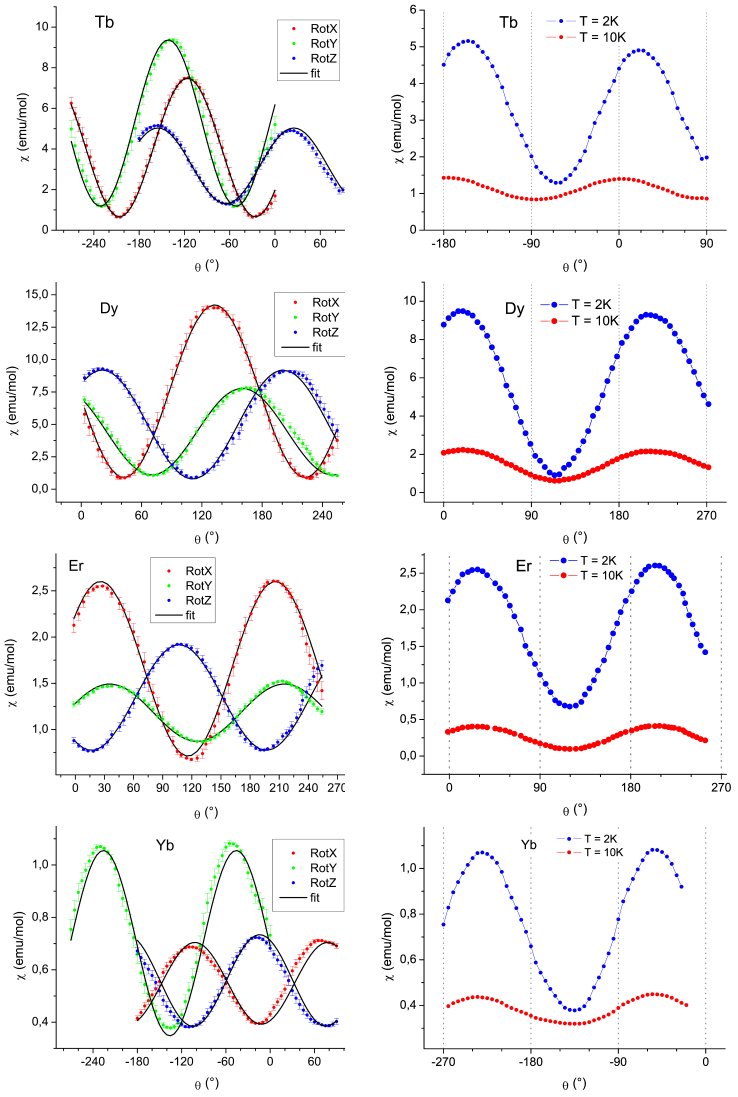

Figure 3.5: On the left: angular dependence of magnetic susceptibility measured at $T = 2$K and $H = 1$kOe for the rotation along the x, y, and z axes of the cube reference frame relating to Tb, Dy, Er and Yb single crystal samples. The solid line represents the calculated values according to Equations (2.16). On the right: comparison of measurements collected at $T = 2$K and $T = 10$K with $H = 1$kOe.

in section 2.3.2 are also reported. The shapes of rotation curves reveal the presence of strong magnetic anisotropy for all compounds. Temperature dependence of angular resolved magnetic measurements shows no appreciable changes in position of maxima and minima for Dy, Er and Yb samples. Between data collected at $T = 2$K and 10K for the Tb sample a shift of about 10° of the position of maxima and minima is instead present. The change of magnetic anisotropy represented by this shift can be addressed, also in this case, to a small energy separation between the ground crystal field level and the first excited ones: heating up the system from 2 K to 10 K implies a depopulation of the lowest levels with a consequent variation of magnetic anisotropy and a related change in angular dependence of the magnetic susceptibility.

The extracted elements of the susceptibility tensor, obtained from the analysis of the angular dependence data, allowed the determination of its principal components according to the diagonalization procedure described in section 2.3.2. Knowing the relative displacement of the x, y, z reference frame in respect to the a, b', c^* one, it was possible to express the components of the susceptibility tensor together with its principal components into the orthogonalized unit cell reference frame (values are summarized in Table 3.4). Results obtained show that all systems have an easy axis of magnetization with strong rhombic anisotropy.

Since all the compounds crystallize in the triclinic group, which means that all the molecules are oriented along the same direction, it has been possible to express the orientation of principal components of $\boldsymbol{\chi}$ with respect to the single molecules. The orientations of the easy axis of magnetization of the molecules measured at $T = 2$K are reported in Figure 3.6 as pink rods together with the angle they form with the the Ln$-$O$_w$ bond (which points to the axial direction of the capped square antiprism described by the first coordination sphere). Results obtained show that for Tb and Dy the displacement of the easy axis of magnetization is almost perpendicular to the molecule axial direction (the angles formed with the Ln$-$O$_w$ direction are respectively 85° and 84° for Tb and Dy); on the contrary Er and Yb compounds present the easy axis of magnetization almost parallel to the Ln$-$O$_w$ bond (6° and 12° respectively). The experimental error of the procedure is evaluated not to exceed 10°. These results compared with

	$\boldsymbol{\chi}$ **elements**	**Pricipal components of** $\boldsymbol{\chi}$
	(emu/mol)	
Tb	$\chi_{aa} = 3.893(18)$ $\chi_{b'b'} = 2.508(3)$ $\chi_{c^*c^*} = 6.116(6)$ $\chi_{ab'} = 1.482(7)$ $\chi_{b'c^*} = 2.2960(16)$ $\chi_{ac^*} = 4.273(11)$	$\chi_1 = 0.493(5)$ $\chi_2 = 1.595(2)$ $\chi_3 = 10.43(2)$
Dy	$\chi_{aa} = 7.221(25)$ $\chi_{b'b'} = 2.131(19)$ $\chi_{c^*c^*} = 7.625(25)$ $\chi_{ab'} = -2.934(25)$ $\chi_{b'c^*} = -2.567(25)$ $\chi_{ac^*} = 6.554(19)$	$\chi_1 = 0.601(17)$ $\chi_2 = 1.227(25)$ $\chi_3 = 15.145(25)$
Er	$\chi_{aa} = 3.9571(22)$ $\chi_{b'b'} = 1.514(5)$ $\chi_{c^*c^*} = 2.669(8)$ $\chi_{ab'} = 0.094(5)$ $\chi_{b'c^*} = 0.234(14)$ $\chi_{ac^*} = -1.768(3)$	$\chi_1 = 1.223(23)$ $\chi_2 = 1.721(8)$ $\chi_3 = 3.1955(12)$
Yb	$\chi_{aa} = 0.9009(4)$ $\chi_{b'b'} = 0.3788(14)$ $\chi_{c^*c^*} = 0.5292(14)$ $\chi_{ab'} = 0.1667(8)$ $\chi_{b'c^*} = -0.1099(16)$ $\chi_{ac^*} = -0.3255(5)$	$\chi_1 = 0.345(3)$ $\chi_2 = 0.3928(10)$ $\chi_3 = 1.0715(10)$

Table 3.4: Magnetic susceptibility tensor elements in the orthogonalized unit cell reference frame and principal components of $\boldsymbol{\chi}$ obtained from fitting procedure described in section 2.3.

Figure 3.6: Experimental (pink) and calculated (blue) magnetization easy axis at $T = 2$K for the series viewed perpendicular (top) and parallel (bottom) to the pseudo four-fold symmetry axis of the molecules together with a representation of the $4f$ electron density distribution relative to the Ln^{III} ions. The reported angles are those formed by the easy axes and the Ln$-$O$_w$ direction.

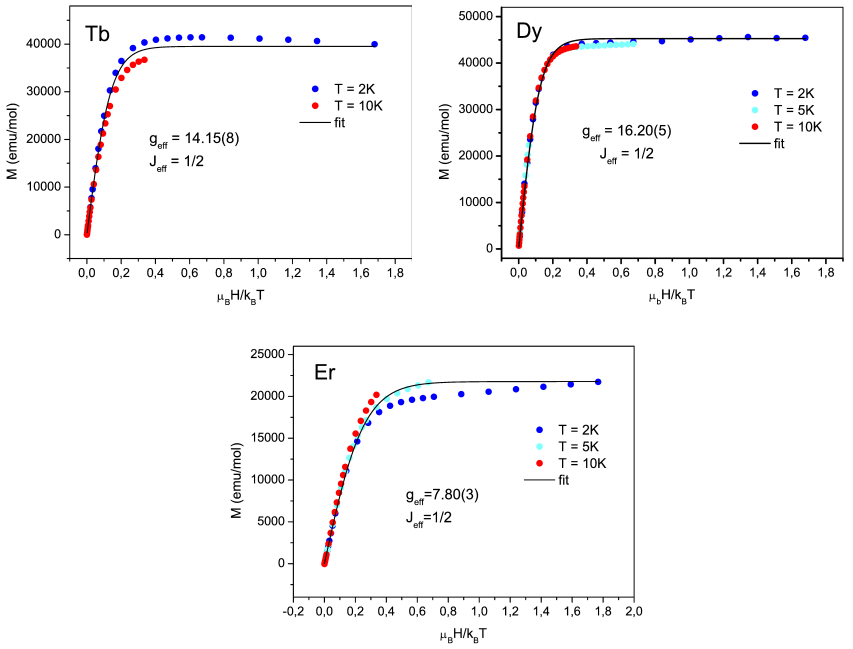

Figure 3.7: Magnetization dependence on reduced variable $\mu_B H/k_B T$ for Tb, Dy and Er single crystals oriented so that their easy axis of magnetization were aligned to the applied magnetic field. Measurements have been performed at different temperatures as specified by the color scale.

the density distribution of the $4f$ electrons (the ones involved in magnetic properties of the rare-earth elements) reveal the importance of interactions between the charge distribution of lanthanide ion and the ligand one that for the DOTA can be thought like a sandwich type consisting of the four carboxylate groups and four nitrogen atoms surrounding the central ion.

Once the direction of easy axis of magnetization was determined, Tb and Er single crystals (whose magnetic signal was strong enough) were opportunely oriented in order to measure the magnetization along the easy axis direction. The field dependence of the magnetization at different temperatures is reported in Figure 3.7 together with the Dy one. Data were fitted with the Brillouin function (1.13) assuming only the ground doublet

populated and describing the system with a g_{eff} and $J_{\text{eff}} = \frac{1}{2}$. For Dy sample data collected at $2, 5, 10$K in function of reduced variable $\mu_B H/k_B T$ are well superimposable and as result the fit returned a value $g_{\text{eff}} = 16.20(5)$. On the contrary, measurements on Tb and Er derivatives revealed a nonperfect superposition when plotted versus the reduced variable $\mu_B H/k_B T$ (again ascribable to small energy separation of ground multiplet from excited ones). Anyhow, the analysis with the Brillouin function considering $J_{\text{eff}} = 1/2$ provided a best fit for $g_{\text{eff}} = 14.2$ and 7.8 for Tb and Er, respectively.

3.3 Comparison with theoretical *ab initio* model

Magnetic properties of the entire series studied have also been investigated by *ab initio* calculations which consist of the numerical solution of the Hamiltonian of the system. This part of the work was conducted in collaboration with Dr. Javier Luzon from Centro Universitario de la Defensa and Instituto de Ciencia de Materiales in Zaragoza (Spain) and not by me personally. The results obtained are here presented for comparison with experimental data given also the importance assumed by the *ab initio* model in describing energetic configurations of molecules.

The method followed is based on the CASSCF/CASPT2-RASSI-SO approach as implemented in the MOLCAS 7.4 code[40] developed by Lund University. This method is particularly advantageous when dealing with systems presenting molecular ground states which are quasi-degenerate with low lying excited states (a situation where Hartree and DFT method are not adequate) and have been demonstrated to be a precious tool to rationalize the magnetic behavior of lanthanide-based molecular clusters and chains.[41–48]

As the starting point a Complete Active Space Self Consitent Field (CASSCF) calculation which determines the Configuration State Functions (CSF) is considered. The latter consists of a combination of Slater determinants which, given N valence electrons in M orbitals, considers all the combinations in order to present a given total spin of the system. At this step, neither electron correlations nor spin-orbit coupling are still not taken into account but the CSF determined by the CASSCF method serves as

	g_1	g_2	g_3
Tb	0.5	2.1	12.7
Dy	0.005	0.04	19.5
Ho	1.3	3.3	6.2
Er	1.8	2.8	10.9
Tm	0.95	1.02	12.02
Yb	0.1	1.0	6.8

(a)

Ground-state multiplet energy levels (cm^{-1})						
Tb	0	1.6	25.4	29.8	115.6	144.0
(singlets)	159.9	213.7	245.9	314.4	323.9	379.9
	384.4					
Dy	0	74.9	117.3	178.3	247.5	297.0
(doublets)	348.5	430.3				
Ho	0	4.8	29.9	44.1	87.5	145.8
(singlets)	155.6	172.2	185.5	192.9	214.0	227.5
	253.6	273.4	290.5	303.8	309.2	
Er	0	19.8	63.2	77.1	163.2	228.8
(doublets)	317.5	427.0				
Tm	0	4.6	99.0	105.3	143.0	173.0
(singlets)	206.6	225.5	260.6	307.5	325.5	384.2
	384.7					
Yb	0	197.2	379.3	416.2		
(doublets)						

(b)

Table 3.5: Gyromagnetic factors along the main anisotropy axes considering $J_{\text{eff}} = 1/2$ (a) and energy level structure of the ground $^{2S+1}L_J$ multiplet from the *ab initio* calculations (b).

a basis set on which to consider further interactions. This is done by the CASPT2 method for calculating the dynamic electron correlation and after applying the RASSI-SO method for spin-orbit coupling.

The cluster model employed in the model consists of LnDOTA(H_2O), the three neighbor Na^+ ions and $H_3C{-}CO_2$ molecules replacing the molecular fragments $-NCH_2{-}CO_2$ from neighbor DOTA molecules. In addition, 4 Na^+ ions in the position of the Ln ions close to the previous $-NCH_2{-}CO_2$ molecular fragments were added to the molecular cluster in order to correctly account for both the short-range electrostatic interaction of LnDOTA(H_2O) molecule with the neighbor ions and molecules and the Madelung potential, due to the long range electrostatic interactions, produced by the rest of the crystal in the region of the LnDOTA(H_2O) molecule.

The calculations allowed to obtain the energies of the lowest multiplet-levels together with the determination of the **g** tensor and its principal components. Results obtained are reported in Table 3.5 while in Figure 3.6 the easy axis of magnetization directions calculated for the molecules are drawn as blue rods.

In Figure 3.6 is evident a gradual rotation of the easy axis from orthogonal towards parallel to the Ln$-O_w$ bond (see the angle values in blue) on increasing the number of $4f$ electrons. Moreover the agreement between calculated and observed anisotropy is good except for Er, for which the easy axis is calculated in an intermediate position while experimentally it lies along the Ln$-$Ow bond. This is ascribable to the fact that Er is the only derivative showing, in the *ab initio* calculations, a large influence of the dynamic electronic correlation correction (CASPT2).[49] This fact makes the accurate determination of the direction of the easy anisotropy axis more complex.

As far as Tb is concerned, the separation between the first excited state and the ground state resulted being $1.6\,cm^{-1}$, which could justify the change in the magnetic anisotropy on increasing the temperature from 2 K to 10 K.[50]

3.4 Luminescence measurements

Several rare-earth ions and particularly Tb are characterized by intense fluorescence.[51] Moreover complexes with DOTA ligand present good emis-

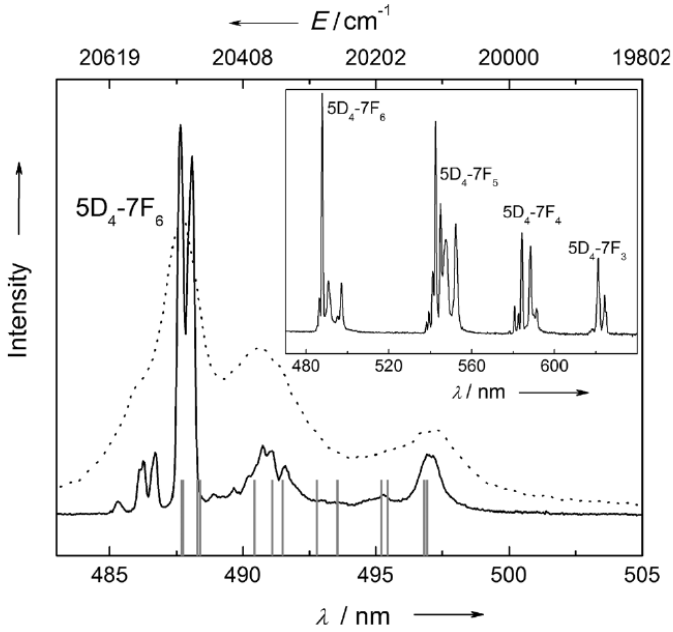

Figure 3.8: Luminescence spectrum in the region involving the ${}^5D_4 \rightarrow {}^7F_6$ transition of a polycrystalline powder sample of Tb excited at 380nm at room temperature (dotted line) and at 77K (solid line). The calculated energy levels of the ${}^7F_6$ multiplet are represented by gray bars. Inset: full emission spectra in the 450 nm to 680 nm range.

sion efficiency.[34] For these reasons to further check the validity of *ab initio* calculations luminescence experiments have been performed on a polycrystalline sample of TbDOTA. Since the laboratory at LA.M.M., where this thesis work has been conducted, are not equipped for luminescence characterization the sample has been sent to INSA laboratory of Rennes where luminescence measurements have been performed.

The experimental set-up used consists of a Fluorolog III spectrofluorimeter by Horiba-JobinYvon equipped with a F-3018 integrating sphere whose task is collect the emitted photons, independently from their emission direction, and collect them to the input of a photomultiplier. The operating temperature range spans from room temperature to 77K thanks to a dedicated N_2 optical dewar. The excitation is instead provided by a

Xe lamp.
The wavelength $\lambda = 380$nm has been chosen for excitation being the wavelength at which the excitation spectra collected showed the maximum of intensity and luminescence spectra were recorded at room temperature and at 77K.

Spectra obtained showed well resolved multiline emissions attributed to $^5D_4 \rightarrow {}^7F_6$ ($20\,500\,\mathrm{cm}^{-1}$), $^5D_4 \rightarrow {}^7F_5$ ($18\,500\,\mathrm{cm}^{-1}$), $^5D_4 \rightarrow {}^7F_4$ ($17\,000\,\mathrm{cm}^{-1}$) and $^5D_4 \rightarrow {}^7F_3$ ($16000\mathrm{cm}^{-1}$) transitions (see inset in Figure 3.8). Focusing on transitions involving the ground multiplet $^7F_6$ (shown in Figure 3.8) it reveals a structured profile. Temperature dependence of the spectra suggests that the intense peak at $20530\mathrm{cm}^{-1}$ indicates the transition involving the ground level and the lowest level of excited multiplet $^5D_4$, while all the features present at higher energies are hot transitions, that is, coming from excited levels of the $^5D_4$ multiplet. Comparing the spectrum with the calculated energy levels from *ab initio* calculation (represented as gray bars in Figure 3.8) the overall separation of the $^7F_6$ manifold results well reproduced.

3.5 AC susceptibility measurements

Given the easy axis anisotropy of the entire series, magnetization dynamics has been measured by AC susceptometry. Values of χ' and χ'' have been measured at fixed temperatures and in different static magnetic fields for all the samples as a function of the frequency of the AC field. In static zero field all compounds did not reveal a significant out of phase component of the susceptibility. The samples showed a different behavior when a static magnetic field was applied: while Tb, Ho, and Tm continue to present no appreciable χ'' values (see Figure 3.9) Er and Yb presented well-resolved maxima after the application of the field. The profiles of χ' and χ'' for Er and Yb derivatives are shown in Figure 3.10 together with the Dy ones for comparison. In particular Dy presents a non-zero χ'' also in the absence of a static magnetic field which is considered as a fingerprint of a SMM behavior. The rise of imaginary components of χ at high frequency is instead due to the presence of a second relaxation process.[35,36]

The frequency dependence of the ac susceptibility of Er and Yb, measured under the application of a static field of 1kOe has been collected at

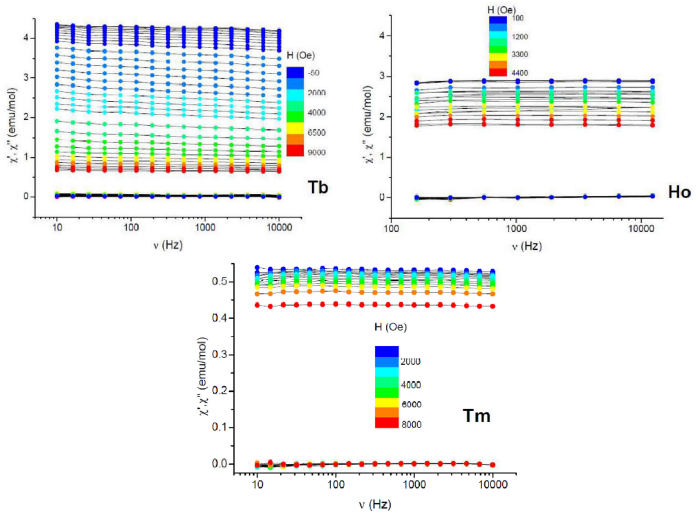

Figure 3.9: Frequency dependence of the real and imaginary components of the magnetic susceptibility of Tb ($T = 2$K), Ho ($T = 2$K) and Tm ($T = 2$K), in different applied static magnetic fields (see color scale in inset).

different temperatures (see Figure 3.11 where are also shown the measurements on Dy derivative measured in a static field of 900Oe) and analyzed using the Cole-Cole formula (2.11). The extracted relaxation times are plotted as a function of the inverse of temperature in a semi-logarithmic plot in Figure 3.12. Both Er and Yb derivatives exhibit an exponential increase of τ on decreasing temperature for the higher investigated temperatures, followed by a gradual leveling of the relaxation time on approaching the lowest investigated temperature. Data following the exponential behavior at higher temperatures have been analyzed with the Arrhenius law $\tau = \tau_0 e^{\Delta/k_B T}$ and the extracted values for the parameters are $\Delta = 39(2)\,\mathrm{K}$ and $\tau_0 = 2.5(8) \times 10^{-8}\,\mathrm{s}$ for Er and $\Delta = 29(2)\,\mathrm{K}$ and $\tau_0 = 4(1) \times 10^{-7}\,\mathrm{s}$ for Yb. Given that the exponential behavior is present only in a small temperature range, to get a better estimation the data were reproduced assuming that the relaxation rate is given by an Arrhenius-like contribution, dominating at high temperature, plus an alternative mechanism, the efficiency of which is considered dependent on T^n. The best fit curves in Figure 3.12 were obtained with $\Delta = 49(1)\,\mathrm{K}$ and $35(2)\,\mathrm{K}$ with $n = 2.5(1)$

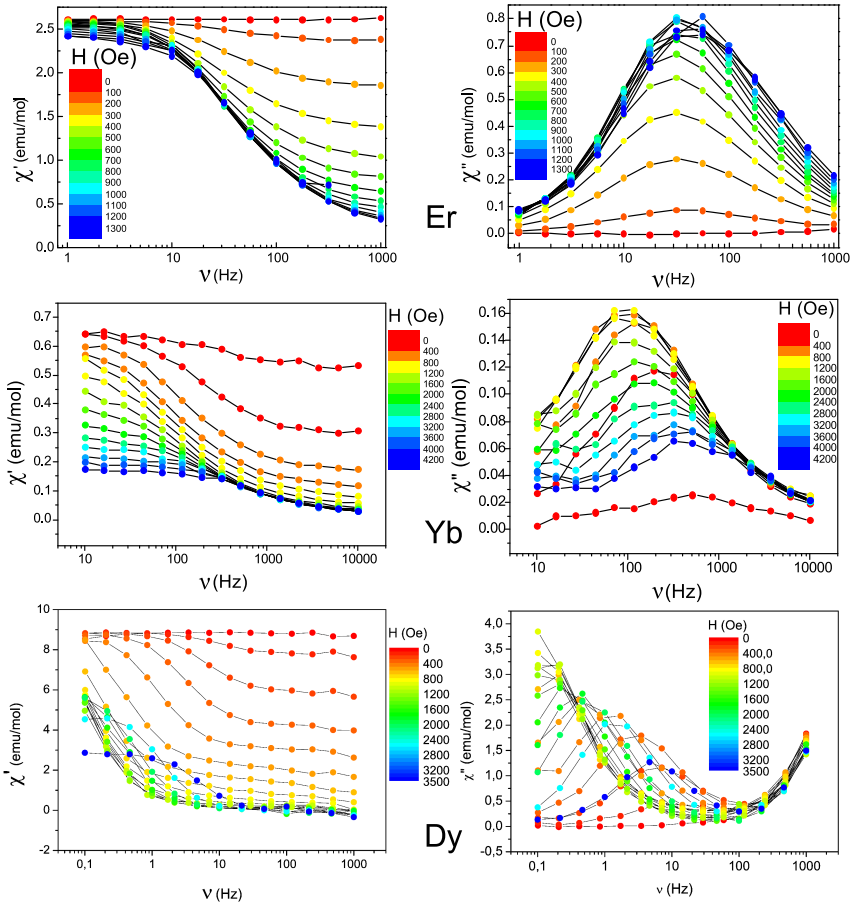

Figure 3.10: Frequency dependence of the real and imaginary components of the magnetic susceptibility of Er ($T = 1.8$K), Yb ($T = 1.8$K) and Dy ($T = 1.9$K), in different applied static magnetic fields (see color scale in inset).

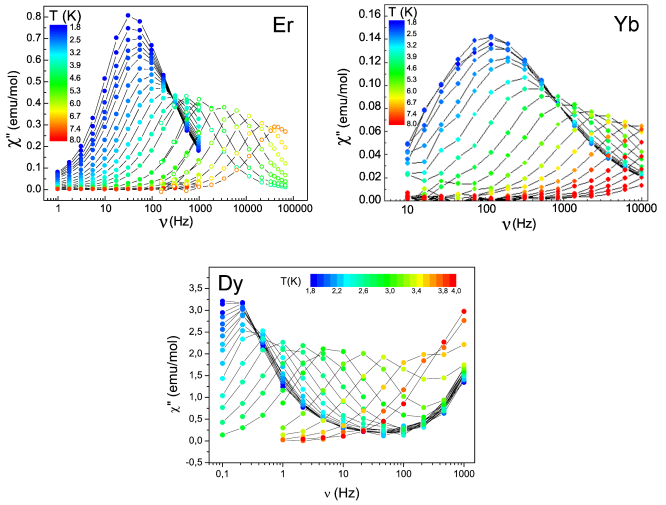

Figure 3.11: Frequency dependence of the imaginary components of the magnetic susceptibility of Er (H = 1kOe), Yb (H = 1kOe) and Dy (H = 900Oe), at different temperatures (see color scale in inset).

and 1.2(1) for Er and Yb, respectively.

The field-induced slow magnetization dynamics of the Er^{III} and Yb^{III} derivatives is quite common among lanthanide complexes. What is more striking here is the absence of any slow dynamics in the other three derivatives. In fact, despite the different shape of the distribution of the electron density, all derivatives present an easy axis of magnetic anisotropy and thus experience a barrier for the reversal of the magnetization. But while for Dy^{III}, Er^{III} and Yb^{III}, whose ground J value is half-integer, Kramers theorem assures a double-degenerate ground state the same is not true for Tb^{III}, Ho^{III} and Tm^{III}. Double-degenerate ground states for integer J would requires infact a pure axial anisotropy but the presence of transverse anisotropy terms (see Table 3.4) reveals that this is not our case. As a consequence the ground multiplet is split by transverse anisotropy in non-degenerate states and states on opposite sides of the barrier are strongly admixed favoring tunnel relaxation processes. The oscillatory behavior observed along the series can thus be ascribed to the number of 4f electrons.

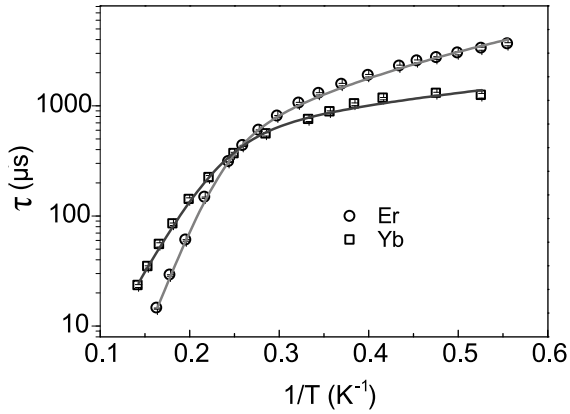

Figure 3.12: Dependence of the relaxation time τ on inverse of temperature T for Er and Yb derivatives in static field 1000Oe. The solid lines correspond to the best fit assuming a combination of exponential and power law dependence on T of the relaxation rate.

Spin parity effects on the tunneling efficiency have been observed in polynuclear 3d clusters[52] and in an isostructural series of single-ion SMMs.[53] On the other hand, in series of bis-phthalocyaninate complexes, where indeed is present a greater axial symmetry, the Tb^{III} and Dy^{III} derivatives show a similar behavior, although with different activation energy.[4]

In a work of 2011, Rinehart and Long[20] proposed a qualitative method to determine the magnetic anisotropy of a SMM based on the correlation between prolate/oblate distribution of electron density and ligand geometry. In particular for the $DOTA^{4-}$ ligand, whose negative charges lie very close to the equatorial plane of the complex (Ln ion is only at 0.72 Å from the plane formed by the oxygen donor atoms), this model predicts an easy axis anisotropy along the axial direction in the case of prolate ions (such as Er^{III} and Yb^{III}) while for oblate ions (like Tb^{III}, Dy^{III} and to a lesser extent Ho^{III}) the axial direction should be a hard one and the equatorial plane should correspond to an easy plane of magnetization without any barrier for the reversal of the magnetization.

Results obtained from the study on LnDOTA series partially confirmed this model which worked only for ErDOTA and YbDOTA but failed to

predict the magnetic behavior of TbDOTA, DyDOTA and HoDOTA. What found reveals that easy axis anisotropy is ubiquitous in the late lanthanide series of DOTA complexes but this feature is far from being a sufficient condition to observe slow magnetization dynamics. The uniaxial magnetic anisotropy is, in fact, not correlated with the pseudo-symmetry of the first coordination sphere. In such a situation transverse components of the crystal field play a crucial role and promote efficient under-barrier mechanisms of relaxation, in particular for integer spin states.

4 The Cp*ErCOT SMM

Angular resolved magnetic measurements performed with the horizontal rotator have demonstrated to be a valid tool to study magnetic anisotropy and, in particular, for compounds which crystallize in the triclinic system, such as the LnDOTA, allows the determination of magnetic anisotropy of the single molecule. Triclinic crystals, however, represent less than one third of the reported lanthanide complexes. In general magnetic measurements performed with the horizontal rotator provide the sum of all molecular contributions which, except in the triclinic case, are not oriented along the same directions. As a consequence, apart from the magnetic anisotropy of the sample as a whole, not much information regarding the anisotropy of the single molecule can be deduced without the support of other measurements. This is the situation encountered in studying the SMM Cp*ErCOT in the single crystal form, where, as will be shown, accompanying the horizontal rotator measurements with the study of dynamics of magnetization we were able to extrapolate important information concerning the molecular magnetic anisotropy notwithstanding the system crystallizing in the orthorhombic system.

Cp*ErCOT indicates an organometallic complex in which Cp* is the pentamethylcyclopentadiene anion ($C_5Me_5^-$) and COT is the cyclooctatetraene dianion ($C_8H_8^{2-}$). Cp*ErCOT is of great appeal for fundamental studies on hybrid nanostructures that are of interest for molecular spintronics because it is soluble in most organic solvents and can be evaporated in an inert atmosphere or under high vacuum. A first evidence of its SMM behavior was reported in a work of 2011 conducted on microcrystalline samples by Jiang et al.[54] where DC and AC magnetic measurements revealed the presence of two thermally activated magnetic relaxation processes with

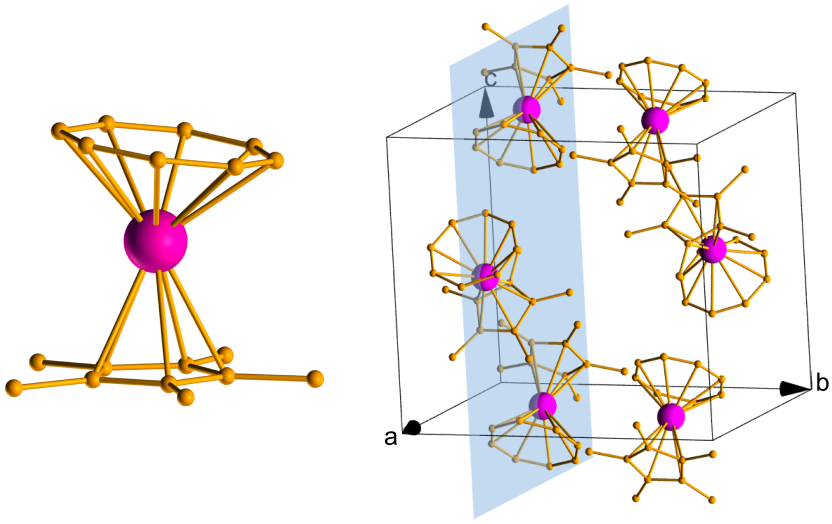

Figure 4.1: Structure of the Cp*ErCOT molecule (on the left) and its molecule packing in the unit cell (on the right). In pale blue is shown the mirror plane. Carbon atoms are represented in orange while in pink are represented the erbium atoms. Hydrogen atoms are not depicted for clarity.

energy barrier equal to 197K and 323K, respectively, together with the opening of a butterfly shaped magnetic hysteresis below 5K. The presence of two thermally activated magnetic relaxation processes was attributed by the authors to the presence of two stable conformers with different COT conformations in the crystal. The complex crystallizes in the orthorhombic space group Pnma with two families of almost perpendicular molecules related by a binary axis parallel to b and characterized by the presence of a mirror plane parallel to the ac plane (see Figure 4.1).

The choice of two aromatic rings sandwiching a rare-earth ion to construct a SMM was dictated by the intent of obtaining a higher local uniaxial symmetry due to the delocalized π electrons which can be approximated into a ring of the electron cloud. Notwithstanding this the two aromatic rings are tilted by 8°, so it is not possible to geometrically define a molecular axis. The presence of this bending angle destroys the local axial symmetry and the consequent presence of transverse anisotropy is one of the causes of the observed tunneling relaxation processes.[54,55]

4.1 Angular resolved magnetic measurements with horizontal rotator

The angular dependence of the susceptibility was measured with the horizontal rotator following the procedure described in chapter 2.3. As Cp*ErCOT is only stable under an inert atmosphere a great attention was paid during the manipulation of the sample to avoid exposure to air. The entire sample preparation was carried out in a glovebox where, in order to isolate the crystal from atmosphere, the crystal was embedded in Apiezon N grease on the face of a millimetric teflon cube. After that, the crystal and the cube's faces were subjected to the indexing procedure under nitrogen gas flux. The installation on the horizontal rotator was also carried out under nitrogen flux.

In the procedure of angular resolved magnetic measurements with horizontal rotator described in chapter 2.3 and applied in the measurements on LnDOTA, three orthogonal rotations were performed. For the Cp*ErCOT complex, given the presence of the symmetry plane only two rotations are relevant.

Following the symmetry showed by the system we tried to perform two rotations: one parallel to the b crystallographic axis and the other orthogonal to it. The strong sensitivity of the compound to air did not allow us to take the time to perfectly align the crystal to perform rotations along the crystallographic axes and the rotation named hereafter **Rot1** was performed along a vector ω_1 nearly perpendicular to b, while **Rot2** was performed by rotating along a vector ω_2 almost collinear to b. In Figure 4.2 are reported the planes spanned by **Rot1** and **Rot2** in the unit cell reference.

The magnetic moment measured by rotating the crystal in the magnetic field is the the sum of two different contributions that come from the two families of symmetry-related but magnetically non-equivalent molecules. In Figure 4.3 a is reported the angular dependence of the magnetic susceptibility at $T = 10$K with a static magnetic field $H = 1$kOe for the two rotations. The **Rot1** data provide evidence that the system possesses a large magnetic anisotropy. By projecting the anisotropy of the magnetic susceptibility on the crystal structure (Figure 4.3 b), it is possible to notice

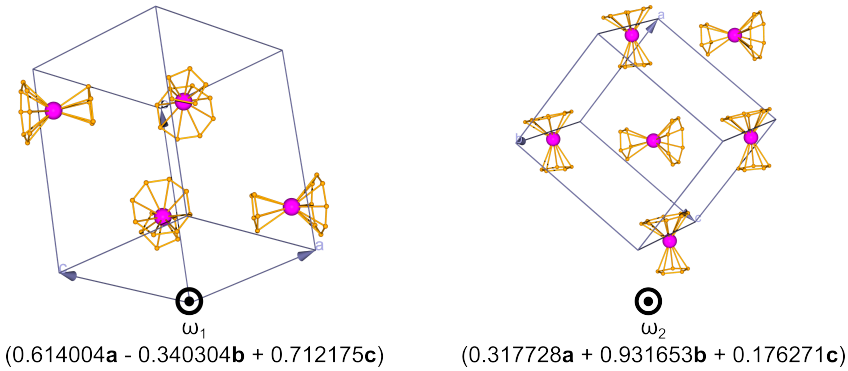

Figure 4.2: Views of the planes spanned by **Rot1** and **Rot2** along the rotation axis, ω_1 and ω_2, directions whose definition in terms of direction cosines in the cell frame is reported.

that the minimum of the susceptibility is observed when the magnetic field is applied in the equatorial plane (i.e. the plane of the cyclic ligands) of both families of symmetry-related molecules. The maximum instead corresponds to the case in which the magnetic field is approximately along the pseudosymmetry axis of only one family and perpendicular to the other. So the first information that is possible to extract from this rotation is that at least one direction in the equatorial plane of the sandwich structure is a hard axis of magnetization.

Rot2 shows a completely different behavior given that the susceptibility presents much less anisotropy. During this rotation the applied magnetic field roughly scans the *ac* plane, which corresponds to the symmetry plane of both families of molecules (Figure 4.3 c). This means that two principal directions of each molecular anisotropy tensor were therefore probed in the rotation and, given the different orientation of the two molecular families, the fact the magnetic susceptibility tensors of the two families are related by a glide plane orthogonal to c has to be taken into account.

In analyzing the lack of strong anisotropy in **Rot2** two limiting cases can be considered: the first one corresponds to a situation in which the molecules possess an easy-plane anisotropy in the *ac* plane and the small anisotropy observed is due to the non perfect alignment of ω_2 with b axis. In the second case the molecules would possess an ideal easy-axis magnetic

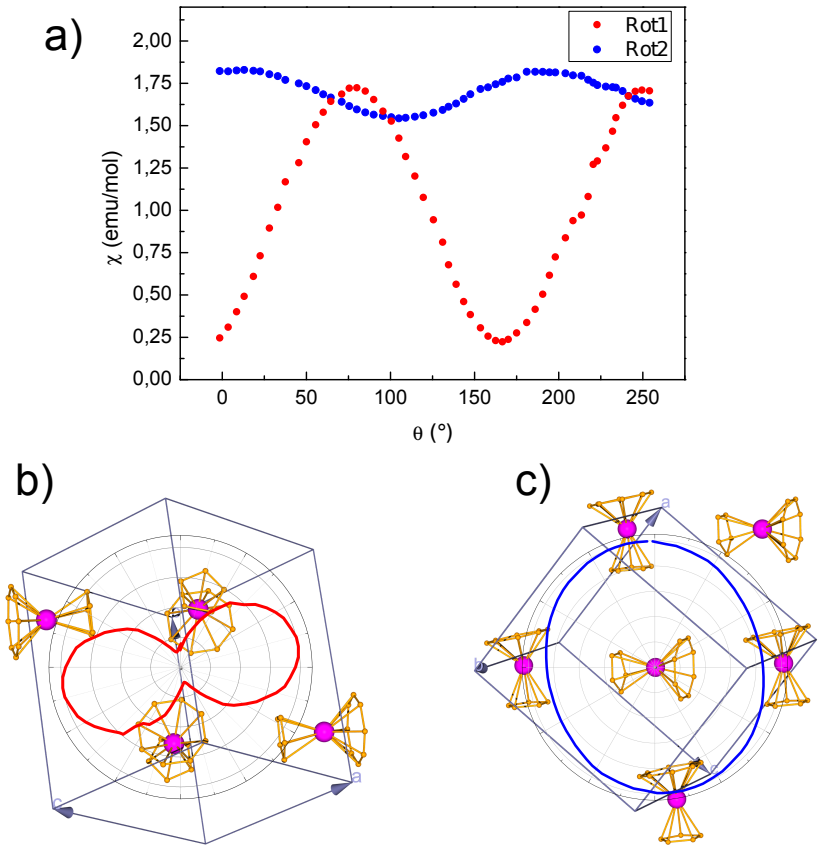

Figure 4.3: a) Angular dependence of the magnetic susceptibility at 10K and 1kOe static field for the rotations **Rot1** (red dots) and **Rot2** (blue dots). b) Polar plot of the measured magnetic susceptibility superimposed over the crystal packing for **Rot1**. c) Polar plot of the measured magnetic susceptibility superimposed over the crystal packing for **Rot2**. Me groups on the Cp* rings are omitted for clarity.

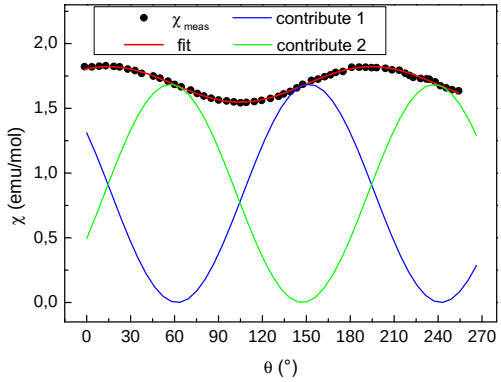

Figure 4.4: Result of the fit (red line) of **Rot2** data collected at $T = 10$K and $H = 1$kOe using Equation (4.1). Blue and green lines represent the single contributions coming from the two molecular families. Fitting procedure returned the parameter values $\chi_{\text{Is}} = 1.69(1)$ emu/mol and $\phi = 94.65(5)°$.

anisotropy and the measured magnetic susceptibility is the result of the sum of two Ising contributions coming from the two molecular families. This situation is described by

$$\chi_{\text{meas}} = \chi_{\text{Is}}[\cos^2(\theta_1) + \cos^2(\theta_2)] = \chi_{\text{Is}}[\cos^2(\theta_1) + \cos^2(\theta_1 + \phi)] \qquad (4.1)$$

where χ_{Is} describe the Ising-type susceptibility of the molecules, θ_1 and θ_2 the angles formed by the applied magnetic field with the two molecular families and ϕ the angle between their easy-axis direction. In particular if the two families were exactly orthogonal to each-other $\cos^2(\theta_1) + \cos^2(\theta_1 + \pi/2) = \cos^2(\theta_1) + \sin^2(\theta_1) = 1$ and $\chi_{\text{meas}} = \chi_{\text{Is}}$ showing an isotropic behavior. The small anisotropy observed would be in this case the result of a tilting angle between the two families near but not exactly equal to 90°. In Figure 4.4 the result of the best fit of **Rot2** data using Equation (4.1) is shown. The value $\phi = 94.65(5)°$ obtained from the fit is consistent with the crystallographic data of the samples where, considering the axis connecting the centroids of the aromatic rings, the angle found is 95.4°.

Even if the latter hypothesis is the most consistent with the quasi-axial symmetry of the complex and its magnetic bistability, any intermediate

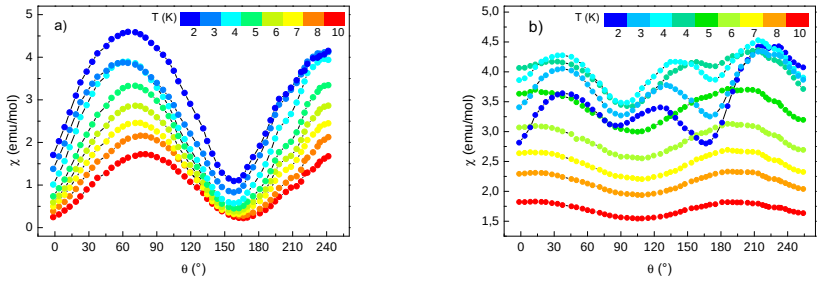

Figure 4.5: Angular dependence of magnetic susceptibility at different temperatures in the range $2 - 10$K for **Rot1** (a) and **Rot2** (b).

situations between the two limiting cases illustrated above could provide a consistent description to the observed behavior.

4.2 Study of dynamics of magnetization

The only sure information obtained thus far from magnetic measurements with the horizontal rotator comes from **Rot1** and it is that at least one direction in the equatorial plane of the molecule is a hard axis of magnetization.

To obtain information independently from any *a priori* assumption, measurements at lower temperatures were carried out. Whereas the angular dependence of the magnetization does not exhibit any particular feature by cooling the temperature in **Rot1** (Figure 4.5 a), **Rot2** measurements reveal the appearance of a third maximum below 5K (Figure 4.5 b).

As already shown by Gao and co-workers,[54,55] below 5K the opening of the magnetization hysteresis loops occurs in Cp*ErCOT, which indeed coincides with the temperature range where the presence of the third peak is observed in **Rot2**. Looking for a correlation between the opening of hysteresis loops and the appearance of the third maximum, the hysteresis curves were measured at 5, 4 and 2K orienting the sample at the angular position that corresponds to the maxima of susceptibility in order to record as much signal as possible. Opening of the hysteresis below 5K was observed for all the three investigated angular positions. The cycles

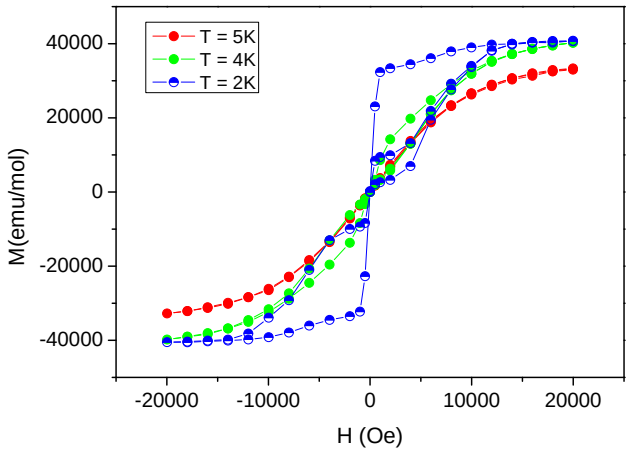

Figure 4.6: Hysteresis loop measured at $T = 5$, 4 and 2K in correspondence of the maxima in measurements with the horizontal rotator, respectively at $\theta = 8.5$, 33 and 37.5°.

showed a butterfly shape, which is a signature of the presence of efficient zero-field quantum tunnelling. In Figure 4.6 are reported data referring to the first maximum for the three temperatures investigated ($T = 5$, 4 and 2K) measured respectively at $\theta = 8.5$, 33 and 37.5°.

These measurements seem to correlate the appearance of the third maximum in the angular dependence of the susceptibility with the opening of the hysteresis cycle. During the rotations the magnetic field was kept constant at $H = 1$kOe so only its projection along the molecular axis varied. The presence of a hysteresis-related behavior excludes the hypothesis that the *ac* plane is an easy-plane of magnetization since in this situation every direction of the magnetic field would be equivalent being the plane magnetically isotropic. The only explanation to the correlation observed between opening of the hysteretic cycles and angular dependence of the magnetic susceptibility is the presence of a molecular magnetic easy-axis in the probed crystallographic plane. During rotation the projection of the magnetic field along the easy-axis changes, which is equivalent to keeping the molecule still and varying the field. When measuring below 5K if the

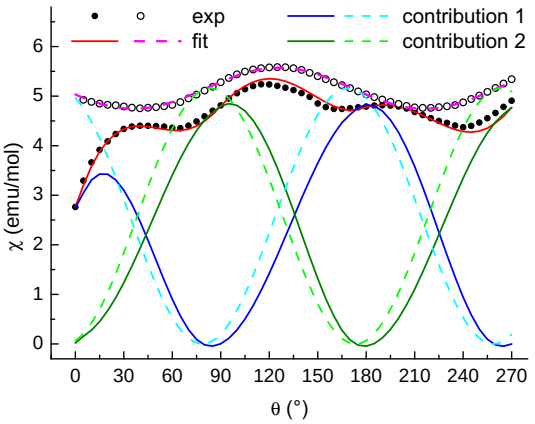

Figure 4.7: Fit (red and pink lines) of the experimental angular dependence of the magnetic susceptibility measured with short (•) and long (○) time delays. The two deconvoluted contributions are shown in blue and green as dashed and solid curves for equilibrium and out of equilibrium, respectively.

field is changed too fast (i.e. the rotation is too fast), being in a slow relaxation regime, the magnetization of each molecule does not reach the equilibrium instantaneously but tends to remain blocked, decaying too slowly to the equilibrium value compared to the characteristic time of the experiment. As a consequence the susceptibility of the crystal deviates from the $\cos^2(\theta)$ behavior and averaging of the contributions of the two families of symmetry-related molecules, which characterizes the smooth behavior at $T = 10$K, is therefore lost in the hysteretic regime.

To confirm this hypothesis a third rotation, **Rot3**, scanning *ac* plane was repeated on a new crystal (this time the rotation axis $\omega_3 = 0.001728\mathbf{a} + 0.999571\mathbf{b} - 0.029253\mathbf{c}$ deviated from the b axis by only 2°) performing measurements with two different timescales. The first consisted in applying between two successive angular positions the shortest delay allowed by our experimental setup (≈ 50s) to measure the system as far as possible from equilibrium. In the second case a delay equal to 2300s was introduced between each step of the rotation and the data acquisition to let the

system relax to equilibrium. The results obtained at $T = 4$K (Figure 4.7) fully support this conjecture. The measurements performed with the long delay (empty circles in Figure 4.7) do not show the three-peak profile that characterizes the system out of equilibrium (black dots) but present a behavior similar to the one obtained above 5K, when hysteresis effects are not present.

Data collected with a long delay were therefore fitted using Equation (4.1) (pink line in Figure 4.7) by summing up the two square cosine functions (dashed green and cyan lines) of two easy-axis magnetic centres obtaining an amplitude of $\chi_{Is} = 5.160(4)$ emu/mol and a separation between the easy-axis equal to 94.60(6)°. The so determined contribution at the equilibrium has been used as starting point to simulate the out-of-equilibrium data obtained with the shortest delay assuming an exponential decay. The behavior of the magnetization $M(\theta, t)$ at angle θ with magnetic field and time t, was fitted point-by-point by using the exponential relation:

$$M(\theta, i) = M_{\text{eq}}(\theta, i) + \Delta M_i e^{-\frac{\sigma_i}{\tau(H)}} \tag{4.2}$$

in which M_{eq} is the value of magnetization at equilibrium (obtained for each θ from the long-delay measurements), σ_i is the time elapsed between i - th measurement and the subsequent (i+1)-th during which the system tends toward equilibrium (assuming that the time of the rotations between two positions is negligible); ΔM_i is the measure of how far from equilibrium the system is at every change of field and $\tau(H)$ is the relaxation time. A better agreement was obtained by assuming that $\tau(H)$ depends on the variation of the magnetic field according to an increase or decrease through a linear relationship composed of a magnetic-field-independent component (tau_0) and by a term linearly dependent on the projection of H along the easy axis according to:

$$\tau = \tau_0 + AH\cos(\theta) \tag{4.3}$$

The difference between increasing and decreasing field situations is expressed through the A constant, which in the best-fit simulation assumes two values: $A_{\text{inc}} = 0.210(5)$ s/Oe and $A_{\text{dec}} = 0.140(5)$ s/Oe, for increasing and decreasing field projection, respectively, whereas $\tau_0 = 105(5)$ s. The result is shown in Figure 4.7 as a red line representing the sum of the two out-of-equilibrium contributions (solid cyan and green lines) obtained with the

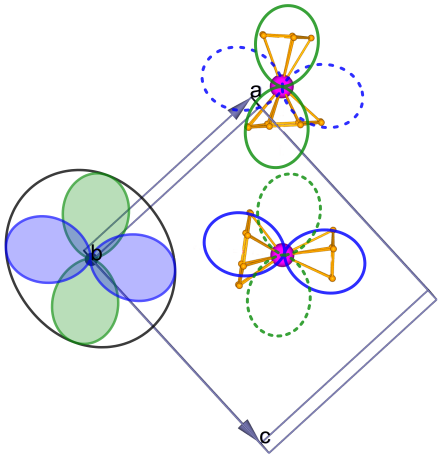

Figure 4.8: Polar plot of the two contributions (same color code as above) and of their sum (black line) superimposed over the crystal cell content view along ω_3 direction. Projected over the molecules are also reported the two possible molecular anisotropies characterized by the easy-axis directed along the pseudo-symmetry molecular axis (solid lines) or orthogonal to them (dashed lines).

best-fit parameters mentioned above. Positive A values reflect the slowing down of the magnetic relaxation when a weak magnetic field is applied due to suppression of the tunnel mechanism. Different values observed upon decreasing or increasing the longitudinal component of the magnetic field during the rotation is not unexpected, since the initial magnetization state of the material affects also the tunneling mechanism by modifying the local magnetic field.[56–58]

Analysis of angular dependence of magnetic susceptibility together with the study of dynamics of the magnetization allowed to deconvolute the contributions of each family of strongly anisotropic molecules starting from a quasi-isotropic behavior of the crystal at thermodynamic equilibrium. It was shown indeed that a reasonable simulation of the out-of-equilibrium anisotropy can only be achieved if two almost orthogonal Ising-like contributions are present, but it is not possible to associate unambiguously each contribution to one particular family of symmetry-related molecules. As illustrated in Figure 4.8 results obtained allowed to determine the two

	Experimental structure at 120K		DFT-optimized structure	
	Conformer 1	Conformer 2	Conformer 1	Conformer 2
g_x	0.00062	0.00057	0.00000	0.00002
g_y	0.00086	0.00085	0.00005	0.00002
g_z	17.947	17.939	17.945	17.944
$\Delta E(\mathrm{cm}^{-1})$	84.8	115.9	134.9	135.2

Table 4.1: Principal components of $\mathbf{g}_{\mathrm{eff}}$ tensor of the ground Kramers doublet (considering an effective $J_{\mathrm{eff}} = 1/2$) and the energetic separation between it and the first excited level for the two conformers of Cp*ErCOT as obtained from *ab initio* calculations considered the experimental structure at 120K and the DFT-optimized structure.

Ising-like contributions giving rise to average magnetic anisotropy measured but it is not possible to assert if they correspond to a molecular easy-axis directed along the pseudo-symmetry axis of the molecule (solid lines in Figure 4.8) or orthogonally to it (dashed lines).

4.3 Comparison with *ab initio* calculations

In order to unambiguously assign the magnetic anisotropy to the Cp*ErCOT molecule *ab initio* calculations have been performed in collaboration with Prof. Chibotaru's group at Katholieke Universiteit of Leuven in Belgium.

Similarly to what was done in the LnDOTA experiments the method followed is based on the relativistic self-consistent field CASSCF-RASSI-SO/SINGLE_ANISO as implemented in the MOLCAS 7.8 code where in this case to the configuration state functions, determined by the CASSCF method and considered as basis functions, has been applied the RASSI-SO method for taking into account the spin-orbit coupling. After spin-orbit interaction is included the procedures in SINGLE_ANISO allows to treat nonperturbatively temperature- and field- dependent magnetic properties, Zeeman interaction together with zero-field splitting.

Ab initio calculations have been performed considering the structure

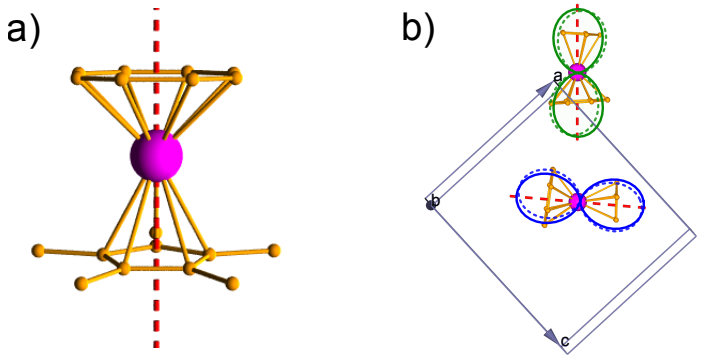

Figure 4.9: a) Easy-axis of magnetization of molecule Cp*ErCOT as calculated from *ab initio* methods. b) Molecular magnetic anisotropy in the plane orthogonal to ω_3 axis obtained from *ab initio* calculations (solid lines) compared to the one obtained from experimental data fitting (dashed lines).

of the Cp*ErCOT determined at 120K taking into account the presence of the two conformers (COT ligand is disordered over two positions with equal populations). On the basis of these geometries calculations revealed that the ground Kramers doublet is expected to be strongly axial, with transverse effective g factors g_x, $g_y < 10^{-3}$, and g_z approaching the value of 18 expected for the ground doublet of a pure Ising $J = 15/2$ state with $g_J = 6/5$ (see Table 4.1). Calculations also showed that the easy axis, corresponding to g_z orientation, lies perpendicularly to the average of the planes of the two rings of COT and Cp* ligands as shown in Figure 4.9 a).

The comparison of the calculated angular plot of the dependence of the susceptibility on the plane scanned by **Rot3** (averaged over the two conformers) with the ones used to reproduce the experimental susceptibility of the crystal is reported in Figure 4.9 b) showing an excellent agreement.

The calculated energy gaps with the first excited Kramers doublet on the two conformers 84.8 and 115.9 cm^{-1} (Table 4.1), are lower than the activation energies, 137 and 224 cm^{-1} obtained from AC susceptibility data by Gao and co-workers.[54] One reason for the observed discrepancy could be addressed to the fact that the experimental geometry used at 120K might not represent the low-temperature geometry accurately enough.

It was for this reason that an optimization of the geometry of the two conformers was tried with the Density Functional Theory (DFT)

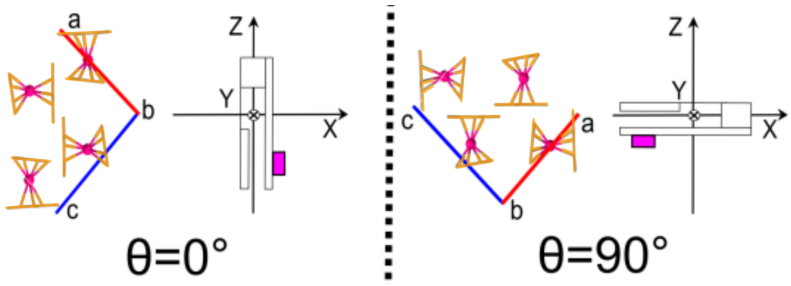

Figure 4.10: Crystal packing and orientation of the molecules in the plane scanned by torque magnetometry at two different angles. The magnetic field is applied along the Z axis of laboratory reference frame.

without taking into account the intermolecular interactions. By using these optimized geometries the principal direction of magnetic anisotropy of the ground Kramers doublets remain practically unchanged with respect to previous calculations. However, the first excitation energy is now obtained at $135\,\mathrm{cm}^{-1}$ for both the conformers, which closely matches the lower activation energy found experimentally.

These results confirm the reliability of *ab initio* calculations in describing the magnetic anisotropy of lanthanide-based compounds together with the importance of flanking results coming from experimental measurements with theoretical predictions in order to better comprise molecular magnetic properties.

4.4 Angular resolved magnetic measurements with capacitive cantilever

Torque magnetometry being insensitive to isotropic magnetic contributions is the ideal tool to analyze the magnetic behavior showed by the Cp*ErCOT on crystallographic plane *ac* where the two almost orthogonal and strongly anisotropic molecular contributions give rise to an average low anisotropic magnetization. A new crystal has been for this reason prepared, and once indexed, it was fixed with Apiezon N grease on the cantilever so that the Y rotation axis of the cantilever and the b crystallographic axis were coincident (the misalignment was estimated to be 1.5°) while

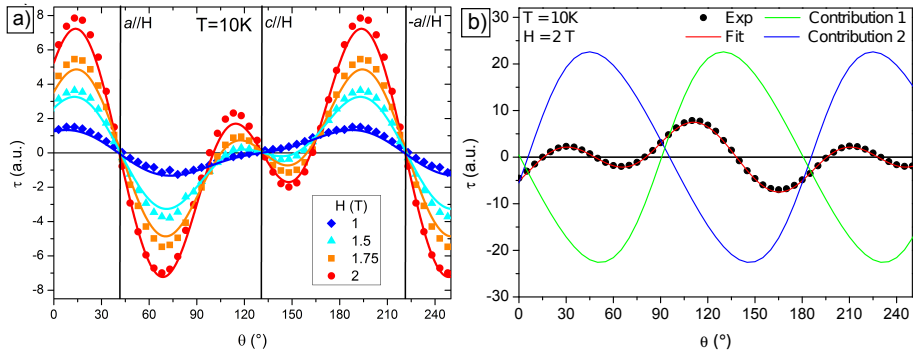

Figure 4.11: a) Angular dependence of the magnetic torque measured at $T = 10$K and different applied magnetic fields. The lines correspond to the fit obtained using two effective $J = 1/2$ (Ising limit) contributions separated by an angle of 94.65° (see Section 4.1). b) Result of the fit (red line) for the magnetic torque measurements at $T = 10$K and $H = 2$T together with the two individual contributions (green and blue lines).

the a axis resulted to be 41° from the normal to the cantilever plate (see Figure 4.10).

Data were collected at variable temperature (in the range from 10 K to 150 K) and magnetic field (from 1 T to 6 T). At any investigated temperature the rotation was also performed in zero field to evaluate the contribution arising from the deflection of the cantilever owing to its own mass and that of the sample. This spurious contribution can be easily identified because it is characterized by a 360° periodicity.

In Figure 4.11 a) are reported the angular resolved magnetic torque measurements at $T = 10$K for different applied magnetic fields. At all the fields the torque profiles cross the zero at $\theta = 41°$ and 131° when the magnetic field is applied along the a and c axis which means that these directions correspond to the principal directions of the magnetic anisotropy of the crystal as a whole. This result is in agreement with what was found by angular resolved magnetization measurements (see Figure 4.8) and is not surprising given the crystal symmetry presenting a glide plane perpendicular to c axis.

Increasing the magnetic field from 1 T to 2 T, beyond an increase in intensity of the torque signal, a modification of the shape observed is evident. As described in Section 2.4.1 this is a signature of the presence of

saturation effects (which become more relevant as the field increases) coming from two axial anisotropic contributions. But unlike the exemplifying model described in Section 2.4.1 the torque signal presents oscillations with different amplitude due to the non-perfect orthogonality of the two contributions.

Collected data have been fitted (continuous lines in Figure 4.11 a considering two $J_{\text{eff}} = 1/2$ Ising contributions separated by the previously found angle $\psi = 94.65°$ (see Section 4.1) whose magnetization was given by the Brillouin equation (1.13). As free parameters were chosen g_{eff} and a scale factor to account for the incertitude on the mass of the sample and on the elastic constant of the cantilever. In Figure 4.11 b is shown what was obtained from the fit procedure for the data collected at $T = 10\text{K}$ and $H = 2\text{T}$ together with the single contributions due to the two symmetry related molecular families. This result confirms the hypothesis of two strong axial contributions obtained from magnetization measurements. Referring to Figures 4.10 and 4.11 b, at $\theta = 0°$, where one molecular family is aligned to the magnetic field and the other is almost orthogonal to it, a zero (or almost) torque is observed for both contributions but with a different slope, which means that the easy direction of one contribution (the less steep one) and the hard one of the other (the steeper one) are observed. The same behavior is observed, with inverted roles, each 90°.

The advantage in using torque magnetometry, given its insensitivity to isotropic contributions, is evident comparing the results obtained at 10K with magnetization measurements. For temperatures higher than 5K, where no hysteretic behavior is present, magnetization data did not allow to discern if the two contributions showed an easy-plane or an easy-axis magnetic anisotropy and the ambiguity was removed only after analysis of magnetization dynamics at lower temperatures. Magnetic torque measurements instead revealed the axial anisotropy of the two molecular families at temperatures where no hysteresis opening is present and without resort to dynamics studies.

In Figure 4.12 are reported the magnetic torque measurements at different temperatures in the range from 20 K to 150 K. In this case on increasing the temperature the saturation effects decrease and the shape become more sinusoidal-like. Also this data have been fitted using the same

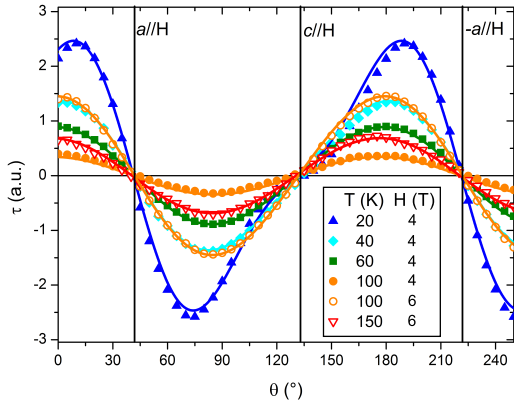

Figure 4.12: Angular dependence of the magnetic torque measured in the temperature range 20 K to 150 K at 2T (filled symbols) and 4T (empty symbols). The lines correspond to the fit obtained using the spin Hamiltonian in Equation (4.4).

model described above and the obtained g_{eff} are reported in Figure 4.13 as a function of temperature and for different magnetic fields. The progressive decrease of g_{eff} for T higher than 60K indicates a depopulation for these temperatures of the ground doublet $J = 15/2$ in favor of higher levels thermally populated. This result is in accordance with the energy separation found from *ab initio* calculations.

The experimental data collected have also been analyzed by using a spin Hamiltonian describing the effects of the crystal field on the $J = 15/2$ multiplet. To avoid overparametrization problems a unique set of crystal field parameters have been used, notwithstanding the presence of two conformers. This appears justified by the results obtained from *ab initio* calculations which showed only small differences between the energies of the two conformers. Also if even small deviations from a perfect axial symmetry can produce non-negligible contributions, given the small tilt angle between the organic rings that act as ligands, transverse terms have been neglected at first approximation as well as the sixth-order terms since it was found that they didn't significantly improve the simulation. The calculations were so carried out by using the spin Hamiltonian:

$$\mathcal{H} = g_L \mu_B \mathbf{J} \cdot \mathbf{H} + B_2^0 O_2^0 + B_4^0 O_4^0 \,. \tag{4.4}$$

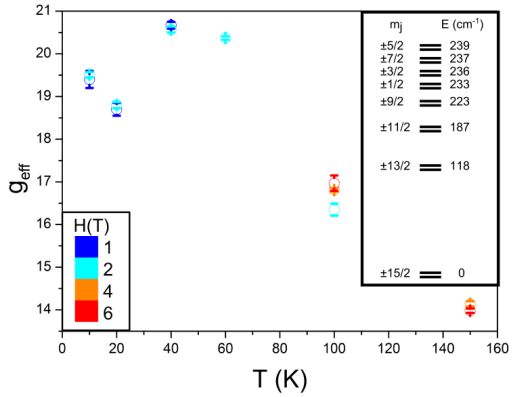

Figure 4.13: Temperature dependence of g_{eff} values obtained from magnetic torque data fit at different fields. In the inset the energy levels diagram scheme from spin Hamiltonian

The experimental data were successfully reproduced (solid lines in Figure 4.12) notwithstanding the approximations made. The best fit parameters were: $B_2^0 = -1.3(1)\,\text{cm}^{-1}$ and $B_4^0 = -3(1) \times 10^{-3}\,\text{cm}^{-1}$. The tilt angle between the easy axis of the two families of molecules was also fitted and the resulting value (95(1)°) agrees with previous estimations. The calculated energy levels of the ground J manifold obtained with these parameters (see inset in Figure 4.13) provide an estimate of the energy separation between the ground and the first excited doublet of $118\,\text{cm}^{-1}$ which is in good agreement with those obtained from *ab initio* calculations.

In order to extract information regarding magnetic bistability from torque measurements, hysteresis loops at a fixed temperature and angular position have been recorded, varying the sweeping rate of the applied magnetic field, as reported in Figure 4.14. Irreversibility is clearly observed at 5K and the dynamic origin of the hysteresis is well evidenced by the differences upon changing the sweeping rate.

As stated in Section 2.4.1 the magnetic torque always vanishes at zero applied field and torque magnetometry is, therefore, unable to detect remnant magnetization. However, information if a remnant magnetization is present or not can be the same extracted from hysteresis loops with torque magnetometry. If the system presents no remnant magnetization

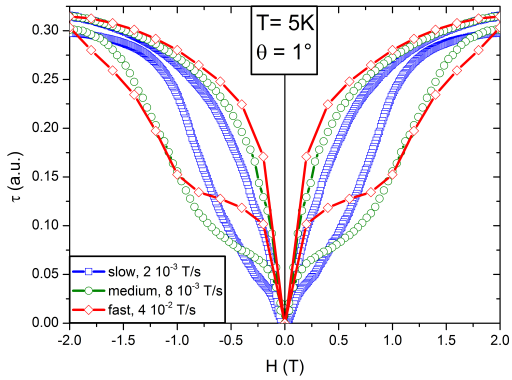

Figure 4.14: Temperature dependence of g_{eff} values obtained from magnetic torque data fit at different fields. In the inset the energy levels diagram scheme from spin Hamiltonian

when the magnetic field crosses the zero changing sign the same does the magnetization so the sign of magnetic torque $\boldsymbol{\tau} = \mathbf{M} \times \mathbf{H}$ remains unchanged. On the opposite situation, when the magnetic field crosses the zero, the magnetization still presents its remnant value and only $\mathbf{H}$ changes sign involving a change in sign of the measured torque.

In the hysteresis loop showed in Figure 4.14 the torque has the same sign over the entire loop, thus indicating that this system presents no remnant magnetization, and is actually characterized by a butterfly hysteresis cycle as observed by standard magnetometry.

5 Electric transport measurements on spintronics devices containing magnetic molecules

In this chapter the explorative results of the electric transport characterization of devices comprising magnetic molecules will be presented. This kind of study falls within the field of spintronics and more in general of molecular electronics.

The term spintronics is the blend of the words "spin" and "electronics". As suggested by the word itself, it concerns the study of spin polarized electric currents and can be thought as the union of electronics (which only deals with the electric charge of carriers) with magnetism allowing in this way to exploit the fact that electric currents consist of spin-up and spin-down carriers which in general interact differently with magnetic materials.

The first spintronics effect reported can be traced back to the Johnson and Silsbee work[59] in 1985 on injection of spin-polarized currents though probably the most known (and surely one of the most exploited in technology) is the giant magneto resistance (GMR) effect. It was discovered independently by the groups of Fert[60] and Grünberg[61] in 1988 in layered magnetic thin-film structures composed of alternating layers of ferromagnetic and nonmagnetic layers. When the magnetic moments of the ferromagnetic layers are parallel, the spin-dependent scattering of the carriers is minimized, and the structure presents its lowest resistance. When the ferromagnetic layers' magnetic moments are antiparallel, the spin-dependent scattering of the carriers is maximized, and the device has

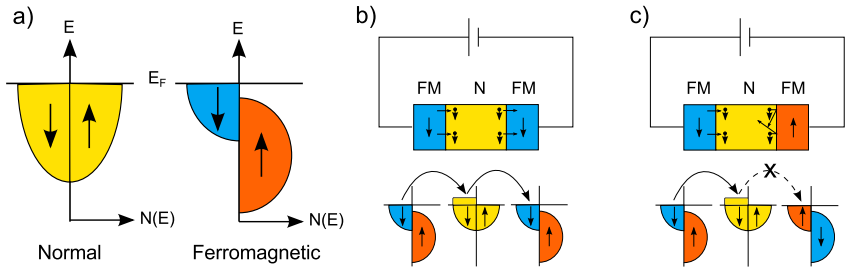

Figure 5.1: a) Schematic representation of the density of electronic states for a normal and a ferromagnetic metal; b) spin-polarized transport from a ferromagnetic metal, through a normal metal, into a second ferromagnetic metal for aligned magnetic moments and c) antiparallel magnetic moments.

its highest resistance. The physical principle governing this phenomena is sketched in Figure 5.1 where a structure constituted of one nonmagnetic layer between two magnetic layers is considered. In a ferromagnetic material, unlike of what happens in nonmagnetic one, the spin populations at the Fermi energy present an imbalance due to the shift in energy between the spin-up and spin-down density of states (which is also the source of the net magnetization of the material) as illustrated in Figure 5.1 a. The different values of density of state at the Fermi level for the two spin populations is at the origin of the spin-polarized current outgoing from the first ferromagnetic layer and at the same time is the source of the different values of resistance measured in respect of the different magnetization state of the two magnetic layers. When the magnetization of the ferromagnetic layers are parallel (Figure 5.1 b) the spin-polarized carriers coming from the source layer find in the second ferromagnetic layer available energy levels and the resistance measured is low. On the opposite situation (Figure 5.1 c) the spin states corresponding to the spin polarization of the current are filled, no available energy levels are present at the Fermi levels and the resistance measured is thus higher. Devices like the one just described are also known as *spin-valves* and are adopted as magnetization detectors in actual hard disks reading heads.

After these discoveries the researches concerning spintronics grew considerably given also the high technological impact that spans from more efficient data storage to energy saving.

In this panorama the possibility of exploiting the magnetic properties at molecular scale offered by SMMs and magnetic molecules in general did not go unobserved[5,6,62] and several studies concerning spintronics properties of structures containing magnetic molecules have been conducted[11,63–67] revealing to be also an alternative to the traditional magnetometry measurements in studying the magnetic anisotropy of SMMs.[68]

In the following sections the first results obtained from electric transport measurements on devices containing magnetic molecules and SMMs are reported. Two different kind of structures have been studied: the first, made in collaboration with the group of Dr. Giuseppe Maruccio from the Università del Salento in Lecce, consists of a network of gold nanoparticles and functionalized Fe_4 SMMs obtained by layer-by-layer deposition on interdigitated electrodes. The second device, developed in collaboration with the group of Dr. Valentin A. Dediu from ISNM-CNR of Bologna, is instead an organic spin-valve (OSV) whose behavior has been analyzed in two different configuration: one comprising an evaporated multilayer of Fe_4 SMMs the other with a monolayer of chemisorbed nitronyl nitroxide radicals (NNR).

5.1 Electric transport measurements on functionalized gold nanoparticles network systems

Reported spintronics experiments involving SMMs mostly concern the study and characterization of electric transport through a single molecule junction[62] making use of nanojunctions,[63,66,69] scanning tunneling microscopes[70] or grafting the SMM on graphene or carbon nanotubes.[11,64] Though fascinating results were obtained with experiments on single molecule junctions the major drawback of these kind of techniques is represented by the variability in the bonding geometry at the contacts. This, coupled with thermal fluctuations, induces a variability in the transport features affecting the reproducibility of the measurements.

For this reason in the experiments described here a different approach was chosen aiming at an ensemble of magnetic molecules acting together where the behavior of the system is determined by the average behavior of all the molecules involved.

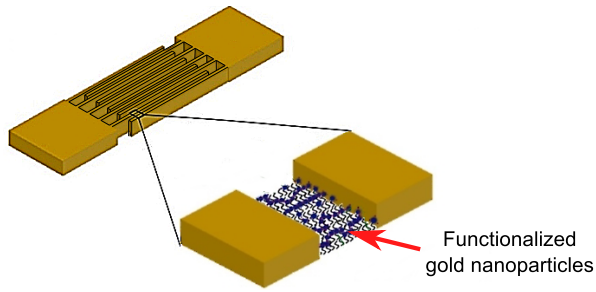

Figure 5.2: Schematic representation of the interdigitated electrodes.

The first typology of device studied consists of two interdigitated electrodes connected by a network of gold nanoparticles (AuNPs) opportunely functionalized (see Figure 5.2). The effects on the current flowing through the device on varying the molecules linking the AuNPs and the number of deposited layers has been studied.

Interdigitated electrodes are substantially made of a noncunductive substrate on which two faced comb electrodes are deposited. Their utilization covers a wide range of applications which include microwave integrated circuits,[71,72] optical and surface acoustic wave devices,[73] thin-film acoustic–electronic transducers and tunable devices,[74] humidity[75,76] and chemical sensors,[77,78] just to mention a few.

The electrodes used consisted of a pair of 25 fingers (width 5 µm) separated by a 5 µm gap and were fabricated by standard photolithography and lift-off techniques by the group of Prof. Giuseppe Maruccio. In particular the image reversal photoresist AZ5214 and a Karl Suss MJB3 mask aligner were employed. The substrate chosen consisted of Si with a 5 µm thick SiO_2 capping layer. In order to facilitate the adhesion of the gold electrodes on the substrate a 6 nm thick Cr layer was thermally evaporated before proceeding with the 60 nm thick Au layer deposition.

To implement the hybrid devices, the Si/SiO_2 substrate between the electrodes was first silanized using 3-Mercaptopropyl-trimetoxy silane in order to expose a free thiol termination useful for subsequently attaching the active layers.[79]

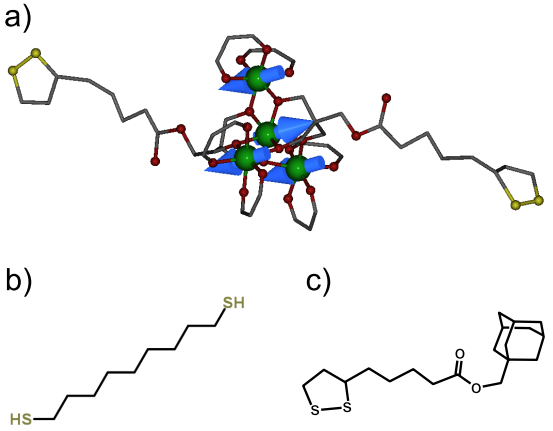

Figure 5.3: a) Fe_4thioctic molecule. The arrows depict the antiferromagnetic spin configuration of the $S = 5$ ground state. Color code: Fe green; C gray; O red; S yellow; hydrogen atoms are omitted for clarity. b) Chemical structure of 1, 9 nonanedithiol. c) Chemical structure of adamantane thioctic ester.

The next step was the layer-by-layer growth of the active film by the subsequent deposition of gold nanoparticles and functionalized molecules of Fe_4thioctic ($[Fe_4(L)_2(dpm)_6]$ with H_3L representing 7-(acetylthio)-2,2-bis(hydroxymethyl)heptan-1-ol and Hdpm representing dipivaloylmethane) a derivative of the Fe_4 SMM functionalized with two 1,2dithiolane terminated arms specifically designed for binding on gold (Figure 5.3 a). Every layer deposition was obtained by dipping the devices first in a solution in dichloromethane of AuNPs (2.2×10^{13} particle/mL) then in a 3mM solution in dichloromethane of Fe_4thioctic. The geometry of these interdigitated electrodes presents the advantage of a high facing surface in a small dimension device allowing thus the presence of a greater number of links with functionalized AuNPs in respect to other electrode geometries of the same dimensions.

The Fe_4thioctic molecule belongs to the Fe_4 SMMs family where four high spin Fe^{III} ions ($S = 5/2$) are arranged in a centered triangular topology (see Figure 5.3 a). Antiferromagnetic interactions between the central and peripheral spins, mediated by the bridging oxygen atoms of the tripodal ligands, lead to a ground state with total spin $S = 5$. These molecules have demonstrated to be SMMs characterized by an uniaxial magnetic anisotropy

($D/k_B \approx -0.6K$) directed along the normal to the plane defined by the four metal ions giving rise to a potential barrier $\Delta E \approx 15$K.[80] Moreover Perfetti et al.[81] showed the effective creation of a network between AuNPs and the Fe_4thioctic molecules with the persistence of SMM behavior in this new hybrid nanostructure.

In order to prove the contribution to conductance arising from Fe_4 other than from NP, a comparison making use of a 3mM solution of dithiols (1, 9 nonanedithiol, Figure 5.3 b) in place of Fe_4 SMMs was performed. Indeed dithiols can bind simultaneously two NPs thus a direct comparison with multilayer structures containing Fe_4 allows to extract the SMMs contribution.

Devices with the active molecular layer obtained by using a 3mM solution of adamantane thioctic esters (ADM, Figure 5.3 c) have also been studied. ADM molecules are characterized by having only one arm able to bind gold, so when NPs are functionalized with this derivative no connections between them occur. In this way comparing the behavior of ADM functionalized devices with the others it is possible to determine the contribution to the electric transport provided by molecular links between AuNPs.

The electrical characterization was performed on about 100 junctions functionalized as described above. The measurements were performed using a programmable DC voltage source Yokogawa 7651 reading the electric current through the interdigitated electrodes with a a HP34410 digital multimeter. Given the low values of current in play a low-noise current preamplifier (SR570) was also employed. Experiments were carried out in the voltage range of -200 mV to 200 mV. At room temperature, a probe station was used while low temperature measurements were carried out within a Variable Temperature Insert (VTI) system and a cryostat by Cryogenic.

In Figure 5.4 are reported the I-V curves at room temperature for two devices functionalized with Fe_4thioctic SMMs obtained at different steps of functionalization. For all the devices characterized with Fe_4thioctic, only a few junctions exhibited current values around few nA at 200mV similar to the ones shown in Figure 5.4 a while, in the remaining devices, the average

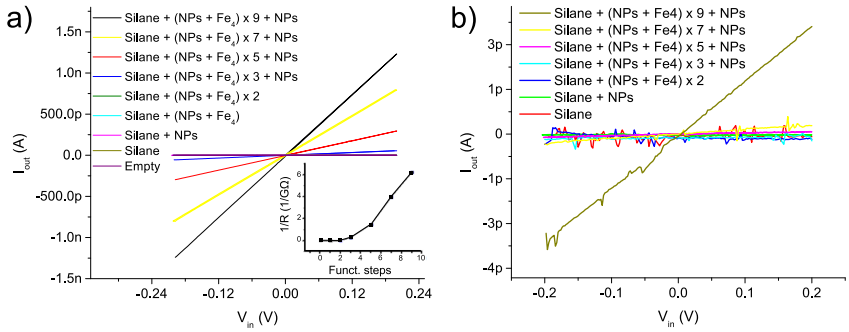

Figure 5.4: I-V characteristics at room temperature of one of the devices showing high a) and low current values b). In the inset of a) conductance of functionalized interdigitated electrodes on varying the number of functionalization steps is reported.

current was about 10pA at 200mV, like the one reported in Figure 5.4 b. In all cases almost linear I-V characteristics were observed.

Data collected reveal an increase in the current with the number of cycles of functionalization (see inset in Figure 5.4 a): in the junctions with high current, after 9 steps of functionalization, resistance decreased from an average value of 400GΩ (1 layer) to 0.1 GΩ (9 layers) while in the majority of junctions with low current the decrease was in average from 400GΩ (1 layer) to 50GΩ (9 layers).

Both the increase in the current with the number of functionalization steps and the variation in current measured can be explained using a percolative model. Indeed, at each step, nanoparticles or molecules get attached to the silane or to the open ends of the previously immobilized film. As a result, the number of particles attached to the substrate increases with the number of deposited layers as well as the probability of obtaining a complete conducting channel. On the other hand, depending on the number of such conducting channels connecting source and drain electrodes within each junction, the current may differ from device to device.

The I-V characteristics at room temperature concerning the interdigitated electrodes functionalized with dithiols and ADM molecules are reported in Figure 5.5. Data regarding dithiols (Figure 5.5 a) present resistance values lower than the ones observed in devices functionalized with Fe_4thioctic. Moreover no important differences are found in increas-

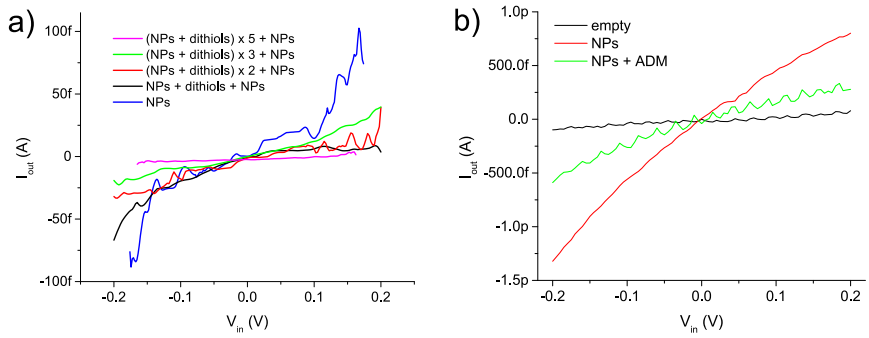

Figure 5.5: I-V characteristics at room temperature for devices functionalized with dithiols a) and ADM b).

ing the functionalization steps. Concerning the conductance properties of AuNPs\dithiols systems, Ogawa[82] reported in the case of AuNPs functionalized with 1,10-decanedithiols, a negligible current at low voltages while a Schottky type increase in current was observed at voltages higher than 4V. Since measurements in devices containing dithiols were performed for comparative purpose, low voltages until 200mV were applied and the results are compatible with the previous work of Ogawa.

Making reference to Figure 5.5, once functionalized with ADM molecules, the devices showed a decrease in the intensity of current measured. This is in accordance with the properties of the ADM molecule which possesses only one arm able to bind with AuNPs avoiding in this way the formation of molecular links between AuNPs and as a consequence making the creation of conducting channels more difficult.

In the case of interdigitated electrodes functionalized with Fe_4thioctic temperature-dependent measurements were also carried out recording I-V characteristics at 1 5K, 50K, 100K and 150K. As shown in Figure 5.6, the current at a specific voltage was found to decrease significantly with the temperature suggesting the presence of a thermally assisted process at the origin of electric transport through the device. The temperature trend of current can be described by the relation:

$$I(T) = I_0 \exp -\frac{\epsilon}{k_B T} \;\Rightarrow\; \ln I(T) = -\frac{\epsilon}{k_B T} + c \tag{5.1}$$

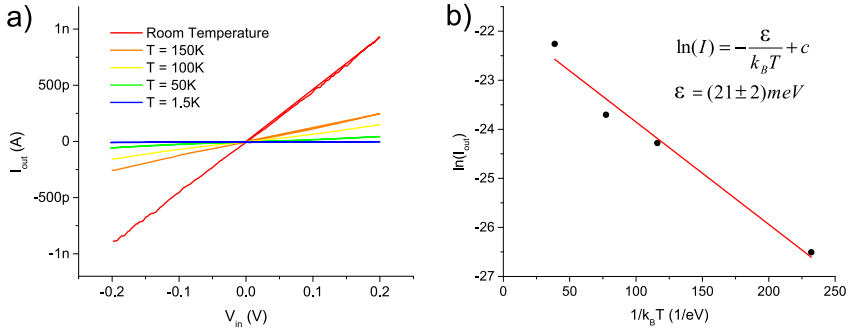

Figure 5.6: a) I-V characteristics for a Fe_4thioctic functionalized device at different temperatures; b) logarithm of the current at 50mV. The red line represent the result of the fit obtained from equation 5.1.

ϵ being the activation energy for electric transport. In Figure 5.6 b the logarithm of the current at 50mV is plotted as a function of $1/k_BT$. A linear fit using equation 5.1 (whose result is shown as a red line in Figure 5.6 b) gave an estimation for the activation energy value of 21(2) meV.

These preliminary results show that Fe_4thioctic\AuNPs structures obtained by layer-by-layer growth present a measurable electric response related to the number of functionalization steps and describable with a percolative model. Temperature behavior of I-V characteristics revealed the presence of thermally activated processes at the basis of the electric transport with an activation energy of 21meV. Moreover at room temperature the electric conductivity of Fe_4thioctic functionalized devices was observed to be higher than in devices functionalized with dithiols and ADM molecules.

In order to exploit possible features in electric transport depending on magnetic properties of the SMM Fe_4thioctic, experiments in the presence of magnetic fields are planned. On the other hand given the low conductivity observed at low temperatures, experiments with different device architectures are under investigation.

5.2 Organic spin-valve devices containing magnetic molecules

One of the limitations presented by the spin-valve model illustrated at the beginning of the chapter is represented by the intermediate non magnetic metal. In order to work properly the spin-polarized injected current must retain, as much as possible, its spin polarization value until it arrives to the second ferromagnetic layer. In passing through the non magnetic layers, carriers are subjected to spin relaxation processes towards the thermal equilibrium which for a non magnetic material corresponds to equal spin populations. This relaxation processes are mainly due to spin-orbit and hyperfine interactions and are characterized by two quantities: the spin-relaxation time, τ_s, (i.e. the average time that an electron spin takes before changing its original direction) and the spin-relaxation length, l_s (i.e. the average distance traveled by a spin before changing direction).

Organic semiconductors (OSC), widely used in commercial hybrid light-emitting diodes with organic emitters (OLEDs), present weak spin-orbit interactions assuring values for τ_s ranging from 10^{-6} s to 10^{-3} s[83,84] which widely exceed the spin-relaxation times present in inorganic materials (10^{-9} s to 10^{-12} s).

The first reported spintronics effect in an organic device is dated 2002 by Dediu et al.[85] where a layer of the organic molecules sexithiophene (already known for its OSC properties[86,87]) acted as conducting channel in a horizontal geometry between two ferromagnetic electrodes made of manganite $La_{0.7}Sr_{0.3}MnO_3$ (LSMO). This device showed a sizable resistance dependence on magnetic field (magnetoresistance) up to room temperature explained as a consequence of the conservation of the spin polarization of the injected carriers.

5.2.1 Description of the vertical geometry OSV studied

For this work the OSVs with vertical geometry illustrated in Figure 5.7 have been studied. The multilayer structure is the same as that of the OSV described by Dediu et al.[88] with the addition of a layer of magnetic molecules in order to determine how the spin-valve behavior can be affected by their presence.

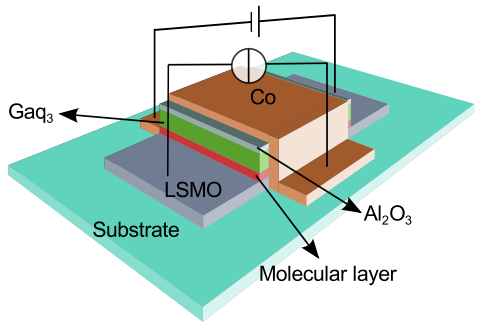

Figure 5.7: Schematic representation of the organic spin-valve device and its layered structure (not in scale): over the NGO substrate is present a 40 nm LSMO followed by the magnetic molecules layer (a molecular monolayer for the device comprising the NNR while a 10 nm film for the spin-valves containing the Fe_4Ph). A 150 nm thick layer of OSC Gaq_3 is deposited over the molecular one and capped with a Co electrode (35 nm height). A 2 nm Al_2O_3 tunnel barrier is interposed between the OSC and Co layers.

- **LSMO layer**

Making reference to Figure 5.7 the first layer of the structure is constituted by an LSMO epitaxial thin film (thickness 40 nm) grown on $NdGaO_3$ (110) by Channel Spark Ablation provided by the group of Dr. V. A. Dediu.[89]

The choice of LSMO has been made for its high percentage of spin-polarized carriers which for temperatures below $T \ll T_c \approx 320 - 330$K can reach values near 100%:[90] in this condition LSMO easily accepts carriers with spin parallel to the average spin polarization and offers a colossal resistance to the carriers with opposite spin polarization[91] making this material a good choice as spin-polarized carriers injector/detector.

Before proceeding with the subsequent layers deposition, the LSMO film has been widely characterized making use of Low Energy Ion Scattering measurements (LEIS) and angular-resolved x-ray photoemission spectroscopy (AR-XPS). The characterization of the LSMO layer as well as the NNR layer described in the following have been mainly conducted by Lorenzo Poggini and are part of his PhD thesis.[92] The importance of such characterization lies in the fact that the interface between the inorganic and organic phases can strongly affect the spin injection processes.[93–97] Not

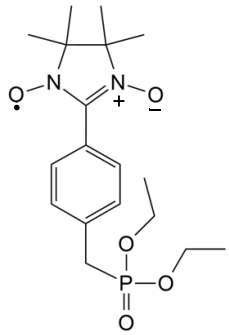

Figure 5.8: Chemical structure of the functionalized ethyl phosphonate NNR used for the molecular monolayer.

less important, the chemical composition and stoichiometry of the LSMO surface directly influence the choice of molecules that can be grafted and the best procedure to do this.

Results obtained indeed showed different concentration ratios La/Sr between the topmost layer and the bulk value having on the surface a higher concentration value of Sr as already found in previous studies.[98–101]

The second layer of the spin-valve device is constituted by the magnetic molecules layer. Two different configurations have been considered exploiting two different molecules: the organic radical Nitronyl Nitroxide Radical (NNR) in the first and the Fe_4Ph SMM in the second.

- **NNR layer**

Among the organic radicals (i.e. molecules with at least one unpaired electron) NNRs are characterized by a good chemical stability. Due to the presence of an unpaired electron, essentially localized in a NO group (see Figure 5.8), NNRs can serve as an additional spin layer at the interface between a spin injecting electrode and a OSC layer. These molecules result particularly interesting since they feature long-range magnetic order[102] at low temperature and it has been theoretically and experimentally demonstrated that partial ordering of the molecules can be achieved also at the nanoscale.[103,104]

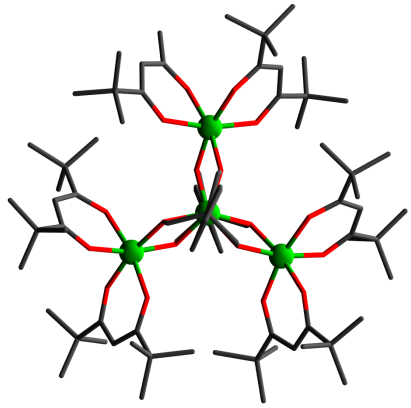

Figure 5.9: View of the structure of the Fe_4Ph along the the normal to the plane defined by the four Fe^{III} ions. Color code: Fe green; C gray; O red; hydrogen atoms are omitted for clarity.

A self-assembled monolayer procedure has been followed to obtain the molecular monolayer. In order to chemically graft the NNRs molecules on the LSMO surface they have been previously functionalized to obtain an ethyl phosphonate NNR system (2-(diethyl 4-methylbenzylphosphonate)-4,4,5,5-tetramethylimidazoline-1-oxyl-3-oxide) represented in Figure 5.8. The deposition of the monolayer on the LSMO surface and the effective presence of a chemical bond between NNRs molecules and the surface have been obtained by incubating the molecules in a 3mM in dichloromethane/methanol 3:1 and then confirmed by ToF-SIMS analysis.[92]

- **Fe_4 layer**

In the second configuration a molecular layer (thickness 10 nm) of Fe_4Ph ($[Fe_4(L)_2(dpm)_6]$ where Hdpm is dipivaloylmethane and H_3L is the ligand 2-hydroxymethyl-2-phenylpropane-1,3-diol, see Figure 5.9) has been deposited by thermal sublimation on the LSMO surface.

Furthermore Fe_4 SMMs demonstrated that they can retain their magnetic properties once chemisorbed as monolayers on a gold substrate[12,105] as well as once thermally sublimated on both nonconductive[106,107] and conductive substrates.[108]

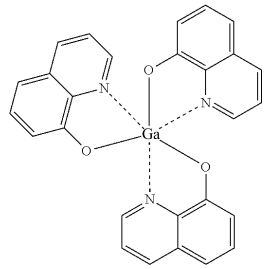

Figure 5.10: Chemical structure of Gaq_3 molecule.

- **OSC layer and Co electrode**

After functionalization of the LSMO surface a 150 nm thick layer of Gaq_3 (tris(8-hydroxyquinoline) gallium) has been grown by organic molecular beam deposition. This layer constitutes the OSC component of the spin-valve where the Gaq_3 is a molecule already studied for its light emission properties.[109,110]

Two different magnetic electrodes characterized by different values of coercive fields are required in order to observe the spin-valve effect modifying selectively the magnetization value of the single electrode. For this reason the outer ferromagnetic electrode is constituted by a 35 nm rf sputtered Co layer.

An additional layer of Al_2O_3 (thickness 2 nm), grown by pulsed plasma deposition, is interposed between the Co and Gaq_3 layers to avoid interdiffusion of the metal inside the OSC. This could give rise to a not well-defined interface together with the possible creation of short-circuits between the two ferromagnetic layers.

5.2.2 Electric transport measurements on OSVs

In order to perform measurements at low temperature and in the presence of an external magnetic field a Physical Properties Measurement System (PPMS) by Quantum Design has been used. The PPMS provides indeed the possibility to collect measurements in a range of temperatures from 1.9 K to 350 K, being equipped with a pumped ^{4}He cryostat, and to

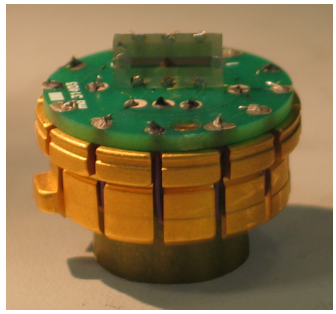

Figure 5.11: Sample-holder used for electric transport measurements with one of the devices measured mounted on it.

apply magnetic fields up to $\pm$9T supplied by a superconductive magnet. It also offers the possibility of performing electric measurements by using a removable sample holder provided with electric connections. The sample-holder is constituted by an oxygen-free high-conductivity copper puck that maintains high thermal uniformity. In order to prevent oxidation the puck is gold-plated. To facilitate the connection of the samples, a custom designed printed circuit board (PCB) has been created and soldered to the electric connection of the sample-holder. In Figure 5.11 is shown a photograph of the sample-holder with one of the devices measured. Each device is constituted of a substrate (10 mm $\times$ 5 mm) on which three OSVs are present and is connected to the PCB by means of gold wires and silver-paint.

Being the PPMS an instrument designed mainly to perform magnetic measurements, the provided electric transport measurements option did not reveal to be the best solution for measurements on OSVs. For this reason a source-meter unit (SMU, Keithley 2601A) has been interfaced with the PPMS. The SMU can operate as a current source, measuring the current (max. resolution 1 pA, depending on measuring range) or as a current source, measuring the voltage (max. resolution 1 µV, depending on measuring range) in both 2- and 4-wire sensing mode. The SMU has also been connected to the computer managing the PPMS in parallel with the PPMS itself through a GPIB cable. In this way it is possible to manage at the same time both temperture and magnetic field (provided by PPMS) and electric measurements with the SMU. This required specific Visual Basic routines to remotely control the instruments allowing to perform

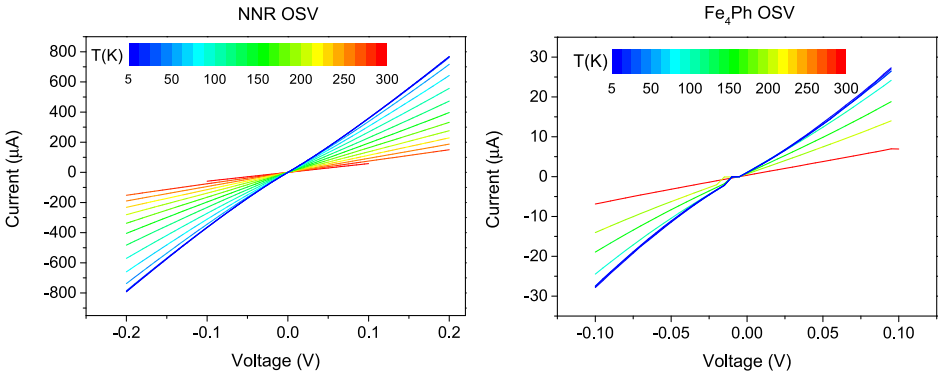

Figure 5.12: Sample-holder used for electric transport measurements with one of the devices measured mounted on it.

automatically several experiments by writing customized sequences of measurements.

In Figure 5.12 are reported the I-V curves collected at different temperatures for two OSV devices containing respectively the NNR molecular monolayer and the Fe_4Ph layer. The data show an almost linear dependence of current-voltage relationship which let us exclude the presence of high interface barriers for both the devices. Also the temperature dependence confirms metallic-like behavior. The small asymmetry present between positive and negative voltages can be explained by the device asymmetry.

Beside I-V characterization, resistance measurements in dependence of an external magnetic field have been performed at different temperatures in a range from 2.5 K to 300 K. The magnetic field was directed parallel to the device surface, while the electric measurements were collected in 2-wire sensing mode maintaining a fixed electric potential difference $V_{\mathrm{Co}} - V_{\mathrm{LSMO}} = 100\,\mathrm{mV}$ between the LSMO and Co. Being $V_{\mathrm{LSMO}} < V_{\mathrm{Co}}$ the LSMO electrode acts as electron spin-polarized injector.

In Figure 5.13 one magnetoresistance measurement is reported obtained at 3 K on an OSV with NNR. From these data a spin-valve effect is evident even though with an opposite behavior respect to the spin-valve described at the beginning of this chapter. Indeed this system presents a high resistance

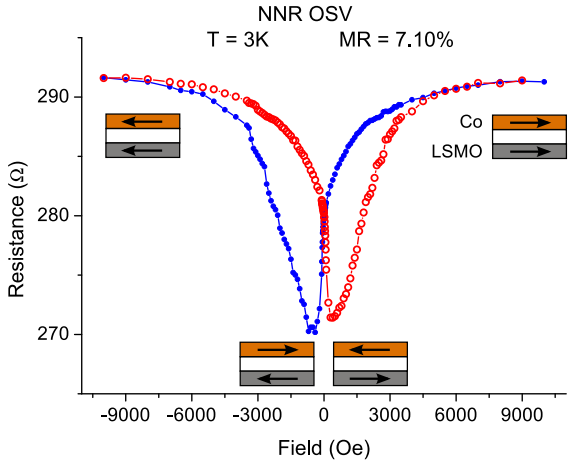

Figure 5.13: Resistance measurements in dependence of an external magnetic field at 3K for an OSV containing NNR molecular monolayer. A schematic representation of the magnetic moments of the electrodes of the device is given in correspondence of the maxima and minima values of resistance.

value when both the magnetic moments of the electrodes are aligned with the magnetic field. This inverse effect is qualitatively in line with the behaviour found in similar OSC-based spinvalves without the NNR layer. Once the magnetic field reaches the value of the LSMO coercive field, the device in an antiparallel configuration of the magnetic moments of the electrodes presents the lowest resistance value. On continuing to decrease the field, once both the magnetic moments are again aligned to the external field, the resistance of the device returns again to its highest value. The switch from one resistance state to the other does not appear to occur at a specific field but rather a smooth transition is observed. This behavior can be ascribed to interface effects at the borders of layers. As will be shown, changing the magnetic molecules' layer indeed affects the shape of the magnetoresistance curves.

In order to quantify this behavior, being $R_{\uparrow\uparrow}$ and $R_{\uparrow\downarrow}$respectively the resistances of the device when the magnetic moments of the electrodes are parallel and antiparallel, we define the magnetoresistance (in percentage) as:

$$\mathrm{MR} = \frac{R_{\uparrow\uparrow} - R_{\uparrow\downarrow}}{R_{\uparrow\uparrow}} \times 100 \; . \tag{5.2}$$

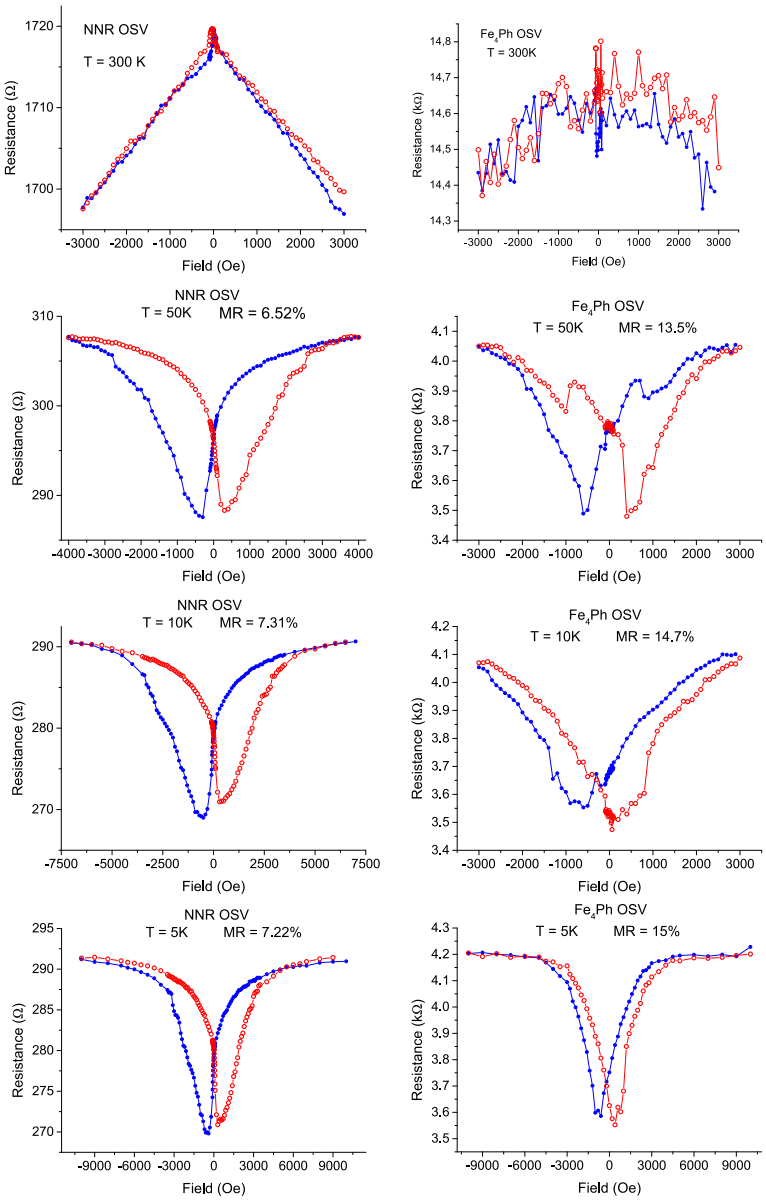

Figure 5.14: Resistance measurements in dependence of an external magnetic field at different temperatures for OSV containing NNR molecular monolayer (left) and Fe_4Ph layer (right).

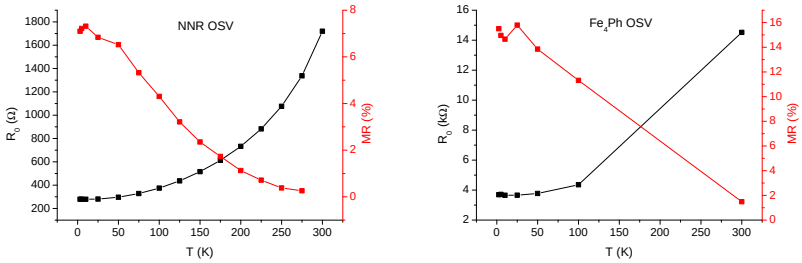

Figure 5.15: Temperature dependence of R_0 (in black) and MR (in red) of an OSV comprising the NNR monolayer (on the left) and one with the Fe_4Ph layer (on the right).

In Figure 5.14 are shown the magnetoresistance data collected at room temperature, 50K, 10K and 5K for both the OSVs containing the NNR and Fe_4Ph layer together with the related MR values, while in Figure 5.15 the temperature dependence of MR and of the resistances in zero magnetic field R_0 are reported for both device typologies. The decrease of R_0 with the temperature confirms the metal-like behavior of the heterostructures studied. On the contrary, in all the samples studied, the appearance of significant magnetoresistance effects occurred at temperatures lower than $270 - 250$K. At the same time MR increased on lowering the temperature reaching values as high as 8% and 15% at $T < 10$K for the devices comprising NNR and Fe_4Ph respectively. These results are in accordance with the reported temperature dependence of spin-polarization in LSMO films[111] which let us infer that temperature dependence of MR in OSVs devices studied is governed by the manganite electrode.

All the devices studied present the inverse spin-valve effect outlined before. The opposite behavior in spin-valve effect observed is common to other reported OSV devices[88,112–114] but the origin of such an effect is still under debate. Indeed both Co and LSMO are majority-spin injector,[83] which should imply a lower resistance for a parallel configuration. Unlike what happens in metals, electric transport in OSC materials is not related to the presence of conduction and valence bands but rather to hopping processes between molecular orbitals. In particular the situation at the interfaces between metals and organic materials plays a fundamental role in

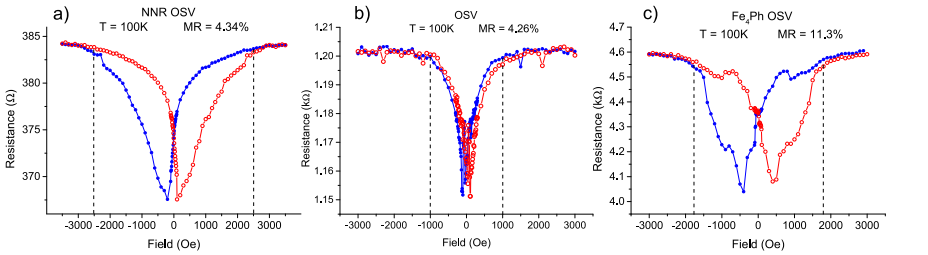

Figure 5.16: Comparison of magnetoresistance measurements at 100K of OSVs comprising a) NNR molecular monolayer , c) Fe_4Ph layer and b) without magnetic molecules layer. Dashed line individuate the magnetic filed at which the OSVs devices switch to the high resistance state.

OSVs devices where effects like broadening of molecular orbitals or energy levels shifts must be taken into account. One of the proposed solutions[88] tries to explain the inversion of the magnetoresistance by assuming that the transport of the majority-spin carriers is occurring by hopping processes through molecular orbitals lying above the Fermi levels of the electrodes where the density of state is higher for the minority-spin for both Co and LSMO. This situation together with spin relaxation processes in OSC would explain the observed magnetoresistance behavior in LSMO\OSC\Co heterostructures.The question is however still unsolved and the exact understanding of what happens in a metal/organic interface remains a puzzle.

The experiments performed, although preliminary, demonstrate anyway the presence of a spin-valve effect in OSVs devices comprising magnetic molecules and, to our knowledge, this represents the first reported case. A comparison with an OSV without magnetic molecules' layer is reported in Figure 5.16 for measurements collected at 100K. The presence of a magnetic molecules' layer interposed between the LSMO electrode and the OSC layer seems to affect the magnetoresistance field dependence shape in particular concerning the value of magnetic field required to restore the high resistance state which, as already stated, is indeed related to the change of the magnetization at the interface with LSMO. In particular, making reference to Figure 5.16, in the device without magnetic molecules layer the magnetization at the LSMO/Gaq_3 is switched at magnetic field $H \approx 1000$Oe; on changing the interface by adding the magnetic molecules

layer the magnetic field required increases going to $\approx$ 1800Oe for the Fe_4Ph-OSVs and $\approx$ 2500Oe for the NNR-OSVs. These results represent a further confirmation of how important the interfaces are in the transport properties of organic based devices.

Also if additional measurements are required in order to obtain a better statistics in the results, from the experiments conducted the use of magnetic molecules' layers demonstrated to be promising in both the development of new OSVs' heterostructures and a better comprehension of the processes at the interfaces related with the magnetization of LSMO electrodes and carriers spin-injection.

Further experiments are planned involving both the variation of parameters such as the height of the molecular layer and the use of different magnetic molecules. It is important to stress that Fe_4Ph and NNR molecules are both paramagnetic in the range of temperature investigated: different electric transport behaviors could be revealed if the experiments would be performed in the presence of a magnetic hysteresis of the molecular layer itself. Moreover the study of the effects on transport properties due to electric fields through the OSVs in search of possible varistor or memristor properties also represents a research field still to be explored.

Conclusions

In this work the results obtained from experiments on different systems comprising magnetic molecules and SMMs were presented. The experiments performed made use of several techniques and methods spanning from the characterization of the magnetic anisotropy of the molecules to the electric transport properties of spintronics devices.

The importance of an appropriate understanding of the magnetic anisotropy driving mechanisms turns out to be essential to confirm synthetic strategies for new and better performing SMMs as well as to develop heterostructures with the desired magnetic properties in the light of a possible technological application.

Results obtained from experiments on SMMs single crystals stress the importance of physical-chemical studies in understanding the mechanisms that lie behind the magnetic anisotropy of such molecules. Angular resolved magnetic measurements with the horizontal rotator proved to be a powerful tool in characterizing samples presenting a magnetic anisotropy. In particular, the experiments conducted on the series of DOTA complexes with the late lanthanide ions confirmed the capability of this method in determining the magnetic anisotropy of the single molecules when in the presence of compounds crystallizing in the triclinic system or, in general, when a unique orientation of the molecules is present in the crystals. It was thus possible to characterize the magnetic susceptibility tensor of the entire series, giving an insight of how the crystal field interactions can affect the magnetic anisotropy of a system and confirming that a rational combination of the geometry of the ligand with the electron charge distribution of the $4f^n$ ions can be exploited to control the magnetic anisotropy.

Crystal field interactions in rare-earth based SMMs are often treated as

perturbations and theoretical models and calculations often failed in a correct description of these systems due to an over-parametrization requested or to over-simplifications of the problem. In this sense the results obtained demonstrate the importance of angular resolved magnetometry in providing the necessary data to test the validity of the different theoretical approaches.

In characterizing the Cp*ErCOT single crystals it was shown that, also if in the presence of a compound crystallizing in a non-triclinic system with more than one molecular orientation in the crystalline lattice, an appropriate experimental planning can lead to relevant results. Indeed the right choice of the rotational axis, on the basis of the system symmetries, the use of two different angular resolved magnetometer techniques together with the study of the dynamics of the magnetization allowed to discern the presence of a magnetic easy-axis anisotropy in the molecules out from an almost isotropic behavior. On the other hand for a univocal assignment of the molecular anisotropy theoretical calculations were needed.

Both experiments conducted on magnetic molecules' single crystals are good representatives of the complexity lying in the characterization of such molecules and underline the necessity of flanking experimental results with theoretical ones in order to obtain a correct description of the magnetic properties of the system.

Having in mind the final but ambitious goal of exploiting the magnetic bistability of SMMs at the single molecule level, magnetometry does not present the necessary senistivity. We have therefore explored an alternative route based on the characterization of the electric transport through a thin layer of molecules embedded in a multilayer architecture.

Although preliminary, the results obtained with experiments on spintronics devices comprising magnetic molecules revealed to be promising.

Concerning the gold nanoparticles' systems functionalized with Fe_4 SMMs a measurable electric response, ascribable to thermally activated processes, was recorded at room temperature related to the presence of the SMMs and depending on the number of functionalization steps. The characterization of this system still lacks measurements in the presence of magnetic fields which could reveal possible effects in electric transport

coming from the magnetic properties of Fe_4. The conductivity at low temperatures appears however too low to perform this type of experiment and other architectures are under investigation.

Effects induced by an external magnetic field were instead observed for the first time, to the best of our knowledge, in the organic based spin-valve devices where a molecule magnetic layer is present. The two typologies of devices studied, one containing a Fe_4 molecular layer and the second a monolayer of magnetic molecules NNR, showed both spin-valve effect. Interestingly, the molecular spins do not seem to act as scattering centers suppressing the spin polarization of the current flowing through the organic semiconductor. This opens the perspective of using magnetic molecules as an active layer in spin valve devices. The effects of interfaces between the different layers of these heterostructured devices seem to play a relevant role but a convincing description of how the electric transport works in these systems is still not present and we hope that by tuning the properties of the magnetic molecules at the interface we can gain a deeper understanding of how organic spintronics devices work.

Bibliography

[1] *Global Magnetic Materials Market Analysis*, `http://www.electronics.ca/global-magnetic-materials-market-analysis.html`, 2014.

[2] R. Sessoli, H. L. Tsai, A. R. Schake, S. Wang, J. B. Vincent, K. Folting, D. Gatteschi, G. Christou and D. N. Hendrickson, *Journal of the American Chemical Society*, 1993, **115**, 1804–1816.

[3] R. Sessoli, D. Gatteschi, A. Caneschi and M. A. Novak, *Nature*, 1993, **365**, 141–143.

[4] N. Ishikawa, M. Sugita, T. Ishikawa, S.-y. Koshihara and Y. Kaizu, *Journal of the American Chemical Society*, 2003, **125**, 8694–8695.

[5] A. R. Rocha, V. M. Garcia-suarez, S. W. Bailey, C. J. Lambert, J. Ferrer and S. Sanvito, *Nature Materials*, 2005, **4**, 335–339.

[6] L. Bogani and W. Wernsdorfer, *Nature Materials*, 2008, **7**, 179–186.

[7] M. Affronte, *Journal of Materials Chemistry*, 2009, **19**, 1731–1737.

[8] M. N. Leuenberger and D. Loss, *Nature*, 2001, **410**, 789–793.

[9] A. Ardavan, O. Rival, J. J. L. Morton, S. J. Blundell, A. M. Tyryshkin, G. A. Timco and R. E. P. Winpenny, *Physical Review Letters*, 2007, **98**, 057201.

[10] P. C. E. Stamp and A. Gaita-Arino, *Journal of Materials Chemistry*, 2009, **19**, 1718–1730.

[11] A. Candini, S. Klyatskaya, M. Ruben, W. Wernsdorfer and M. Affronte, *Nano Letters*, 2011, **11**, 2634–2639.

[12] M. Mannini, F. Pineider, P. Sainctavit, C. Danieli, E. Otero, C. Sciancalepore, A. M. Talarico, M.-A. Arrio, A. Cornia, D. Gatteschi and R. Sessoli, *Nature Materials*, 2009, **8**, 194–197.

[13] C. Eckart, *Reviews of Mododern Physics*, 1930, **2**, 305–380.

[14] N. W. Ashcroft and N. D. Mermin, *Solid State Physics*, Saunders College, Orlando, 1976.

[15] K. W. H. Stevens, *Proceedings of the Physical Society. Section A*, 1952, **65**, 209–215.

[16] A. Abragam and B. Bleaney, *Electron paramagnetic resonance of transition ions*, Clarendon Press, Oxford, 1970.

[17] D. Gatteschi, R. Sessoli and J. Villain, *Molecular Nanomagnets*, Oxford University Press, New York, 2006.

[18] M. T. Hutchings, in *Solid State Physics*, ed. F. Seitz and D. Turnbull, Academic Press, 1964, vol. 16, pp. 227–273.

[19] H. A. Kramers, *Proceedings Koninklijke Akademie van Wetenschappen*, 1930, **33**, 959–972.

[20] J. D. Rinehart and J. R. Long, *Chemical Science*, 2011, **2**, 2078–2085.

[21] J. Clarke and A. I. Braginski, *The SQUID handbook: fundamentals and technology of SQUIDs and SQUID Systems, Volume I*, Wiley-VCH Verlag GmbH & Co. KGaA, Weinheim, 2004, p. 396.

[22] B. D. Josephson, *Physics Letters*, 1962, **1**, 251–253.

[23] C. P. Poole, Jr., H. A. Farach, R. J. Creswick and R. Prozorov, *Superconductivity*, Academic Press, 2nd edn., 2007, p. 670.

[24] A. H. Silver and J. E. Zimmerman, *Physical Review*, 1967, **157**, 317–341.

[25] K. S. Cole and R. H. Cole, *Journal of Chemical Physics*, 1941, **9**, 341–351.

[26] H. B. G. Casimir and F. K. Du Pré, *Physica*, 1938, **5**, 507–511.

[27] I. J. Hewitt, J. Tang, N. T. Madhu, C. E. Anson, Y. Lan, J. Luzon, M. Etienne, R. Sessoli and A. K. Powell, *Angewandte Chemie International Edition*, 2010, **49**, 6352–6356.

[28] J. Luzon and R. Sessoli, *Dalton Transactions*, 2012, **41**, 13556–13567.

[29] G. Cowan, *Statistical Data Analysis*, Oxford University Press, Oxford, 1998.

[30] W. H. Press, S. A. Teukolsky, W. T. Vetterling and B. P. Flannery, *Numerical Recipes in C*, Cambridge University Press, Cambridge, 2nd edn., 1992.

[31] L. Hunt, *Journal of Scientific Instruments*, 1944, **21**, 97.

[32] N. Viola-Villegas and R. P. Doyle, *Coordination Chemistry Reviews*, 2009, **253**, 1906–1925.

[33] M. Bottrill, L. Kwok and N. J. Long, *Chemical Society Reviews*, 2006, **35**, 557–571.

[34] L. Armelao, S. Quici, F. Barigelletti, G. Accorsi, G. Bottaro, M. Cavazzini and E. Tondello, *Coordination Chemistry Reviews*, 2010, **254**, 487–505.

[35] P.-E. Car, M. Perfetti, M. Mannini, A. Favre, A. Caneschi and R. Sessoli, *Chemical Communications*, 2011, **47**, 3751–3753.

[36] G. Cucinotta, M. Perfetti, J. Luzon, M. Etienne, P.-E. Car, A. Caneschi, G. Calvez, K. Bernot and R. Sessoli, *Angewandte Chemie International Edition*, 2012, **51**, 1606–1610.

[37] J. F. Desreux, *Inorganic Chemistry*, 1980, **19**, 1319–1324.

[38] F. Benetollo, G. Bombieri, S. Aime and M. Botta, *Acta Crystallographica Section C*, 1999, **55**, 353–356.

[39] O. Kahn, *Molecular magnetism*, Wiley-VCH, 1993.

[40] G. Karlström, R. Lindh, P.-A. Malmqvist, B. O. Roos, U. Ryde, V. Veryazov, P.-O. Widmark, M. Cossi, B. Schimmelpfennig, P. Neogrady and L. Seijo, *Computational Materials Science*, 2003, **28**, 222–239.

[41] L. Chibotaru, L. Ungur and A. Soncini, *Angewandte Chemie International Edition*, 2008, **47**, 4126–4129.

[42] P.-H. Guo, J.-L. Liu, Z.-M. Zhang, L. Ungur, L. F. Chibotaru, J.-D. Leng, F.-S. Guo and M.-L. Tong, *Inorganic Chemistry*, 2012, **51**, 1233–1235.

[43] G. Novitchi, G. Pilet, L. Ungur, V. V. Moshchalkov, W. Wernsdorfer, L. F. Chibotaru, D. Luneau and A. K. Powell, *Chemical Science*, 2012, **3**, 1169–1176.

[44] F. Tuna, C. A. Smith, M. Bodensteiner, L. Ungur, L. F. Chibotaru, E. J. L. McInnes, R. E. P. Winpenny, D. Collison and R. A. Layfield, *Angewandte Chemie International Edition*, 2012, **51**, 6976–6980.

[45] Y.-N. Guo, G.-F. Xu, W. Wernsdorfer, L. Ungur, Y. Guo, J. Tang, H.-J. Zhang, L. F. Chibotaru and A. K. Powell, *Journal of the American Chemical Society*, 2011, **133**, 11948–11951.

[46] H. L. C. Feltham, Y. Lan, F. Klöwer, L. Ungur, L. F. Chibotaru, A. K. Powell and S. Brooker, *Chemistry – A European Journal*, 2011, **17**, 4362–4365.

[47] K. Bernot, J. Luzon, A. Caneschi, D. Gatteschi, R. Sessoli, L. Bogani, A. Vindigni, A. Rettori and M. G. Pini, *Physical Review B*, 2009, **79**, 134419.

[48] K. Bernot, J. Luzon, L. Bogani, M. Etienne, C. Sangregorio, M. Shanmugam, A. Caneschi, R. Sessoli and D. Gatteschi, *Journal of the American Chemical Society*, 2009, **131**, 5573–5579.

[49] P. A. Malmqvist, B. O. Roos and B. Schimmelpfennig, *Chemical Physics Letters*, 2002, **357**, 230–240.

[50] L. Ungur and L. F. Chibotaru, *Physical Chemistry Chemical Physics*, 2011, **13**, 20086–20090.

[51] J.-C. G. Bunzli and C. Piguet, *Chemical Society Reviews*, 2005, **34**, 1048–1077.

[52] W. Wernsdorfer, N. E. Chakov and G. Christou, *Physical Review Letters*, 2005, **95**, 037203.

[53] M. Sugita, N. Ishikawa, T. Ishikawa, S.-y. Koshihara and Y. Kaizu, *Inorganic Chemistry*, 2006, **45**, 1299–1304.

[54] S.-D. Jiang, B.-W. Wang, H.-L. Sun, Z.-M. Wang and S. Gao, *Journal of the American Chemical Society*, 2011, **133**, 4730–4733.

[55] S.-D. Jiang, S.-S. Liu, L.-N. Zhou, B.-W. Wang, Z.-M. Wang and S. Gao, *Inorganic Chemistry*, 2012, **51**, 3079–3087.

[56] W. Wernsdorfer, T. Ohm, C. Sangregorio, R. Sessoli, D. Mailly and C. Paulsen, *Physical Review Letters*, 1999, **82**, 3903–3906.

[57] T. Ohm, C. Sangregorio and C. Paulsen, *European Physical Journal B*, 1998, **6**, 195–199.

[58] A. Cuccoli, A. Fort, A. Rettori, E. Adam and J. Villain, *European Physical Journal B*, 1999, **12**, 39–46.

[59] M. Johnson and R. Silsbee, *Physical Review Letters*, 1985, **55**, 1790–1793.

[60] M. Baibich, J. Broto, A. Fert, F. Van Dau, F. Petroff, P. Etienne, G. Creuzet, A. Friederich and J. Chazelas, *Physical Review Letters*, 1988, **61**, 2472–2475.

[61] G. Binasch, P. Grünberg, F. Saurenbach and W. Zinn, *Physical Review B*, 1989, **39**, 4828–4830.

[62] S. V. Aradhya and L. Venkataraman, *Nature Nanotechnology*, 2013, **8**, 399–410.

[63] S. Thiele, R. Vincent, M. Holzmann, S. Klyatskaya, M. Ruben, F. Balestro and W. Wernsdorfer, *Physical Review Letters*, 2013, **111**, 037203.

[64] M. Urdampilleta, S. Klyatskaya, J.-P. Cleuziou, M. Ruben and W. Wernsdorfer, *Nature Materials*, 2011, **10**, 502–506.

[65] A. S. Zyazin, J. W. G. van den Berg, E. A. Osorio, H. S. J. van der Zant, N. P. Konstantinidis, M. Leijnse, M. R. Wegewijs, F. May, W. Hofstetter, C. Danieli and A. Cornia, *Nano Letters*, 2010, **10**, 3307–3311.

[66] R. Vincent, S. Klyatskaya, M. Ruben, W. Wernsdorfer and F. Balestro, *Nature*, 2012, **488**, 357–360.

[67] L. Bogani, C. Danieli, E. Biavardi, N. Bendiab, A.-L. Barra, E. Dalcanale, W. Wernsdorfer and A. Cornia, *Angewandte Chemie International Edition*, 2009, **48**, 746–750.

[68] E. Burzurí, A. Zyazin, A. Cornia and H. van der Zant, *Physical Review Letters*, 2012, **109**, 147203.

[69] H. B. Heersche, Z. De Groot, J. A. Folk, H. S. J. Van Der Zant, C. Romeike, M. R. Wegewijs, L. Zobbi, D. Barreca, E. Tondello and A. Cornia, *Physical Review Letters*, 2006, **96**, 206801.

[70] T. Komeda, H. Isshiki, J. Liu, Y.-F. Zhang, N. Lorente, K. Katoh, B. K. Breedlove and M. Yamashita, *Nature Communications*, 2011, **2**, 217.

[71] G. D. Alley, *IEEE Transactions on Microwave Theory and Techniques*, 1970, **18**, 1028–1033.

[72] R. K. Hoffmann, *Handbook of microwave integrated circuits*, Artech House, Inc., Norwood, MA, 1987.

[73] J. Wei, *IEEE Journal of Quantum Electronics*, 1977, **13**, 152–158.

[74] H.-D. Wu, Z. Zhang, F. Barnes, C. M. Jackson, A. Kain and J. Cuchiaro, *IEEE Transactions on Applied Superconductivity*, 1994, **4**, 156–160.

[75] M. C. Zaretsky, J. R. Melcher and C. M. Cooke, *IEEE Transactions on Electrical Insulation*, 1989, **24**, 1167–1176.

[76] W. Qu and W. Wlodarski, *Sensors and Actuators B: Chemical*, 2000, **64**, 42–48.

[77] C. Hagleitner, A. Hierlemann, D. Lange, A. Kummer, N. Kerness, O. Brand and H. Baltes, *Nature*, 2001, **414**, 293–296.

[78] R. Zhou, A. Hierlemann, U. Weimar and W. Göpel, *Sensors and Actuators B: Chemical*, 1996, **34**, 356–360.

[79] C. A. Goss, D. H. Charych and M. Majda, *Analytical Chemistry*, 1991, **63**, 85–88.

[80] S. Accorsi, A.-L. Barra, A. Caneschi, G. Chastanet, A. Cornia, A. C. Fabretti, D. Gatteschi, C. Mortalò, E. Olivieri, F. Parenti, P. Rosa, R. Sessoli, L. Sorace, W. Wernsdorfer and L. Zobbi, *Journal of the American Chemical Society*, 2006, **128**, 4742–4755.

[81] M. Perfetti, F. Pineider, L. Poggini, E. Otero, M. Mannini, L. Sorace, C. Sangregorio, A. Cornia and R. Sessoli, *Small*, 2014, **10**, 323–329.

[82] T. Ogawa, K. Kobayashi, G. Masuda, T. Takase and S. Maeda, *Thin Solid Films*, 2001, **393**, 374–378.

[83] V. A. Dediu, L. E. Hueso, I. Bergenti and C. Taliani, *Nature materials*, 2009, **8**, 707–716.

[84] G. Szulczewski, S. Sanvito and M. Coey, *Nature materials*, 2009, **8**, 693–695.

[85] V. Dediu, M. Murgia, F. Matacotta, C. Taliani and S. Barbanera, *Solid State Communications*, 2002, **122**, 181–184.

[86] A. Dodabalapur, L. Torsi and H. E. Katz, *Science*, 1995, **268**, 270–271.

[87] J. H. Schön, C. Kloc, A. Dodabalapur and B. Batlogg, *Science*, 2000, **289**, 599–601.

[88] V. Dediu, L. Hueso, I. Bergenti, A. Riminucci, F. Borgatti, P. Graziosi, C. Newby, F. Casoli, M. De Jong, C. Taliani and Y. Zhan, *Physical Review B*, 2008, **78**, 115203.

[89] P. Graziosi, M. Prezioso, A. Gambardella, C. Kitts, R. K. Rakshit, A. Riminucci, I. Bergenti, F. Borgatti, C. Pernechele, M. Solzi, D. Pullini, D. Busquets-Mataix and V. A. Dediu, *Thin Solid Films*, 2013, **534**, 83–89.

[90] J.-H. Park, E. Vescovo, H.-J. Kim, C. Kwon, R. Ramesh and T. Venkatesan, *Nature*, 1998, **392**, 794–796.

[91] P. de Gennes, *Physical Review*, 1960, **118**, 141–154.

[92] L. Poggini, *Ph.D. thesis*, Università degli Studi di Firenze, 2014.

[93] I. Bergenti, V. Dediu, M. Prezioso and A. Riminucci, *Philosophical Transactions of the Royal Society of London A: Mathematical, Physical and Engineering Sciences*, 2011, **369**, 3054–3068.

[94] S. Steil, N. Groszmann, M. Laux, A. Ruffing, D. Steil, M. Wiesenmayer, S. Mathias, O. L. A. Monti, M. Cinchetti and M. Aeschlimann, *Nature Physics*, 2013, **9**, 242–247.

[95] Y. Zhan, E. Holmström, R. Lizárraga, O. Eriksson, X. Liu, F. Li, E. Carlegrim, S. Stafström and M. Fahlman, *Advanced Materials*, 2010, **22**, 1626–1630.

[96] Z. H. Xiong, D. Wu, V. Z. Valy and J. Shi, *Nature*, 2004, **427**, 821–824.

[97] M. Prezioso, A. Riminucci, I. Bergenti, P. Graziosi, D. Brunel and V. A. Dediu, *Advanced Materials*, 2011, **23**, 1371–1375.

[98] T. T. Fister, D. D. Fong, J. A. Eastman, P. M. Baldo, M. J. Highland, P. H. Fuoss, K. R. Balasubramaniam, J. C. Meador and P. A. Salvador, *Applied Physics Letters*, 2008, **93**, 151904.

[99] K. Katsiev, B. Yildiz, K. Balasubramaniam and P. A. Salvador, *Applied Physics Letters*, 2009, **95**, 092106.

[100] H. Jalili, J. W. Han, Y. Kuru, Z. Cai and B. Yildiz, *The Journal of Physical Chemistry Letters*, 2011, **2**, 801–807.

[101] Å. Monsen, F. Song, Z. Li, J. Boschker, T. Tybell, E. Wahlström and J. Wells, *Surface Science*, 2012, **606**, 1360–1366.

[102] A. Caneschi, F. Ferraro, D. Gatteschi, A. le Lirzin and E. Rentschler, *Inorganica Chimica Acta*, 1995, **235**, 159–164.

[103] M. Mannini, L. Sorace, L. Gorini, F. M. Piras, A. Caneschi, A. Magnani, S. Menichetti and D. Gatteschi, *Langmuir*, 2007, **23**, 2389–2397.

[104] G. Rajaraman, A. Caneschi, D. Gatteschi and F. Totti, *Journal of Materials Chemistry*, 2010, **20**, 10747–10754.

[105] M. Mannini, F. Pineider, C. Danieli, F. Totti, L. Sorace, P. Sainctavit, M.-A. Arrio, E. Otero, L. Joly, J. C. Cezar, A. Cornia and R. Sessoli, *Nature*, 2010, **468**, 417–421.

[106] L. Margheriti, M. Mannini, L. Sorace, L. Gorini, D. Gatteschi, A. Caneschi, D. Chiappe, R. Moroni, F. B. de Mongeot, A. Cornia, F. M. Piras, A. Magnani and R. Sessoli, *Small*, 2009, **5**, 1460–1466.

[107] L. Rigamonti, M. Piccioli, L. Malavolti, L. Poggini, M. Mannini, F. Totti, B. Cortigiani, A. Magnani, R. Sessoli and A. Cornia, *Inorganic Chemistry*, 2013, **52**, 5897–5905.

[108] L. Malavolti, V. Lanzilotto, S. Ninova, L. Poggini, I. Cimatti, B. Cortigiani, L. Margheriti, D. Chiappe, E. Otero, P. Sainctavit, F. Totti, A. Cornia, M. Mannini and R. Sessoli, *Nano Letters*, 2014, available on-line, doi:10.1021/nl503925h.

[109] P. E. Burrows, L. S. Sapochak, D. M. McCarty, S. R. Forrest and M. E. Thompson, *Applied Physics Letters*, 1994, **64**, 2718–2720.

[110] P. Shakya, P. Desai, M. Somerton, G. Gannaway, T. Kreouzis and W. Gillin, *Journal of Applied Physics*, 2008, **103**, 103715–103715.

[111] J.-H. Park, E. Vescovo, H.-J. Kim, C. Kwon, R. Ramesh and T. Venkatesan, *Physical review letters*, 1998, **81**, 1953.

[112] A. Riminucci, I. Bergenti, L. E. Hueso, M. Murgia, C. Taliani, Y. Zhan, F. Casoli, M. P. de Jong and V. Dediu, *eprint arXiv:cond-mat/0701603*, 2007.

[113] F. J. Wang, C. G. Yang, Z. V. Vardeny and X. G. Li, *Physical Review B*, 2007, **75**, 245324.

[114] W. Xu, G. J. Szulczewski, P. LeClair, I. Navarrete, R. Schad, G. Miao, H. Guo and A. Gupta, *Applied Physics Letters*, 2007, **90**, 072506–072506.

Acknowledgments

First of all I would like to express my gratitude to my supervisor Prof. Roberta Sessoli for all the time she dedicated to me, her support and the trust she always put in me. From her I learned, not only all that I know on molecular magnetism, but also how to do research.

Thanks to all the people of LA.M.M. for the opportunity they gave me to do research in a stimulating and familiar environment and for the patience every time that my "few hours measurement" took several days of time-machine.

I'm particularly grateful to Matteo Mannini for his helpfulness, his support and his friendship.

A special thank to Marie-Emmanuelle Boulon. We shared joys and sorrows of working with single crystals. Thanks for all the things she taught me and for her friendship.

Thanks are also due to Dr. Valentin Alek Dediu and his group in Bologna for the precious collaboration in OSVs work.

I am also grateful to Prof. Giuseppe Maruccio and his collaborators for the time I spent in their laboratories in Lecce and for the priceless help with experiments on interdigitated electrodes.

I want to thank all the new and old friends I met in these years. The roommates of room 338: Eva Lucaccini, Mauro Perfetti, Elisabetta Lottini, Martin Albino, Michele Petrecca, Andrea Guerrini, Pasquale Totaro and Silviya Ninova; the canteen team: Massimo Manuelli, Irene Cimatti,

Michele Serri; Luigi Malavolti and Lorenzo Poggini. Thank you all for your friendship and for having stood with me all this time.